Modelling self healing creep steel

Versteylen, Casper

Important note
To cite this publication, please use the final published version (if applicable).
Please check the document version above.

MODELLING SELF HEALING CREEP STEEL

MODELLING SELF HEALING CREEP STEEL

Proefschrift

ter verkrijging van de graad van doctor
aan de Technische Universiteit Delft,
op gezag van de Rector Magnificus prof. dr. ir. T.H.J.J. van der Hagen,
voorzitter van het College voor Promoties,
in het openbaar te verdedigen op vrijdag 22 juni om 10:00 uur

door

Casper Daniël VERSTEYLEN

Ingenieur Luchtvaart en Ruimtevaart,
Technische Universiteit Delft,
geboren te Tilburg, Nederland.

Dit proefschrift is goedgekeurd door de promotoren.

Samenstelling promotiecommissie:

Rector Magnificus,   voorzitter

promotor: prof. dr. E.H. Brück
promotor: dr. ir. N.H. van Dijk
promotor: dr. ir. M.H.F. Sluiter

Onafhankelijke leden:
Prof. dr. J. Neugebauer

          Max-Planck-Institut für Eisenforschung GmbH

Prof. dr. ir. B.J. Kooi

          University of Groningen

Prof. dr. G.C.A.M. Janssen

          Technische Universiteit Delft

Prof. dr. ir. S. van der Zwaag

          Technische Universiteit Delft

CONTENTS

SUMMARY

Advances in self-healing creep steels are driven by the understanding of its mechanism. Previous work on self-healing creep metals has shown selective precipitation inside the creep cavities, which has a beneficial effect on the creep lifetime. This effect occurs when a solute supersaturation exists at the creep temperature. In the case of self-healing creep steels, the precipitation of gold was found to have an exceptional effect. Gold precipitation was found to be efficient because of the atomic size mismatch of gold and iron, which induces a high selectivity for precipitates to form inside creep cavities and not in the bulk. However, gold is not the most widely used alloying element in steel, to put it mildly. Ideally the self-healing effect could be achieved by another solute element dissolved in steel. In order to identify some other possible solute element for self healing creep steels, the mechanism must be understood. In this thesis the mechanism of self healing creep steels, and metals in general, is investigated.

This thesis is divided in chapters in which parts of the processes which govern self-healing and creep damage formation are reviewed. The ultimate goal is to unravel the mechanism and propose optimised compositions for self-healing creep steels for high temperature healing. This was done to provide insight in the factors which determine the efficiency of a self healing creep-resistant alloy and also to establish a theory of the process of self healing in metals and on creep damage formation in general. The diffusivity of elements in bcc iron determines the kinetics of many processes. The rate of growth of a creep void, the growth rate of precipitates and also the creep deformation rate are all defined by diffusivities. Bcc-iron diffusion is a special case when compared to other hosts for diffusion. The reason for this is the role of magnetic disordering which influences the activation energy for diffusion. As a result, the activation energy for diffusion is not constant with temperature. This temperature dependent activation energy is required to determine all diffusivities. The diffusivities of iron self-diffusion and impurity elements through the bulk and through the grain boundary determine how fast grain-boundary voids and precipitates can grow. The healing of creep voids by precipitation affects the strain rate during creep deformation. The link between creep deformation, creep void growth and healing can be modelled, which then also leads to the critical stress for self-healing of alloys with regard to temperature.

In **chapter 2** the impurity diffusion rates are calculated using *first-principles*. Diffusivities in bcc iron are modelled by determining formation energies of defects, vacancy-impurity binding and nearest migration barriers are calculated in order to obtain an activation energy for diffusion. The formation energies of defects are calculated using VASP to compute total energies and jump barrier energies. Entropies of formation were obtained from harmonic phonon calculations. The prefactor is determined by calculating vibration entropies and the jump frequency of the impurity element. The resulting activation energy and prefactor for diffusion provide species dependent diffusivities. These diffusivities are compared to experiment in order to validate the method. The trends of

substitutional impurity diffusion in bcc iron are as follows: fast diffusion for those elements at the fringes of the periodic table and comparable diffusivity with respect to iron self-diffusion for those elements which are found in the centre of the periodic table of the elements. The diffusivity of substitutional elements which require a single vacancy to diffuse play are important for self-healing. For an analysis of the healing of creep damage, this chapter is fundamental.

A specific issue which complicates the diffusivity calculations in bcc iron is the magnetic order-to-disorder transformation. In **chapter 3** the effect of magnetic ordering on diffusivity in bcc iron is reviewed for a large selection of datasets. The activation barrier for diffusion changes with the degree of magnetic order. This magnetic order also has its effect on the phonon softening in a particular shear direction.The reduction of the activation barrier for diffusion can be related to either the persistence of long-range magnetic order, or the total magnetic energy associated to spin allignment. This effect can be represented by the Girifalco model and the Jönsson model, respectively. The merits and limitations of each model are reviewed and the implications of applying each model shows that the Girifalco model is preferred. The application of the Girifalco model to fit experimentally determined diffusion data provides the most reasonable result. Fitting the datasets of impurity elements to the Girifalco model provides a constant α which relates the effect of the spontaneous magnetisation to the diffusivity. Filtering the most reliable datasets by magnitude of the error, a constant value of $\alpha = 0.10(1)$ is obtained.

In **chapter 4** finite element calculations are presented of solute diffusion towards creep cavities. The time required to fill a creep cavity on a grain boundary by a diffusional flux of supersaturated solute depends on the diffusivity of grain boundary and bulk and on the geometric ratio of creep cavity radius and the intercavity distance. For a relatively large intercavity spacing, 3D transport is observed when the grain boundary and volume diffusivities are of a similar order of magnitude, while a 2D behavior is observed when the grain boundary diffusivity is dominant. Instead when the intercavity distance is small, the transport behavior tends to a 1D behavior in all cases, as the amount of solute available in the grain boundary is insufficient. This is a relevant observation for creep cavity growth and precipitate growth, since their distance can vary during annealing of a metal at high temperature. This can lead to a change in character of the diffusional behaviour. A phase diagram with the transition lines is presented.

A design principle for new creep steels is presented in **chapter 5**. The results of the concept can be used to elucidate the mechanism of self-healing creep metals. The flux of vacancies towards a creep void can be countered by selective precipitation, which thereby prevents creep cavity growth. This vacancy flux is shown to be related to the bulk deformation, leading to the possibility of a significantly extended service life.

In **chapter 6** the previously developed conceptual model is formalised using readily available equations. The self-healing process causes precipitates to grow inside creep cavities. Due to the Kirkendall effect, vacancies are transported away from the creep cavity during this selective precipitation, which impedes their growth. The magnitude of this effect depends on the strength of the solute flux towards a creep cavity, and therefore on the chemical potential for segregation and the solute mobility. The atomic mobilities for bcc iron have been determined in chapter 2 and the chemical potential is derived from the amount of supersaturation. With this model it is possible to calculate

the critical stress at which self-healing can work, which depends on the solute species, solute content and temperature dependent value. The model is applied to binary Fe-Cu, Fe-Au, Fe-Mo, and Fe-W alloys. Fe-Au is found to be the most efficient self-healing alloy.

SAMENVATTING

De ontwikkeling van zelfherstellend kruipstaal wordt gedreven door het begrip van de onderliggende mechanisme. Onderzoek naar zelfherstellende kruipmetalen heeft laten zien dat selectieve precipitatie binnen de kruipholtes een vertragend effect heeft op de kruipsnelheid van metaallegeringen. Dit effect treed op als er een oversaturatie van opgeloste atomen bestaat op de kruiptemperatuur. In het geval van zelfherstellend staal bleek goudprecipitatie een uitzonderlijk groot effect te hebben. Goudprecipitatie werd gezien als efficiënt vanwege de verschillende atomaire afmetingen van goud en ijzer, wat een selectieve precipitatie in de holtes afdwingt. Goud is echter op zijn zachts gezegd niet het meest gebruikte legeringselement. Idealiter kan dit zelfherstellende effect ook optreden vanwege het oplossen van een ander element in staal. Het volledige proces moet worden begrepen om te bepalen welke elementen zodanig kunnen werken. In dit proefschrift wordt het mechanisme van zelfherstellende kruipstalen, en metalen in het algemeen, onderzocht. Dit proefschrift is opgedeeld in hoofdstukken waarin delen van de processen die het zelfherstellend gedrag en kruipschade vorming beheersen. Het ultieme doel hiervan is om de werking van het zelfherstellend mechanisme in kaart te brengen en composities voorstellen van zelfherstellend staal wat kan werken op hoge temperatuur. Dit is gedaan om inzicht te verschaffen in de factoren die de efficiëntie van zelfherstellend kruip-resistente legeringen en om een algemene theorie voort te brengen over het zelfherstellend effect en de schadevorming onder kruip belasting. De diffusiviteit van elementen in bcc (body centered cubic) ijzer bepaald de kinetiek van de processen. De groei van kruipholtes, de groei van precipitaten en ook de kruip vervorming worden allen bepaald door de diffusiviteit. Bcc ijzer is een bijzonder geval als men het vergelijkt met andere basismaterialen. Het magnetisch effect op de energiebarrière voor diffusie is de reden dat de activeringsenergie niet constant is met temperatuur. De temperatuur afhankelijkheid van de activeringsenergie is nodig om de diffusiviteit te bepalen. De diffusie binnen de korrels en op de korrelgrenzen bepaald hoe snel korrelgrens holtes en precipitaten kunnen groeien. Het autonome herstel van korrelgrens kruipholtes door middel van precipitatie heeft een direct effect op de vervormingssnelheid. Het verband tussen kruip vervormingssnelheid en de kruipholte groei kan gemodelleerd worden, wat ook een kritische spanning voor zelfherstellende metalen als functie van de temperatuur oplevert.

In **hoofdstuk 2** zijn de diffusiviteiten van elementen in ijzer berekend met behulp van *first-principles*. Diffusiviteiten in bcc ijzer zijn berekend via het berekenen van formatie energieën van puntdefecten, vacature-atoom binding en naaste buurmigratie barrières, die de activeringsenergie voor diffusie opleveren. De formatie energieën van defecten zijn bepaald met VASP waarmee totale energie en barrière energieën berekend kunnen worden. De voorfactor is berekend door formatie entropieën te berekenen met harmonische fononen berekeningen en de sprongfrequentie van legeringselementen. De activeringsenergiën en de prefactoren voor legeringselementen in ijzer leveren temperatuurs-

afhankelijke diffusiviteiten op. Waar mogelijk, zijn deze vergeleken met experimentele waardes. De trends voor de diffusie van legeringselementen in ijzer zijn als volgt: snelle diffusie voor de elementen aan de randen van het periodieke systeem der elementen en diffusie snelheden vergelijkbaar met ijzer zelfdiffusie voor de elementen in het midden van het periodieke systeem. De diffusie van legeringselementen is van fundamenteel belang voor de werking van zelfherstellend kruipstaal.

Een bcc ijzer specifiek probleem wat de diffusiviteits berekeningen compliceert is de magnetische orde-wanorde transitie. In **hoofdstuk 3** wordt het effect van de magnetische orde op de diffusiviteit in bcc ijzer overzien en geanalyseerd met behulp van een grote selectie diffusiedatasets. De activeringsbarrière voor diffusie veranderd met de mate van magnetische order. Deze magnetische order heeft ook een effect op een specifieke stijfheidsrichting. De verlaging van de barrière voor diffusie is groot rond de Curie temperatuur en kan ofwel aan het verlies van langeafstand order, of aan de totale magnetische enthalpie worden gerelateerd. Dit effect wordt gemodelleerd door respectievelijk het Girifalco model en Jönsson model. De voordelen en nadelen van elk model is geanalyseerd alsmede de implicaties van elk model wat laat zien dat het Girifalco model geprefereerd is in dit geval. De fit van het Girifalco model met de experimentele resultaten van diffusiviteiten levert het meest redelijke resultaat. Wanneer alle datasets van legeringselementen gefit worden met het Girifalco model levert dit een stabiele waarde van constante α op. De constante α gerelateerd het effect van de ferromagnetische magnetisatie met de diffusiviteit. De meest betrouwbare datasets zijn gefilterd op een vooraf bepaalde grootte van de error, dit levert een waarde voor $\alpha = 0.10(1)$ op.

In **hoofdstuk 4** worden de resultaten van eindige-elementenmethode berekeningen van opgeloste elementen die diffunderen richting kruipholtes gepresenteerd. De tijd die benodigd is om een kruipholte op een korrelgrens te vullen met een diffusionele flux van oververzadigde elementen hangt af van de diffusiesnelheid over korrelgrens en door de korrel (of volume) en van de ratio tussen kruipholteradius en de afstand tussen kruipholtes. Voor een relatief grote afstand tussen kruipholtes word 3D transport geobserveerd als de korrelgrensdiffusie en volumediffusie van vergelijkbare orde zijn, terwijl 2D transport gedrag is geobserveerd als de korrelgrensdiffusie dominant is. Als de afstand tussen kruipholtes echter klein is, neigt het transportgedrag naar 1D in alle gevallen, omdat de hoeveelheid opgeloste elementen op de korrelgrens niet groot genoeg is. Dit is een relevante observatie voor kruipholte groei en voor precipitatie groei op korrelgrenzen, aangezien hun afstand kan variëren tijdens warmtebehandelingen van metalen. Dit lijd tot een verandering in het karakter van het diffusiegedrag. Een fase diagram van dit gedrag is gemaakt waarop ook is aangegeven waar transitiepunten liggen.

Een ontwerpprincipe voor nieuwe kruip-resistente staalsoorten is gepresenteerd in **hoofdstuk 5**. De resultaten van het concept kan worden gebruikt om het mechanisme van zelfherstellende metalen op te helderen. De flux van vacatures richting de kruipholte kan worden tegengegaan door middel van selectieve precipitatie, wat de groei van de kruipholte verhinderd. De vacature flux is gerelateerd aan bulkdeformatie van de korrels, wat ertoe leid dat de levensduur van de metalen significant wordt verlengd.

In **hoofdstuk 6** wordt het conceptuele model van hoofdstuk 5 uitgewerkt met behulp van formules die de verschillende fluxen omschrijven. Het zelfherstellende proces veroorzaakt de groei van precipitaten in de kruipholtes. Dankzij het Kirkendall effect wor-

den vacatures weggetransporteerd van de kruipholtes dankzij de selectieve precipitatie in de holtes, wat ervoor zorgt dat de groei van de holtes gehinderd wordt. De grote van dit effect hangt af van de kracht van de flux van opgeloste elementen richting de holtes, de drijvende kracht en de mobiliteit van elementen in ijzer. De mobiliteiten van legeringselementen in ijzer zijn bepaald in hoofdstuk 2 van dit proefschrift, de chemische potentiaal kan worden afgeleid van de hoeveelheid oververzadiging. Met behulp van dit model is het mogelijk om de kritische stress te bepalen waarop het zelfherstellend gedrag nog kan optreden. Dit is afhankelijk van de hoeveelheid oververzadigde elementen, welk element in oververzadiging is en de temperatuur. Dit model is toegepast op Fe-Cu, Fe-Au, Fe-Mo en Fe-W legeringen. Fe-Au is de meest efficiënte zelfherstellende legering.

1

INTRODUCTION

Je connais une planète où il y a un Monsieur cramoisi.
Il n'a jamais respiré une fleur.
Il n'a jamais regardé une étoile.
Il n'a jamais aimé personne.
Il n'a jamais rien fait d'autre que des additions.
Et toute la journée il répète comme toi :
"Je suis un homme sérieux! Je suis un homme sérieux!"
et ça le fait gonfler d'orgueil.
Mais ce n'est pas un homme,
c'est un champignon !

Antoine de Saint-Exupery - le petit prince

1.1. ENERGY EFFICIENCY

The dangers of global warming and pollution require a great research effort and most of all ample political courage. In the foreseeable future, neither solar, nor wind power can provide sufficient energy for the needs of society, and battery and other energy storage techniques are not yet in a mature state. Which means that the production of electricity will be by means of steam turbines, propelled by heat from either fossil or nuclear fuels. It is known from the thermodynamical properties of a Carnot cycle that the efficiency of an energy conversion turbine can be increased by raising the inlet temperature. The key to efficient energy conversion is the steam turbine temperature, which is limited by the material properties of the turbine.

1.2. CREEP DEFORMATION

One of the most relevant materials and microstructural properties in high-temperature applications is the resistance against creep deformation. Creep deformation, under constant stress and temperature, is a time-dependent deformation mode, which leads to

1

1
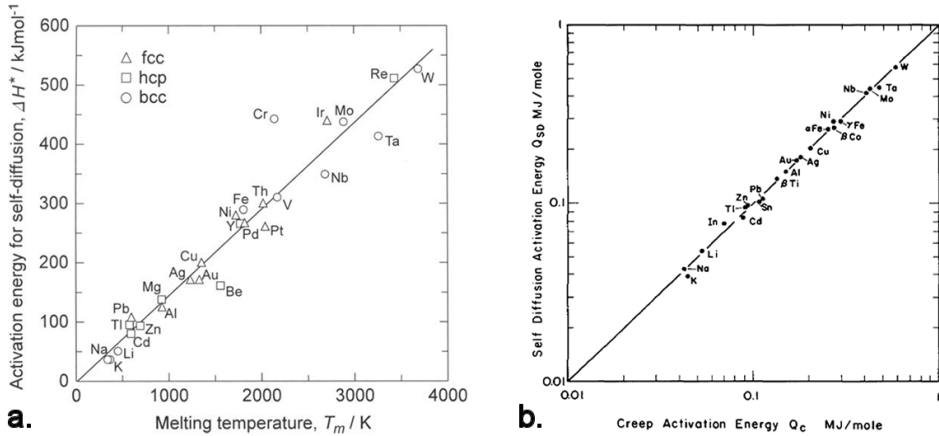
Figure 1.1: a.) Relation between the activation energy for diffusion ΔH^* and the melting temperature T_m for many pure elements with fcc, hcp and bcc cyrstal structures, from Tiwari and coworkers [1]. b.) Relation between the activation energy for self-diffusion Q_{SD} and the activation energy of creep Q_C, from Sherby & Weertman [2].

failure. Both creep deformation rates, and the activation energy for diffusion are linked to the melting temperature (T_m) of the material, see figure 1.1. For metallic materials, creep deformation starts occurring at temperatures $T > 0.4\ T_m$. The activation energy for creep is related to the self-diffusion activation energy [2]. Atom diffusivity in the bulk is the rate-controlling factor for the deformation and the growth of creep cavities. The strain rate of a metal deforming under creep is therefore in most cases determined by the bulk diffusivity. Yet despite creep being a phenomenon mostly dominated by bulk diffusion, creep cavities grow on grain boundaries by fast grain-boundary diffusion of vacancies. The description of creep cavity growth on a grain boundary under the influence of an applied stress started in the 1950s [3, 4]. The growth rate of creep cavities, which ultimately leads to the failure of creep-loaded metals, can be described by assuming that the driving force for their growth comes from an applied stress [3]. This applied stress causes a chemical potential for vacancies, which causes them to migrate to a cavity surface.. The growth of creep cavities then occurs via vacancy migration over the grain boundary by grain boundary diffusivity [4]. The vacancy formation rate is assumed to be comparatively fast.

Failure of metals subject to creep conditions occurs due to crack formation as a consequence of the growth and coalescence of creep cavities. The rate of creep deformation is controlled by bulk diffusion [2]. Yet there is a well-known experimental relation between the strain rate and the time to failure, known as the Monkman-Grant relation. The Monkman-Grant relation says that the product of the steady-state strain rate $\dot{\varepsilon}_{ss}$ and the time to failure t_f is a constant:

$$C_{MG} = \dot{\varepsilon}_{ss} t_f. \tag{1.1}$$

This provides us with an apparent inconsistency, since the strain-rate is a bulk diffusion controlled process and the growth of cavities, which leads to failure is a grain-

boundary controlled process. It was found that the growth rate of creep voids can be constrained by the rate of deformation. This lead to a description of this process by Ishida & McLean [5], where the strain rate is limiting for cavity growth by the formation of vacancies at grain boundaries due to ingressing dislocations. Dyson [6] instead states that the physical straining of the facets containing creep cavities controls their growth. The approach by Dyson has been the prevailing theory describing the constraint growth of creep cavities [7, 8].

1.3. CREEP RESISTANCE

A mechanical component needs to conform to its design criteria. At high temperatures and during long lifetimes the mechanical and dimensional features of mechanical components can deteriorate. Metal components operating at high temperatures whilst loaded by stress, deform time-dependently. During this deformation, localized damage can occur in the shape of cavities, intergranular wedge cracks, necking, or cleavage crack formations. Since damage formation largely relies on the existence of grain boundaries, the ultimate creep-resistant components are single crystal nickel-based superalloys [9]. The mode of damage formation is a function of both temperature and applied stress [10, 11]. The only common factor in these different types of damage formation is that they are temperature dependent, and they are often controlled by the diffusivity of either host or solute in either grain interiour or on the grain boundary.

In many cases the time to failure depends on the strain rate of creeping metals. Therefore, the conventional method of designing creep-resistant metals is by reinforcing both the grain interiours and the grain boundaries by nanoprecipitates [12]. The precipitates serve to avoid grain-boundary sliding and dislocation movement inside the grains. Coarse precipitates do not contribute as much to strength as small nanosized precipitates. As metals in creep conditions are also subject to precipitate coarsening the resilience to creep deformation irreversibly deteriorates as the alloy is aged at high temperatures [13]. Much of the optimisation of creep-resistant steel design is focused on maintaining stable nanosized precipitates [14].

1.4. SELF-HEALING

Recently, the concept of self-healing or autonomous repair is being applied to coatings [15, 16], polymers[17–19], composites[20], cementitious materials [21], ceramics[22, 23] and even in metallic systems [24]. Applying self-healing principles has some distinct benefits, since self-healing materials have the ability to repair damage locally, where it occurs. The self-healing methods can prolong life-times of components in similar ways as observed in biological systems.

In metals the concept of autonomous repair of creep damage by selective precipitation was first applied by Shinya and Laha [24, 25] and Lumley and coworkers [26]. Shinya and Laha allowed precipitation of boron nitride (BN) inside creep voids in austenitic stainless steels, which prolonged their creep life. It was argued that this precipitation could delay coalescence of creep voids and also block fatigue damage growth. They also showed that there is a beneficial effect of Cu in supersaturation, as it forms precipitates inside creep cavities. One could wonder however if the strength of the new precipitates

1
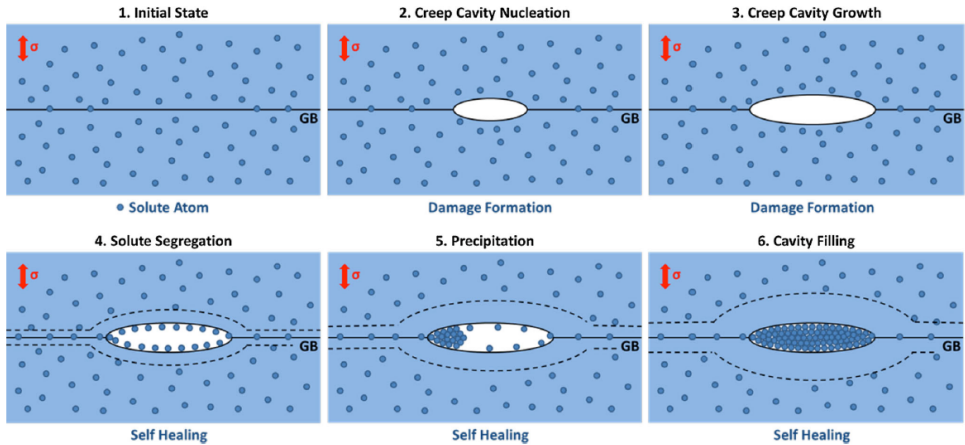
Figure 1.2: Schematic representation of self-healing creep steel, where the forming and growth of a precipitate in a creep cavity hinders the growth and coalescence of creep cavities. The precipitation growth inside a creep cavity effectively prevents the formation of cracks from creep cavities [28].

on the surface of the creep voids adds significantly to the materials' strength. And if so, how the method works both for very brittle BN, and for soft copper in steel.

Research on selective precipitation of substitutionals inside creep cavities in order to delay failure continued in Delft [27–30]. The addition of 1 atomic percent of copper to pure iron increases the lifetime and reduces the strain rate of the alloy under creep conditions. A comparison between the creep curves of an annealed specimen and a quenched specimen shows the effect of solutionising the copper. When more copper is in supersaturation, the effect of self-healing is quite pronounced and creep lifetimes can be significantly increased. More striking is the much stronger effect on the creep curve of the addition of gold [28]. Despite the fact that the precipitate which forms inside the creep cavity is bulky and should not poses any particularly high strength.

The efficiency of a self-healing creep steel in this picture relies on the degree of filling of the creep cavity and how much the precipitate prevents the growth of a partially filled creep cavity. However, it is not obvious why gold should work much better than copper, from the point of view of strength. This observation is more logical if the magnitude of the diffusional flux of the solute plays an important role.

1.5. Creep mechanism

In this thesis modelling thechniques are applied to the problem of self-healing creep steel and to the subproblems involved in both growth of creep cavities, healing, and precipitation on grain boundaries. A new model is developed on the working of self-healing creep steels and clarity is provided into how creep deformation and damage formation are linked. It is found that the efficiency of self-healing creep steels depends on the strenght of the Kirkendall effect which they cause. What is interesting about this approach is that it does not necessarily hinders traditional creep strengthening strategies.

1.6. THESIS STRUCTURE AND SCOPE

In this thesis the efficiency of self-healing elements in bcc iron are reviewed, focusing on substitutional elements in iron. In order to do this, modelling techniques are applied to specific problems associated with the creep damage and healing problems. Common industrial alloys used for creep-resistant components are multiphase iron-based alloys with a complex microstructure. The analysis of self-healing steel is limited to binary alloys in this thesis, in order to analyse separately the effect of solute atoms on diffusivity and on creep live times. This is done by calculation the diffusivities of impurity elements in bcc iron and reviewing the precipitation process inside creep cavities. The mechanism of self-healing is intricately linked to the working of diffusional creep in metals, through the Kirkendall effect and the formation rate of vacancies at grain boundaries. Reviewing this mechanism provides insight which elucidates the mechanisms controlling diffusional creep deformation and its relation to creep cavity growth. Finally, a review of the efficiency of different amounts and types of solutes is given to illustrate the critical parameters required to obtain an optimal self-healing creep alloy.

In **chapter 2** the impurity diffusion rates are calculated using *first-principles* [31]. Diffusivities in bcc iron are modelled by determining formation energies of defects and their interaction. The formation energies of defects are calculated using VASP to compute total energy calculations and jump barrier energies. Entropies of formation were obtained from harmonic phonon calculations. The trends of these factors are reviewed as function of the elements' position on the periodic table of the elements. The resulting activation energies and prefactors for diffusion provide species-dependent diffusivities. These diffusivities are compared to experiment in order to validate the method where possible.

A specific issue which complicates the diffusivity calculations in bcc iron is the magnetic order-to-disorder transition. In **chapter 3** the effect of magnetic order on diffusivity in bcc iron is reviewed for a large selection of elements and experimental datasets. The degree of magnetic order has an effect on the activation energy for diffusion. This effect and its magnitude can be described by different models. The results are presented and explained using literature knowledge and a systematic approach to fitting the experimental data to the model which best describes the deviation from Arrhenius behaviour. The large selection of experimental datasets allows for a thourough analysis of the magnitude of the magnetic effect the activation energy and also of the accuracy of each model.

In **chapter 4** finite element calculations of solute diffusion towards creep cavities are presented [32]. The time required to fill a creep cavity on a grain boundary by a diffusional flux of supersaturated solute depends on the diffusivity on grain boundaries and through the bulk and on the geometric ratio of creep cavity radius and the intercavity distance. For a relatively large intercavity spacing 3D transport is observed when the grain boundary and volume diffusivities are of a similar order of magnitude, while a 2D behavior is observed when the grain boundary diffusivity is dominant. Instead when the intercavity distance is small, the transport behavior tends to a 1D behavior in all cases, as the amount of solute available in the grain boundary is insufficient. This is a relevant observation for creep cavity growth and precipitate growth, since their distance can vary during annealing of a metal at high temperature. This can lead to a change in character

1

of the diffusional behaviour. A phase diagram with the transition lines is presented.

A design principle for new creep steels is presented in **chapter 5**. The results of the concept can be used to elucidate the mechanism of self-healing creep metals. The flux of vacancies towards a creep void can be countered by selective precipitation, which thereby prevents creep cavity growth. This vacancy flux is shown to be related to the bulk deformation, leading to the possibility of a significantly extended service life.

In **chapter 6** the previously developed conceptual model is formalised using readily available equations. The self-healing process causes precipitates to grow inside creep cavities. Due to the Kirkendall effect, vacancies are transported away from the creep cavity during this selective precipitation which impedes their growth. The magnitude of this effect depends on the strength of the solute flux towards a creep cavity and therefore on the chemical potential for segregation and the solute mobility. The atomic mobilities for bcc iron have been determined in chapter 2, the chemical potential is derived from the amount of supersaturation. With this model it is possible to calculate the critical stress at which self-healing can work. The critical stress depends on solute species, solute content and temperature. The model is applied to binary Fe-Cu, Fe-Au, Fe-Mo, and Fe-W alloys.

The main findings presented in this thesis are reiterated in the summary.

1

REFERENCES

[1] G. P. Tiwari, R. S. Mehrotra, and Y. Iijima, *Diffusion processes in Advanced Technological Materials*, edited by D. Gupta (Springer-Verlag, Norwich, New York, 2005) pp. 69–82.

[2] O. Sherby and J. Weertman, *Diffusion-controlled dislocation creep: A defense,* Acta Metall. **27**, 387 (1979).

[3] C. Herring, *Diffusional viscosity of a polycrystalline solid,* J. Appl. Phys. **21**, 437 (1950).

[4] D. Hull and D. E. Rimmer, *The growth of grain-boundary voids under stress,* Philos. Mag. **4**, 673 (1959).

[5] Y. Ishida and D. McLean, *The Formation and Growth of Cavities in creep,* Met. Sci. **38**, 171 (1967).

[6] B. F. Dyson, *Constraints on diffusional cavity growth rates,* Met. Sci. **10**, 349 (1976).

[7] J. R. Rice, *Constraints on the Diffusive Cavitation of Isolated Grain Boundary Facets in Creeping Polycrystals,* Acta Metall. **29**, 675 (1981).

[8] H. Riedel, *Life Prediction Methods for Constrained Grain Boundary Cavitation,* Int. J. Press. Vessel. Pip. **39**, 119 (1989).

[9] T. M. Pollock and S. Tin, *Nickel-Based Superalloys for Advanced Turbine Engines: Chemistry, Microstructure and Properties,* J. Propuls. Power **22**, 361 (2006).

[10] M. F. Ashby, C. Gandhi, and D. M. Taplin, *Overview No. 3 Fracture-mechanism maps and their construction for f.c.c. metals and alloys,* Acta Metall. **27**, 699 (1979).

[11] C. Gandhi and M. F. Ashby, *Fracture mechanism maps for materials which cleave: fcc, bcc and hcp metals and ceramics,* Acta Met. **27**, 1565 (1979).

[12] F. Abe, T.-U. Kern, and R. Viswanathan, *Woodhead Publ.* (Boca Raton, 2008).

[13] J. Hald, *Microstructure and long-term creep properties of 9-12% Cr steels,* Int. J. Press. Vessel. Pip. **85**, 30 (2008).

[14] D. F. Urban and C. Elsässer, *Atomic defects and dopants in ternary Z-phase transition-metal nitrides Cr M N with M= V, Nb, Ta investigated with density functional theory,* Phys. Rev. B **96**, 104107 (2017).

[15] M. Abdolah Zadeh, S. van der Zwaag, and S. Garcia, *Routes to extrinsic and intrinsic self-healing corrosion protective sol-gel coatings: a review,* Self-Healing Mater. **1**, 1 (2013).

1

[16] Y. González-García, S. J. García, A. E. Hughes, and J. M. C. Mol, *A combined redox-competition and negative-feedback SECM study of self-healing anticorrosive coatings,* Electrochem. commun. **13**, 1094 (2011).

[17] S. R. White, N. R. Sottos, P. H. Geubelle, J. S. Moore, M. R. Kessler, S. R. Sriram, E. N. Brown, and S. Viswanathan, *Automatic Healing of Polymer Composites,* Nature **409**, 794 (2001).

[18] S. R. White, N. R. Sottos, P. H. Geubelle, J. S. Moore, M. R. Kessler, S. R. Sriram, E. N. Brown, and S. Viswanathan, *Automatic Healing of Polymer Composites,* Nature **409**, 794 (2001).

[19] A. Susa, R. K. Bose, A. M. Grande, S. Van Der Zwaag, and S. J. Garcia, *Effect of the Dianhydride/Branched Diamine Ratio on the Architecture and Room Temperature Healing Behavior of Polyetherimides,* ACS Appl. Mater. Interfaces **8**, 34068 (2016).

[20] N. Zhong and W. Post, *Self-repair of structural and functional composites with intrinsically self-healing polymer matrices: A review,* Compos. Part A Appl. Sci. Manuf. **69**, 226 (2015).

[21] M. D. Hager, P. Greil, C. Leyens, S. van der Zwaag, and U. S. Schubert, *Adv. Mater.*, Vol. 22 (2010) pp. 5424–5430.

[22] Z. Derelioglu, A. L. Carabat, G. M. Song, S. van der Zwaag, and W. G. Sloof, *On the use of B-alloyed MoSi$_2$ particles as crack healing agents in yttria stabilized zirconia thermal barrier coatings,* J. Eur. Ceram. Soc. **35**, 4507 (2015).

[23] A. S. Farle, C. Kwakernaak, S. van der Zwaag, and W. G. Sloof, *A conceptual study into the potential of $M_{n+1}AX_n$-phase ceramics for self-healing of crack damage,* J. Eur. Ceram. Soc. **35**, 37 (2015).

[24] K. Laha, J. Kyono, S. Kishimoto, and N. Shinya, *Beneficial effect of B segregation on creep cavitation in a type 347 austenitic stainless steel,* Scr. Mater. **52**, 675 (2005).

[25] N. Shinya, *Self Healing of Mechanical Damage in Metallic Materials,* Adv. Sci. Technol. **54**, 152 (2008).

[26] R. N. Lumley, A. J. Morton, and I. J. Polmear, *Enhanced creep performance in an Al-Cu-Mg-Ag alloy through underageing,* Acta Mater. **50**, 3597 (2002).

[27] S. Zhang, C. Kwakernaak, F. D. Tichelaar, W. G. Sloof, M. Kuzmina, M. Herbig, D. Raabe, E. Brück, S. van der Zwaag, and N. H. van Dijk, *Autonomous Repair Mechanism of Creep Damage in Fe-Au and Fe-Au-B-N Alloys,* Metall. Mater. Trans. A **46**, 5656 (2015).

[28] S. Zhang, C. Kwakernaak, W. Sloof, E. Brück, S. Van Der Zwaag, and N. Van Dijk, *Self healing of creep damage by gold precipitation in iron alloys,* Adv. Eng. Mater. **17**, 598 (2015).

[29] H. Fang, C. D. Versteylen, S. Zhang, Y. Yang, P. Cloetens, D. Ngan-Tillard, E. Brück, S. van der Zwaag, and N. H. van Dijk, *Autonomous filling of creep cavities in Fe-Au alloys studied by synchrotron X-ray nano-tomography,* Acta Mater. **121**, 352 (2016).

[30] W. W. Sun, H. Fang, N. H. van Dijk, S. van der Zwaag, and C. R. Hutchinson, *Linking Surface Precipitation in Fe-Au Alloys to Its Self-healing Potential During Creep Loading,* Metall. Mater. Trans. A **48**, 2109 (2017).

[31] C. D. Versteylen, N. H. Van Dijk, and M. H. Sluiter, *First-principles analysis of solute diffusion in dilute bcc Fe- X alloys supplementary material,* Phys. Rev. B **96**, 1 (2017).

[32] C. D. Versteylen, N. K. Szymański, M. H. Sluiter, and N. H. van Dijk, *Finite element modelling of creep cavity filling by solute diffusion,* Philos. Mag. **98**, 864 (2018).

1

2

FIRST-PRINCIPLES ANALYSIS OF SOLUTE DIFFUSION IN DILUTE BCC FE-X ALLOYS

$\pi\alpha\nu\tau\alpha$ $\rho\epsilon\iota$

Heraclitus

The diffusivities of substitutional impurity elements in iron have been computed with ab-inito electronic density functional techniques, using exhange correlation (xc) functional PW91. Excess entropies and the attempt frequency for a jump were determined by calculating phonon frequencies in the harmonic approximation. The influence of the degree of spontaneous magnetisation on diffusivity is taken into account by means of the Girifalco model. The activation energy for diffusion has been determined, by computing the vacancy formation energy, impurity-vacancy binding energies, migration barrier energies, and the effective energy associated with correlation of vacancy mediated jumps. For each type of impurity atom these contributions have been evaluated and analyzed up to and including the fifth nearest neighbor shell of the impurity atom. It is found that impurities that have a low migration energy tend to have a high effective energy associated with vacancy migration correlation, and vice versa, so that the total diffusion activation energies for all impurities are surprisingly close to each other. The strong effect of vacancy migration correlation is found to be associated with the high migration energy for iron self-diffusion, so that movement of vacancies through the iron bulk is in all cases, except for cobalt, the limiting factor for impurity diffusion. The diffusivities calculated with the PW91 functional show good agreement with most of the experimental data for a wide range of elements.

2.1. INTRODUCTION

Diffusional processes in metals are relevant for a wide variety of mechanisms, such as phase transformations and partitioning. In many cases the subsititutional diffusivity is rate limiting for growth and coarsening of precipitate phases. Understanding and predicting such processes accurately requires knowledge of diffusivities of all elements present in a host. Here we present a systematic calculation of substitutional impurity diffusivities in bcc iron that makes it possible to compare the various contributing factors.

The diffusion of dilute substitutional impurities in iron has been the subject of many experimental studies[2, 3, 3–7, 7–46]. It has become apparent that in contrast to impurity diffusion in say fcc aluminum, the diffusivities of subsitutional impurities in bcc iron do not differ very much from one another. However, a comprehensive comparison of *ab initio* computed substitutional diffusivity with actual experimental data, not just the fitted parameters, is highly desirable. This is particularly the case for diffusion in iron where an Arrhenius plot does not show a simple linear relation in the ferromagnetic state. DFT calculations have proven successful in predicting experimental data such as lattice parameters[47, 48], elastic properties [49, 50], and energy barriers for diffusion, e.g. diffusivities in aluminum[51], magnesium[52, 53], and nickel[54]. Many impurity diffusivities in bcc iron[55–62] have been calculated with DFT methods, but oftentimes only experimentally fitted data, such as activation energy for diffusion, have been compared with the computed results. The fact that the Arrhenius plot of the diffusivity in bcc iron is not linear makes it desirable to compare the computed and experimentally determined diffusivities directly. This is because the determination of an activation energy for diffusion experimentally is not trivial because of the narrow temperature range available in the paramagnetic state.

The calculations were performed for the following elements (in order of atomic number): Mg, Al, Si, P, S, Ca, Ti, V, Cr, Mn, Fe, Co, Ni, Cu, Zn, Ge, Zr, Nb, Mo, Ag, Sn, Sb, Hf, Ta, W, Au, Pb and Bi. These elements were chosen to represent the entire periodic system of the elements and because of their use in the steel industry. In order to clarify trends, most elements of the 4th row, and of several columns, in the periodic table were considered. For 21 of these 28 diffusing elements the calculated results could be compared to experimental data. Some elements, such as the heavier earth alkaline species and the rare earths proved to be so large in the iron matrix that a single vacancy ($\square$) assisted impurity diffusion mechanism was deemed unrealistic. We therefore excluded the elements Sr, Ba, Ce, and La from this study.

Diffusivities in most metallic crystalline solids can be accurately described with an Arrhenius equation over a wide range of temperatures with just two parameters, the activation energy for diffusion Q and the diffusivity prefactor D_0,

$$D = D_0 e^{-\beta Q}, \tag{2.1}$$

where $\beta = 1/(k_B T)$ with k_B the Boltzmann constant and T the absolute temperature. Accordingly, for most diffusivities, an Arrhenius plot gives a straight line, but for diffusion in bcc iron there is a systematic deviation from linearity near the Curie temperature. This deviation indicates the effect of magnetic order in the bcc iron matrix. Extensive experimental work[3–6, 8, 63] has resolved that around the Curie temperature the diffusivity prefactor is relatively little affected, but that the activation energy for diffusion

changes significantly. In analogy with CsCl type ordering on a bcc lattice, as occurs in β brass Cu-Zn alloys, Girifalco[64, 65] derived a mean field model to relate the magnetic order parameter to the diffusion activation energy,

$$Q = Q_{PM}(1 + \alpha s^2),$$ (2.2)

where Q_{PM} is the diffusion activation energy in the paramagnetic state (PM), α is a dimensionless proportionality constant, and s is the (dimensionless) magnetic order parameter in the ferromagnetic state (FM). The magnetic order parameter is given as a ratio of spontaneous magnetizations: $s = M(T)/M(T = 0)$, where $M(T)$ is the temperature dependent spontaneous magnetisation in the ferromagnetic state. In the perfectly ordered ferromagnetic state, with $s = 1$ the activation energy for diffusion Q_{FM} can be computed *ab initio*, so that Q_{PM} is obtained through

$$Q_{PM} = \frac{Q_{FM}}{1 + \alpha}.$$ (2.3)

The activation energy for substitutional diffusion in a pure metal includes a vacancy formation energy and a migration energy for the actual movement of the vacancy. As these energy terms are computed within finite size supercells, rather than within a more or less infinitely large crystal, special care must be taken. To limit errors associated with wave expansions, calculations are performed in a supercell of constant (cubic) shape and volume. However, when a vacancy is introduced in such a cell, and/or when an iron atom is replaced by a large substitutional atom, under normal (practically zero external pressure) conditions, the supercell should relax to some other volume and/or shape. Therefore, we convert *ab initio* computed internal energies to zero pressure enthalpies according to

$$H[supercell] = U[supercell] + P[supercell]V_0 + \frac{1}{2}U_{int}[supercell],$$ (2.4)

where $P[supercell]$ is the hydrostatic pressure as computed *ab initio* within the fixed size supercell, and V_0 is the volume of the supercell. U_{int} is the elastic interaction between lattice defects due to periodic images that are unavoidable in supercell calculations. The energy correction has been computed using the program Aneto of Varvenne et al.[66], using the stiffness matrix parameters used to obtain the hydrostatic and dipole energies of all supercells. With the stiffness matrix (in units of GPa) is follows;

$$C_{ijkl} = \begin{bmatrix} 268.760 & 154.450 & 154.450 & 0 & 0 & 0 \\ 154.450 & 268.760 & 154.450 & 0 & 0 & 0 \\ 154.450 & 154.450 & 268.760 & 0 & 0 & 0 \\ 0 & 0 & 0 & 89.400 & 0 & 0 \\ 0 & 0 & 0 & 0 & 89.400 & 0 \\ 0 & 0 & 0 & 0 & 0 & 89.400 \end{bmatrix}.$$ (2.5)

We used supercells consisting of 4×4×4 bcc cubes with a lattice parameter of $a = 0.283$ nm, giving $V_0 \approx 1.45$ nm^3. We selected $a = 0.283$ nm because it is the zero pressure value for pure bcc iron according to the PW91 GGA exchange correlation

potential (xc-potential). At $T = 0$ K, the vacancy formation enthalpy can then be computed with

$$\Delta H_{f,\square} = H[\text{Fe}_{N-1}\square] - \frac{N-1}{N} H[\text{Fe}_N], \tag{2.6}$$

where $Fe_{N-1}\square$ refers to a supercell with $N-1$ iron atoms and a single vacancy, where N=128 for a 4×4×4 supercell.

Of course, the effect of a vacancy or impurity atom is not limited to the ground state properties, as excitations are also affected. Therefore, the formation free energy of a defect is evaluated by adding the free energy contribution due to excitations to the defect formation enthalpy. In the case of a vacancy this gives

$$\Delta G_{f,\square}(T) = \Delta H_{f,\square} + \Delta\Delta G_{exc,\square}(T), \tag{2.7}$$

where $\Delta\Delta G_{exc,\square}(T)$ is the free energy change associated with a defect (here a vacancy) due to excitations, such as related to electrons and phonons. Calculations in supercells with and without a defect give

$$\Delta\Delta G_{exc,\square}(T) = \Delta G_{exc}(T)[\text{Fe}_{N-1}\square] - \frac{N-1}{N}\Delta G_{exc}(T)[\text{Fe}_N], \tag{2.8}$$

analogous with equation 2.6. The electronic excitations are evaluated by varying the electron temperature in the Fermi-Dirac distribution function in the supercell calculations. Vibrational excitations have been evaluated in the harmonic approximation using zone-centered supercell modes. Then, the vibrational free energy G_{vib} is computed from the phonon frequencies ω_i using[67],

$$\Delta G_{vib}(T) = \sum_i \frac{1}{2}\hbar\omega_i + k_B T \ln\left(1 - e^{-\beta\hbar\omega_i}\right). \tag{2.9}$$

At high temperatures the excess vibrational free energy associated with a defect is approximately linear with temperature, $\lim_{T\to\infty} \Delta G_{vib}(T) = T \sum_i k_B \ln(\hbar\omega_i)$. The excess vibrational enthalpy difference behaves as the reciprocal of temperature and therefore vanishes. The vibrational formation energy of a vacancy is obtained through

$$\Delta\Delta G_{vib,\square}(T) \approx \Delta\Delta H_{vib,\square} - T\Delta\Delta S_{vib,\square}, \tag{2.10}$$

where, in the high temperature limit, $\Delta\Delta H_{vib,\square} = 0$ and the effective vacancy formation entropy arises from the difference between the ΔS contributions of a cell with and without a vacancy;

$$\Delta\Delta S_{vib,\square} = -\sum_i k_B \ln(\hbar\omega_i[\text{Fe}_{127}\square]) + \frac{127}{128}\sum_i k_B \ln(\hbar\omega_i[\text{Fe}_{128}]). \tag{2.11}$$

Specific to bcc iron is a correction for the diffusivity activation energy in order to capture the effect of magnetism [65], (see equation 2.2) through the relative spontaneous magnetisation s. The temperature dependence of s is accurately represented by an empirical formula[68],

$$s(\tau) = \frac{(1-\tau)^B}{1 - B\tau + A\tau^{3/2} - C\tau^{7/2}}, \tag{2.12}$$

where τ is the reduced temperature $\left(\tau = \frac{T}{T_C}\right)$, with the Curie temperature $T_C = 1043$ K in bcc iron. The constants take the values [68] $A = 0.11$, $B = 0.368$, and $C = 0.129$. The parameter α, which indicates how much the magnetic disordering affects the activation barrier for diffusion, was found to be similar for all solute elements in bcc iron. The determination of this parameter is discussed by the authors in a separate manuscript [69]. The parameter $\alpha = 0.10$ for all impurities in Fe, except for iron self-diffusion where $\alpha = 0.16$.

2.1.1. SELF-DIFFUSION

To determine the self-diffusivity $D[\text{Fe}]$, the migration energy for the movement of a vacancy to a neighboring iron atom needs to be calculated. The migration energy H_{mig} is the energy difference between energies of the transition-state (tr) and equilibrium state (eq). The rate Γ at which a vacancy trades place with its neighbor atom can then be expressed as

$$\Gamma = \nu e^{-\beta H_{mig}}, \tag{2.13}$$

where ν is the attempt frequency and where the exponential gives the probability of success. In the transition state the evaluation of the vibrational excitations requires care because of the negative curvature of the energy along the transition path. Therefore, the vibrational contribution to the migration free energy is treated according to transition state theory [70]. The effective jump attempt frequency $\tilde{\nu}$ is given by [70],

$$\tilde{\nu} = \frac{\prod \nu_i [eq]}{\prod' \nu_i [tr]}, \tag{2.14}$$

where the product of vibrational modes ($\prod \nu_i$) of a system with a vacancy is computed with a diffusing atom in the transition state ($[tr]$) and with all atoms in the equilibrium state ($[eq]$). The imaginary frequency representing the direction of the unstable vibrational mode of the transition-state is specifically excluded from the product, as is indicated by the prime in the product operator in the denominator. In our calculations, we ignore the effect of thermal lattice expansion, and the small contribution of electronic excitations is neglected also. The vacancy migration rate is then,

$$\Gamma = \tilde{\nu} e^{-\beta H_{mig}}, \tag{2.15}$$

where $\tilde{\nu}$ is given by equation 2.14, and H_{mig} is computed with

$$H_{mig} = H_{tr}[\text{Fe}_{N-1}\square] - H_{eq}[\text{Fe}_{N-1}\square], \tag{2.16}$$

where $H_{tr}[\text{Fe}_{N-1}\square]$ is the enthalpy of a supercell in the transition state (the saddlepoint configuration where an atom is about midway its jump) and $H_{eq}[\text{Fe}_{N-1}\square]$ concerns the situation prior to the jump where all atoms are still in their equilibrium positions.

The self-diffusivity $D[\text{Fe}]$ is the product of the migration rate Γ, the vacancy concentration $C_\square$, a correlation factor f and the actual jump distance l that a migrating atom travels squared,

$$D[\text{Fe}] = C_\square l^2 f \Gamma. \tag{2.17}$$

The jump distance is equal to the nearest neighbor distance $l = \frac{\sqrt{3}}{2} a$ in the case of bcc iron, where a is the bcc lattice parameter of iron. The correlation factor f describes how efficiently the vacancy contributes to the movement of iron atoms. It can be calculated with the 9-frequency model of Le Claire[71, 72], which yields a constant value $f = 0.727$ in the case of self-diffusion in bcc.

The vacancy concentration is assumed to be at equilibrium in the low concentration limit and therefore given by an Arrhenius equation with prefactor unity and with the Gibbs energy of vacancy formation $\Delta G_{f,\square}$ as,

$$C_\square = e^{-\beta \Delta G_{f,\square}}, \tag{2.18}$$

where $\Delta G_{f,\square}$ is given by equation 2.7.

2.1.2. Impurity diffusion

In comparison with self-diffusion, impurity diffusion introduces several new factors because of the interaction between impurity atom and the vacancy. One can recognize the influence of the two point defects a) on the correlation factor because of a variety of migration barriers, b) on vacancy binding at various distances from the impurity both as a binding enthalpy and as a binding entropy. First we consider how a vacancy moves in the immediate vicinity of a substitutional diffusing species via the correlation factor. Unlike in the case of self-diffusion, there are multiple jump rates because after a jump the vacancy can have a new position relative to the impurity atom, as is illustrated in figure 2.1. Each of the distinct jumps has its own migration enthalpy and its own jump rate. Of course, the migration enthalpy is generally not the same in both directions. We will assume that the jump attempt frequency, $\tilde{\nu}$ in equation 2.15, takes the value of pure iron for all jumps of iron atoms given by equation 2.14. For the Γ_2 jump, where an X impurity atom jumps, we compute the jump rate according to equation 2.14. Details concerning the attempt frequency are generally not extremely important because it varies over a relatively small range of values compared to the Boltzmann factor which varies over many orders of magnitude as function of temperature.

The correlation factor f of an impurity diffusing in a bcc system was approximated by Le Claire [71] with a model explicitly considering 9 distinct jump-rates Γ, the so-called 9-frequency model,

$$f = \frac{3\Gamma_3 + 3\Gamma_{3'} + \Gamma_{3''} - \frac{\Gamma_3 \Gamma_4}{\Gamma_4 + F\Gamma_5} - \frac{2\Gamma_{3'}\Gamma_{4'}}{\Gamma_{4'} + 3F\Gamma_0} - \frac{\Gamma_{3''}\Gamma_{4''}}{\Gamma_{4''} + 7F\Gamma_0}}{2\Gamma_2 + 3\Gamma_3 + 3\Gamma_{3'} + \Gamma_{3''} - \frac{\Gamma_3 \Gamma_4}{\Gamma_4 + F\Gamma_5} - \frac{2\Gamma_{3'}\Gamma_{4'}}{\Gamma_{4'} + 3F\Gamma_0} - \frac{\Gamma_{3''}\Gamma_{4''}}{\Gamma_{4''} + 7F\Gamma_0}}, \tag{2.19}$$

with the factor $F = 0.512$.

The correlation factor f, equation 2.19, depends on temperature because each of the Γ varies with temperature (eq. 2.15). The influence of temperature on the correlation factor can be quite significant for elements with large variations in $\Delta H_{mig,i}$. In spite of the complex formal temperature dependence of the correlation factor, usually it is well approximated by a simple Arrhenius equation because one of the jump frequencies Γ_i tends to become the bottleneck in the diffusive process. A simple analysis of equation 2.19 shows that the numerator is dominated by the largest terms; either Γ_3, $\Gamma_{3'}$,

or $\Gamma_{3''}$. If the largest Γ in the numerator is larger than Γ_2 in the denominator, f will be approximately unity almost independent of temperature. However, if Γ_2 is larger than the largest Γ in the numerator, their ratio will be a good estimate of f,

$$f \approx \frac{\max(\Gamma_3, \Gamma_{3'}, \Gamma_{3''})}{\max(\Gamma_2, \Gamma_3, \Gamma_{3'}, \Gamma_{3''})}. \tag{2.20}$$

The jump rates are all Boltzmann factors, so that f is approximated by an Arrhenius equation. This leads to the definition of an effective entropy and effective enthalpy of correlation by fitting a linear relation between $\ln(f)$ and β,

$$\ln(f) \sim \Delta S_c / k_B - \beta \Delta H_c. \tag{2.21}$$

The approximation for f in equation 2.20 then yields for

$$\Delta H_c \approx \max[0, \min(H_{mig,3}, H_{mig,3'}, H_{mig,3''}) - H_{mig,2}]. \tag{2.22}$$

When fitting within the temperature range between 600 and 1200 K and accounting for the negative terms in the numerator and denominator in equation 2.19, it is found that a minor rescaling is required which gives

$$\Delta H_{c,approx} = 1.2 \max[0, \min(H_{mig,3}, H_{mig,3'}, H_{mig,3''}) - H_{mig,2}]. \tag{2.23}$$

The effective entropy of correlation is not easily estimated by an approximate expression.

The impurity-vacancy binding at various separation distances is temperature dependent and thus can be thought of as both a binding enthalpy and as a binding entropy.
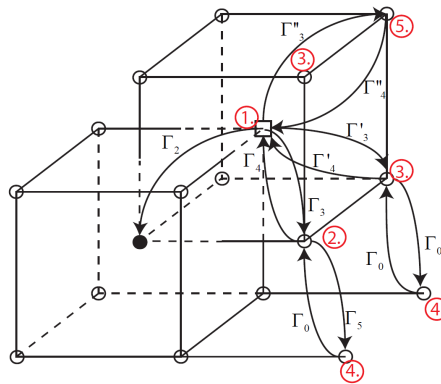
Figure 2.1: The 9 frequency model by Le Claire [71]. Each distinct jump frequency is indicated, and with the red numbers indicating the nearest neighbor with respect to the impurity atom. Γ_2 concerns the impurity trading places with the vacancy, Γ_3 concerns an iron atom that is a 2nd neighbor of the impurity exchanging with a vacancy and thereby becoming a nearest neighbor to the impurity, Γ_4 is the reverse of Γ_3, $\Gamma_{3'}$ is a jump whereby an iron atom changes from a first to a third neighbor of the impurity, $\Gamma_{4'}$ is the reverse of $\Gamma_{3'}$, an iron atom jumping from 1st to 5th impurity neighbor is $\Gamma_{3''}$, and $\Gamma_{4''}$ is the reverse of $\Gamma_{3''}$. All other jump frequencies are assumed to be unaffected by the presence of a substitutional solute and are assumed to take the same value as the one in pure iron bulk Γ_0.

The enthalpy differences at zero pressure are evaluated with,

$$\Delta H_{bind,X\square}(\mathbf{R}_j) = H[\text{Fe}_{N-2}X\square](\mathbf{R}_j) - H[\text{Fe}_{N-1}X] - H[\text{Fe}_{N-1}\square] + H[\text{Fe}_N], \quad (2.24)$$

where each of the supercell enthalpies have been computed using equation 2.4, and where $\mathbf{R}_j$ indicates the shortest vector that separates X and $\square$. The entropic binding terms then arise from electronic, magnetic, and vibrational excitations. The electronic excitations are easily incorporated self-consistently through the Fermi-Dirac distribution function. We find these effects to be negligible. The magnetic excitations are globally included through the Girifalco model. Of course, magnetic behavior, and its temperature dependence, must be expected to differ from the global pure Fe bulk in the vicinity of a defect. We have chosen to neglect such local defect-induced excess terms. The excess vibrational free energy associated with vacancy-impurity binding has been calculated from supercells with and without defects, analogeous to equation 2.11.

$$\Delta\Delta S_{bind,X\square}(\mathbf{R}_j) = -\sum_i k_B \ln(\hbar\omega_i[\text{Fe}_{N-2,X,\square}]) +$$
$$\sum_i k_B \ln(\hbar\omega_i[\text{Fe}_{N-1,X}]) + \sum_i k_B \ln(\hbar\omega_i[\text{Fe}_{N-1,\square}]) -$$
$$\sum_i k_B - \ln(\hbar\omega_i[\text{Fe}_N]). \quad (2.25)$$

As indicated in equation 2.10, the excess vibrational free energy can be separated in a vanishing excess vibrational enthalpy $\Delta H_{vib,X\square}(\mathbf{R}_j)$ and an approximately temperature-independent vibrational impurity-vacancy binding entropy $\Delta S_{vib,X,\square}(\mathbf{R}_j)$ term. The activation barrier for diffusion in the fully ferromagnetically ordered state is calculated as the sum of the various contributions,

$$Q_{FM} = \Delta H_{f,\square} + \Delta H_{bind,X\square}(\mathbf{R}_1) + \Delta H_{mig,2} + \Delta H_c. \quad (2.26)$$

where $\mathbf{R}_1$ indicates a nearest neighbor in the bcc crystal structure. The paramagnetic activation energy for diffusion is computed from Q_{FM} with equation 2.3. The pre-exponential factor D_0, in equation 2.1 is calculated in the purely ferromagnetic state and is assumed to be the same for PM and FM states. This is justified by the relatively small shifts in phonon frequencies [73–75]. In addition, the shift in phonon frequencies are gradual with temperature [76, 77]. The entropy contribution which originates from the correlation is modest and the difference with magnetic order is expected to be small as well.

$$D_0 = \frac{3}{4} a^2 \tilde{\nu}_2 e^{(\Delta\Delta S_{vib,\square} + \Delta\Delta S_{bind,X\square}(\mathbf{R}_1) + \Delta S_c)/k_B}, \quad (2.27)$$

where $\Delta\Delta S_{vib,\square}/k_B$ applies to pure iron.

2.2. FIRST-PRINCIPLES CALCULATIONS

Enthalpies (total energies) have been computed within the local density approximation using the Vienna *ab initio* simulation program (VASP) [78, 79] version 5.2 at a pressure of 0 GPa. The calculations were performed using pseudopotentials of the projector

augmented wave (PAW) type [80]. Standard potentials were used[81], except for atoms much larger than Fe where harder potentials with semicore states treated as valence states were used: Bi_d, Ca_pv, Ge_d, Hf_pv, Mo_pv, Nb_pv, Pb_d, Sn_d, Ta_pv, Ti_pv, V_pv, W_pv and Zr_sv. Supercells with $4 \times 4 \times 4$ conventional bcc cubes (128 lattice sites) were employed, with $5 \times 5 \times 5$ Γ-centered k-point grids in the case of the vacancy formation energies and migration barriers with an energy cutoff of 400 eV for plane wave expansions. For the vacancy-impurity binding phonon calculations the cutoff frequency was chosen to be 440 eV, in $3 \times 3 \times 3$ bcc supercells with $4 \times 4 \times 4$ Γ-centered kpoint grids. All calculations were spin-polarized. Migration barriers have been calculated with the nudged-elastic band (NEB) method with the climbing image algorithm[82]. Elastic energy corrections for image interactions associated with supercells were made using the method of Varvenne et al.[66]. The elastic interaction energy is computed from the pressure and the deviatoric stress computed *ab initio* within supercells with fixed volume and fixed (cubic) shape. Elastic energy corrections for image interactions were typically in order of meVs at most for the $4 \times 4 \times 4$ supercells, with the larger values occurring for the transition state configurations. In our calculations two GGA exchange-correlation (xc) functionals were used: PW91 [83, 84] and PBEsol[85]. The PBEsol xc functional was designed with the aim to correct for an inaccuracy in predicted lattice constants of PW91 and PBE. The overestimation of lattice parameters (in the case of PBE) coincides with an underestimation of the bulk modulus of pure metals, PBEsol is reported to give a better approximation for many different pure metals [48]. However, PBEsol for bcc iron fails at predicting the lattice parameter, giving 2.79 Å [86], to be compared with an experimental value of about 2.86 Å. At the theoretical lattice parameter (2.79 Å), PBEsol gives a rather high vacancy formation enthalpy [47, 87], about 2.47 eV, which is beyond the currently general accepted value of about 2.2 eV[47, 58, 88–91]. The results of the PBEsol calculated energies are therefore presented only in table 2.1 and in the supplementary material [1]. The PBEsol computed value increases to even higher values when a more realistic value for the lattice parameter is selected [47]. At the bcc lattice parameter selected in this work, 2.83 Å, the PW91 equilibrium value, it is to be expected that too large a vacancy formation enthalpy is computed for PBEsol. However, recent work by Glensk et al.[92] has called into question the validity of currently generally accepted vacancy formation enthalpies, so that we find it of interest to consider the PBEsol functional.

2.3. Results & discussion

2.3.1. Vacancy formation and impurity-vacancy binding enthalpy

The vacancy formation enthalpy in pure bcc iron was computed with equation 2.6, see table 2.1. Table 2.1 shows that there is agreement with previously published data. Our PW91 vacancy formation enthalpy is in the middle of the range of values reported in the literature and it agrees nicely also with results published for the PBE GGA [93]. PBEsol rather consistently gives values almost half an eV higher than PW91 and PBE.

The vacancy formation vibrational entropy, see equation 2.10, in bcc iron is computed to be about 4.14 k_B for PW91 in a $4 \times 4 \times 4$ supercell. This value is in good agreement with the value obtained by Lucas and Schäublin [95] $S_{vib,\square} = 4.08\ k_B$, and in a little less close

Table 2.1: Calculated vacancy formation enthalpies ($\Delta H_{f,\square}$) calculated with equation 2.6 and entropies ($\Delta\Delta S_{vib,\square}$), calculated with equations 5 and 10, comparison of various exchance-correlation (xc) functionals.

xc type	$\Delta H_{f,\square}$ (eV)	$\Delta\Delta S_{f,vib,\square}$ (k_B)
PW91	2.129 [this work]	4.14 [this work]
PW91	2.02 [57]	-
PW91	2.0[94]	-
PW91	2.16[89]	-
PW91	2.16[47]	-
PW91	2.16[95]	4.08[95]
PBE	2.18[96]	4.62[96]
PBE	2.13[88]	-
PBE	2.23[58]	-
PBE	2.01[90]	-
PBE	2.22[47]	-
PBE	2.31[91]	-
PBEsol	2.626 [this work]	-
PBEsol	2.47[47]	-
revTPSS	2.64[47]	-

agreement with the value by Messina et al.[97] $S_{vib,\square} = 4.6$ k_B. The vacancy formation vibrational entropy obtained in a 3×3×3 supercell is 3.79 k_B, quite close to our 4×4×4 result. In view of the computational resources needed, and the relatively small effect on the diffusivity, we use the 4×4×4 result for the vacancy formation vibrational entropy, and the 3×3×3 supercell results for the vacancy-impurity binding entropy. The vacancy formation vibrational entropy is quite large in comparison to other single site excess entropies: the configurational entropy in real alloys and entropy differences between allotropes are usually in the neighborhood of 1 k_B or less.

The impurity - vacancy binding enthalpies, computed with equation 2.24, are plotted in figure 2.2. These enthalpies correlate well with the columnar position in the periodic table of the elements of the impurity atom. The row position of the impurity atom is less discriminating; for elements in the same column row 5 and row 6 differ little from one another. There is a minimum at the edges of the periodic system of the transition metals in each row of the periodic table. Of course, atoms at the middle of the transition metal series are usually smallest confirming a well-documented relation to atomic sizes[51, 52]. There have been several studies of vacancy-impurity binding in bcc iron [58–60, 62, 98, 99] and our results mostly agree with previous calculations with a few notable exceptions: For cobalt our results, and those of Olsson et al. [99] and Messina et al. [62], are in marked contrast to those of Ohnuma et al. [98]. For nickel we agree with refs. [62, 99], but disagree with those of Vincent et al. [59]. For copper our results are closest to those of Ohnuma et al. [98], and close to those of refs. [62, 99], but differ significantly from others [59, 60]. For Mo we agree with Huang et al. [58] and refs. [62, 99], but not with Ohnuma et al. [98]. For some elements we did not find literature values to compare with: Bi, Ca, Ge, Mg, Pb, and Sn. Details for
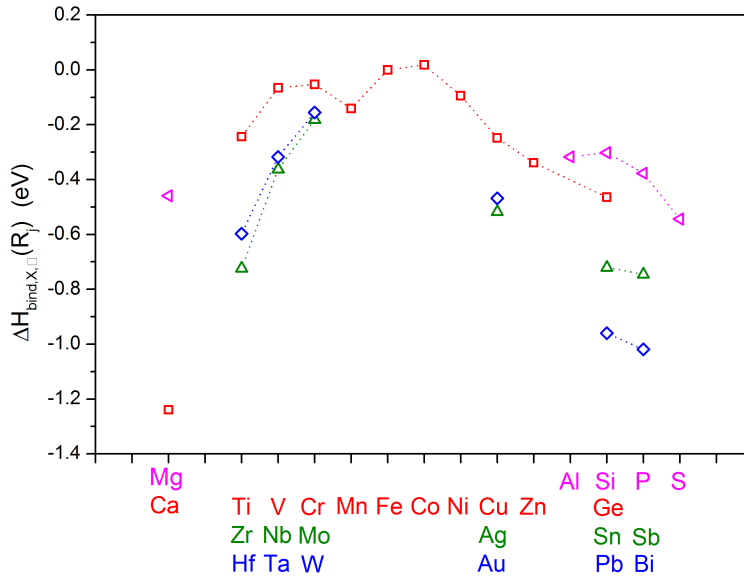
Figure 2.2: Vacancy binding enthalpy next to a single impurity atom as computed with 2.24 using PW91. Impurity elements are arranged by row and column of the periodic system, row 3 of the periodic system (purple triangles), row 4 of the periodic system (red squares), row 5 of the periodic system (green triangles), row 6 of the periodic system (blue diamonds). Dashed lines, between neighboring impurities, are guides to the eyes only.

the impurity-vacancy binding up to the 5th shell for all impurities can be found in the supplementary information [1].

The vacancy-impurity binding enthalpy varies rather systematically with distance as can be seen in figure 2.3 and was also reported by others[62, 99]: relative to the binding with the 1st nearest neighbor, the 2nd neighbor binding is a bit weaker, at the 3rd and 4th neighbors the binding is much weaker, while at the 5th neighbor, it is again stronger, but weaker than at the 1st and 2nd neighbors. This can be rationalized by the strong transmission of strain effects along a dense packed direction, such as applies to the 1st and 5th neighbors.

2.3.2. MIGRATION BARRIERS

The migration enthalpies of various impurity elements in iron and the barriers of the iron atoms in the vicinity of the impurity were computed with equation 2.16. Large impurity atoms, such as towards the left and right extremities of the periodic table, have low values for $\Delta H_{mig,2}$, see figure 2.4. Impurities close to Fe in the middle of the periodic table have $\Delta H_{mig,2}$ of similar magnitude as ΔH_{mig} for iron self-diffusion with the exception of Mn, which has a much lower barrier. This trend was reported by Ding

2

Figure 2.3: Vacancy-impurity binding enthalpy for impurities in the 4th row of the periodic table as computed with equat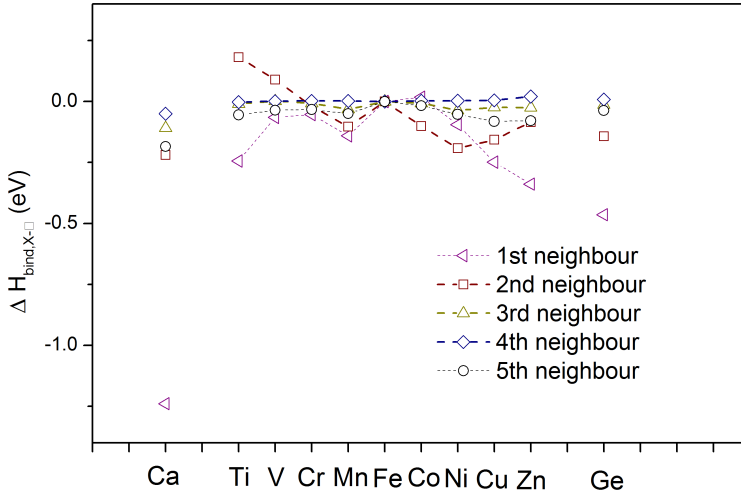ion 2.24 using PW91. Nearest neighbors: pink squares, 2nd neighbors: red diamonds, 3rd neighbors: green triangles, 4th neighbors: blue circles, 5th neighbors: black X-es.

et al.[61] and Messina et al.[62] also. It has been found for TM impurities diffusion in fcc Ni as well [54]. The inverse relation between the magnitude of $\Delta H_{mig,2}$ and atomic size, has been rationalized through the displacement of the large impurity atom towards the vacancy. This results in short jump distances and correspondingly low barriers [51]. Very large impurity atoms such as Sr, Ba, Ce, and La, take an intermediary position between the original position and the neighboring vacancy, forming a vacancy-impurity atom complex. Such complexes can probably only migrate when an additional vacancy approaches. Such double-vacancy assisted diffusion processes have not been explored in the current work. For calcium a nearest-neighbor jump although shortened, still can be defined, but the associated migration enthalpy is 19 meV only. In such a case the Ca atom frequently jumps back and forth without any net displacement, and diffusion of the calcium atom is going to be determined by how the vacancy migrates through the neighboring bulk, that is, it will be determined by the correlation factor, as will be discussed below.

Large impurity atoms, at the left and right sides of the periodic table, generally have strong vacancy binding, see figure 2.2. As a result their migration barriers for dissociative jumps $\Delta H_{mig,3}$, $\Delta H_{mig,3'}$, and $\Delta H_{mig,3''}$ tend to be much larger than the corresponding barriers for associative jumps $\Delta H_{mig,4}$, $\Delta H_{mig,4'}$, and $\Delta H_{mig,4''}$. For many larger atoms $\Delta H_{mig,4''}$ is the lowest barrier (Ca, Zr, S, Hf, Pb, Bi, Ge, P, Sn, Mn, Sb, Si, Cu, Cr,

Au, W), for a others (Mg, Nb, Ti, Zn, Ag, Al, Ta, V, Mo) it is $\Delta H_{mig,4'}$. For Co and Ni only, we find $\Delta H_{mig,3}$ to be the lowest barrier. Not surprisingly Ni has almost no vacancy binding, and Co is the only element (in our analysis) that we found that repels a vacancy at the nearest neighbor shell in bcc Fe.

The migration enthalpies for all the impurity species form a large data set. Therefore, all detailed information concerning migration enthalpies is tabulated (table III) in the supplementary material [1], with a detailed comparison to literature data.

2.3.3. CORRELATION FACTOR

Using equation 2.19, the correlation factor for each impurity species has been computed as function of temperature. As the correlation factor is found to be described rather well by an Arrhenius relation, an effective entropy and effective enthalpy of correlation has been defined (equation 2.21). ΔH_c is significant for several impurity species, especially for impurity species at the far left and far right of the periodic table, see figure 2.6. This result relates with the finding that large impurity atoms diffusing in a Mg matrix also feature significant effective correlation enthalpies[52, 53]. However, position in the periodic table gives a more significant correlation than atomic size. Tungsten and gold are larger atoms than chromium and copper, but the latter two have larger effective

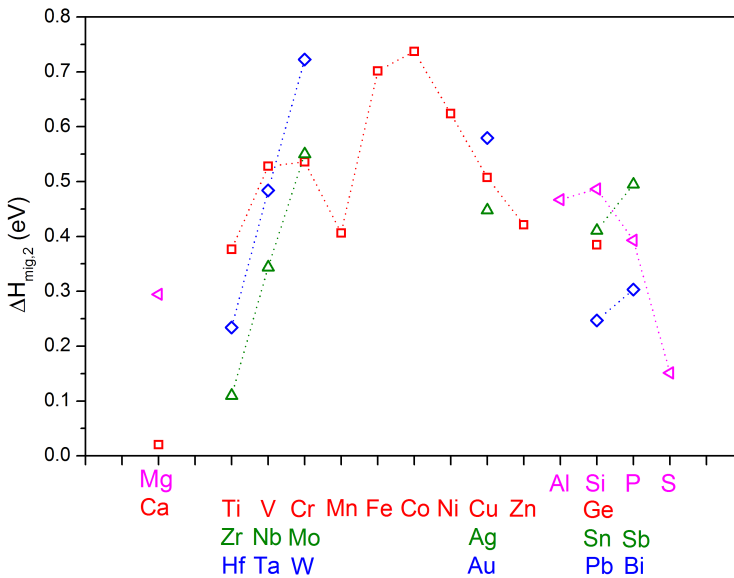Figure 2.4: Migration enthalpy $\Delta H_{mig,2}$ of impurity elements calculated with equation 2.16, arranged by row and column of the periodic table, row 3 of the periodic system (purple triangles), row 4 of the periodic system (red squares), row 5 of the periodic system (green triangles), row 6 of the periodic system (blue diamonds). Dashed lines, between neighboring impurities, are guides to the eyes only.

correlation enthalpies. Likewise sulfur, phosphorous, and germanium have much larger effective correlation enthalpies than their atomic size in the bcc Fe matrix would suggest, but they are clearly far to the right from Fe in the periodic table. For elements with large ΔH_c one cannot neglect the temperature dependence of the correlation factor, as has been found in Mg also [52, 53]. An analysis of the expression for the correlation factor has revealed that an approximate analytic expression can be derived, (see equation 2.23). In figure 2.5 the accuracy of the approximate expression can be gauged. The approximation deviates typically by up to about 5% of the value obtained by fitting according to equation 2.21 with f from equation 2.19. Eqn. 2.23 also suggests a negative correlation between ΔH_c and $\Delta H_{mig,2}$. This is confirmed by the opposite tendencies in figure 2.6 and figure 2.4. When ΔH_c is plotted as function of $\Delta H_{mig,2}$, in figure 2.7, this negative correlation is evident. Clearly, when the activation energy of diffusion is computed, using equation 2.26, two element specific terms, ΔH_c and $\Delta H_{mig,2}$ have the tendency to compensate one another. As a result, the activation energy of impurity diffusion in bcc Fe does not vary nearly as much as in some other metallic matrices, e.g. fcc Al [51]. It is clear that the temperature dependence of the correlation factor should not be ignored, in contrast to some previous studies [55, 58, 61, 61, 89]. Fortunately for elements close to iron in the periodic table ΔH_c is relatively small, see figure 2.4. Evaluating the
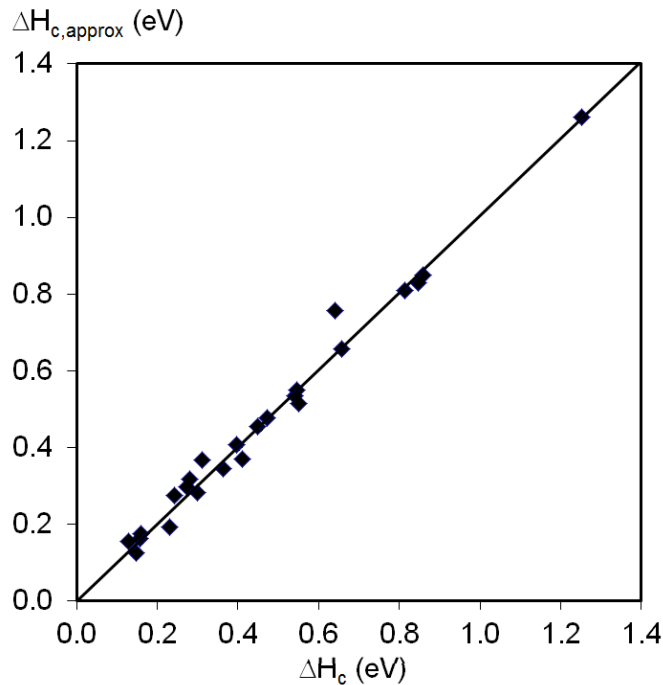

Figure 2.5: Effective enthalpy associated with correlation as estimated from equation 2.23, $\Delta H_c[approx]$ as function of the ΔH_c obtained from equation 2.21 within the temperature range of 600 K to 1200 K for all elements considered in this study. The most overestimated value pertains to sulfur.
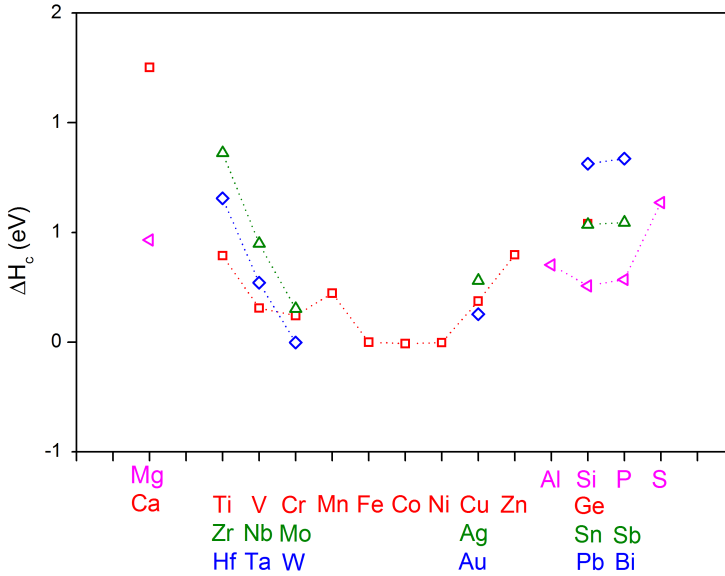
Figure 2.6: Effective enthalpy of correlation calculated with equation 2.21 derived from the temperature relation of correlation factors of impurity elements, arranged by row and column of the periodic system, row 3 of the periodic system (purple triangles), row 4 of the periodic system (red squares), row 5 of the periodic system (green triangles), row 6 of the periodic system (blue diamonds). Dashed lines, between neighboring impurities, are guides to the eyes only.

correlation factor at one specific temperature[100] is thus likely to give a large error in the calculated diffusion activation energy of yttrium, titanium and zirconium.

The effective entropy associated with correlation as obtained by fitting to equation 2.21 within T=600 K to 1200 K is much less transparent. For Fe self diffusion, where all Γ_i take the same value, this gives $\Delta S_c = -0.32 k_B$. Likewise, when

$$\min(H_{mig,3}, H_{mig,3'}, H_{mig,3''}) < H_{mig,2}, \qquad (2.28)$$

such as for Co, Ni, and W, equation 2.20 yields a temperature independent value of f with $\Delta S_c \approx -0.32 k_B$. For the other impurity elements $\Delta S_c / k_B$ generally takes small positive values, in the neighborhood of unity, except for Ge, Zn and Ca where $\Delta S_c / k_B \approx 2$. Recently, a more accurate expression for the correlation factor has been derived [62] where the jump rate between 2nd and 4th impurity atom neighbors is not equated to the bulk jump rate. Use of this equation did not yield any significant changes in our qualitative or quantitative results.

2.3.4. DIFFUSIVITIES
For the calculation of diffusivities of impurities in iron, we examine first the parameters for the fully FM state as given by eqns. 2.26 and 2.27. The element-specific terms

2
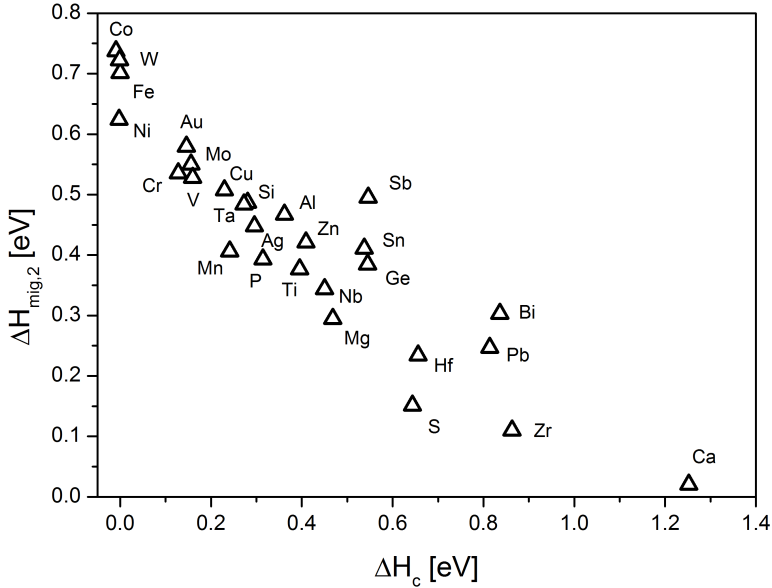
Figure 2.7: ΔH_c from equation 2.21 as function of $\Delta H_{mig,2}$.

in equation 2.27 are $\tilde{\nu}_2$, ΔS_c, and $\Delta S_{vib,X\square}(\mathbf{R}_1)$, the other factors being independent of impurity species. The effective attempt frequency for the diffusing species, $\tilde{\nu}_2$, has been computed using equation 2.14, see figure 2.8 and table II of the supplementary material [1]. table II shows a number of remarkable results: For the 3d transition metal (TM) impurities attempt frequencies are generally high, with a remarkable dip for Mn in the middle of the series. The early 4d and 5d TM impurities are rather similar and have markedly lower attempt frequencies than the corresponding 3d TM impurities. The late TMs, Cu, Ag, and Au, all have rather similar attempt frequencies, in spite of their significant differences in atomic mass. Both the described tendencies and numerical values agree well with those found by Messina et al. [62]. Our frequencies are typically about 10% higher than those reported previously [62], which may be related to our somewhat smaller bcc lattice parameter. Given a typical temperature of 1000 K, a 10 % error in the attempt frequency, gives the same deviation in the computed diffusivity as an error in the diffusion activation energy of 8 meV. Concerning tendencies for frequencies of non-TM impurities, the rather low values stand out. These elements, such as Ca, Mg, Zn, Al, Si, Ge, Sn, Pb, P, Sb, and Bi all fall in the range of 1 to 5 THz, except S at 0.44 THz. Non-TM elements have lower frequencies further down in the same column of the periodic system, as is seen in the comparison Mg-Ca, Si-Ge-Sn-Pb, and Sb-Bi. The 3p series Al-S also shows a marked decrease of frequencies as the number of p-electrons increases, with a value of about 5 THz for Al and a very low value of 0.44 THz for S (figure 2.8). We also applied a Meyer-Neldel fit to attempt frequency - $\Delta H_{mig,2}$. As

before [62], the fit to the 3d TMs is very poor, but the fit to 3p elements [Al-S]also does not yield a physically significant result [101]. For the 3p elements an exponent of 0.507 and a Meyer-Neldel energy of 0.014 eV, as well as a reference frequency ν_0 of 0.01 THz is found. These parameters differ strongly to what has been found for the 4d and 5d TM impurities [62], and appear to be closer to other analyses [102, 103]. However, an alternate Meyer-Neldel analysis of the computed $\log(D_0)$ versus $\Delta H_{mig,2}$ values does not yield a significant correlation because the D_0 are similar for all impurity elements considered. Therefore, the Meyer-Neldel analysis does not appear particularly useful for substitutional impurity diffusion in bcc iron.

The vibrational impurity-vacancy binding entropy, $\Delta S_{vib,X\square}(\mathbf{R}_1)$, ranges from about -0.5 to +1.5 k_B 2.9. The largest value is reached for Ca, and the smallest for Mg. For TM, values of about +0.5 k_B are common, while for non-TM, lower values predominate. Our data did not allow us to recognize any clear trends. Meyer-Neldel type correlations between $\Delta S_{vib,X\square}(\mathbf{R}_1)$ and $H_{mig,2}$ or Q_{FM} are not significant, reinforcing our conclusion that a Meyer-Neldel analysis is not particularly revealing.

The element-specific terms in equation 2.26, $\Delta H_{bind,X\square}(\mathbf{R}_1)$, $\Delta H_{mig,2}$, and ΔH_c have all been discussed above already, so that here we examine Q_{FM}. The activation energy for diffusion ranges from about 2 to 3 eV figure 2.10, with most TM impurities
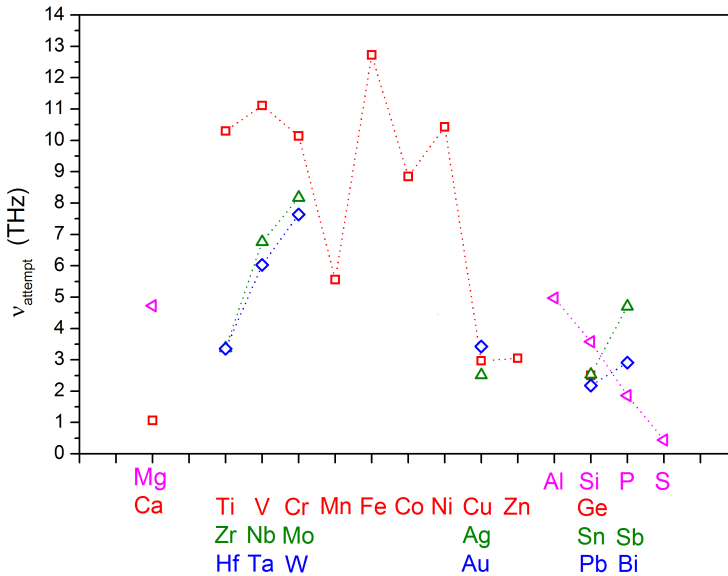
Figure 2.8: The attempt frequencies for an impurity jump in iron calculated with equation 2.14, arranged by row and column of the periodic system, row 3 of the periodic system (purple triangles), row 4 of the periodic system (red squares), row 5 of the periodic system (green triangles), row 6 of the periodic system (blue diamonds). Dashed lines, between neighboring impurities, are guides to the eyes only.

within the range of 2.4 to 2.8 eV. This is in marked contrast to activation energies for subsitutional impurity diffusion in metals such as Al [51] or Mg [52, 53]. The activation energy for TM impurities in aluminum can be twice that of aluminum self diffusion while non-TM impurities often have activation energies which are very similar to that of the host [51, 104]. The activation energies for the p-type elements in bcc iron show some interesting trends. The 3p impurities, Al-Si-P-S, display a monotonic decrease in diffusion activation energy in bcc Fe as the number of p electrons is increased. Along the columns of the periodic table too, a tendency is apparent where elements of the lower rows feature lower activation energies than those of the upper rows; Si-Ge-Sn-Pb, and P-Sb-Bi. This tendency is already recognizable in the vacancy-impurity binding enthalpy and also in the impurity nearest neighbor migration enthalpy. Increasing p-electron count strengthens the pd hybridization and thereby makes the vacancy-impurity binding increasingly less favorable. Furthermore, the loss of a number of nearest neighbors in the transition state is energetically less costly for a more covalently bonded element than for a metallicly bonded element. Therefore the migration energy is lowered as the p-electron count increases. Of course, impurities further down a given column in the periodic system with their increased atomic size relax more toward the vacancy position, and have p-bands that are wider and better aligned with the iron d-bands to
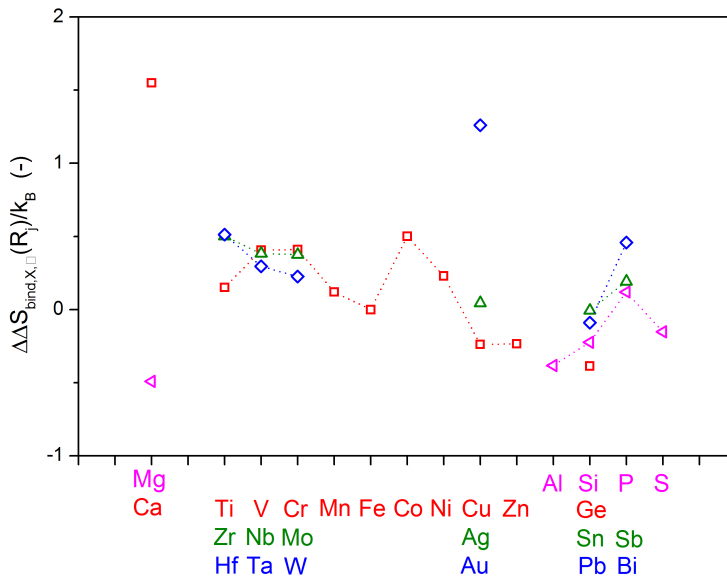
Figure 2.9: The impurity-vacancy binding entropy of in units of k_B, arranged by row and column of the periodic system, row 3 of the periodic system (purple triangles), row 4 of the periodic system (red squares), row 5 of the periodic system (green triangles), row 6 of the periodic system (blue diamonds). Dashed lines, between neighboring impurities, are guides to the eyes only.

give a further decrease in migration energies.
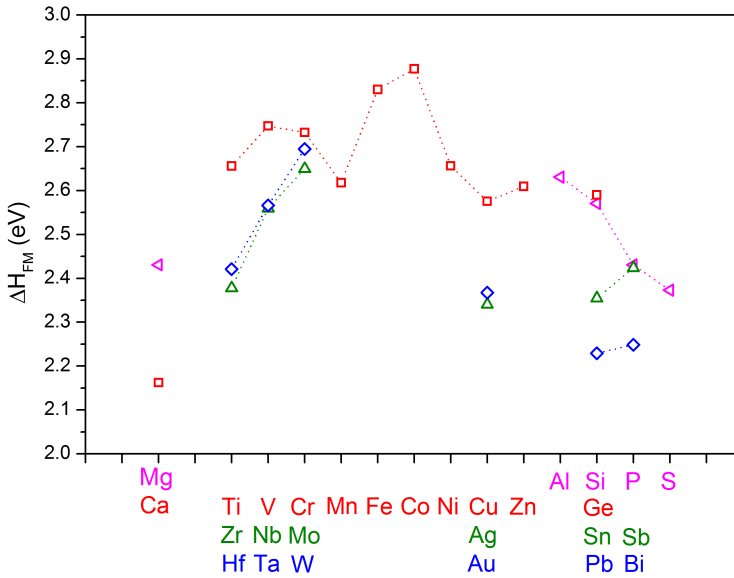
Figure 2.10: PW91 total activation energies in fully ferromagnetic state of impurity elements, arranged by row and column of the periodic system, row 3 of the periodic system (purple triangles), row 4 of the periodic system (red squares), row 5 of the periodic system (green triangles), row 6 of the periodic system (blue diamonds). Dashed lines, between neighboring impurities, are guides to the eyes only.

A comparison of the computed impurity diffusivities with experimental data as function of temperature requires consideration of the effect of magnetic (dis)ordering. The paramagnetic activation barrier has been computed in pure iron by Ding et al. [75] via the spin-wave method [74]. This provides a description of pure iron paramagnetic diffusion, however to apply it for all impurity elements would not be trivial. Fortunately, the results [75] strongly resemble that of the semi-empirical Girifalco model [65] so that we will be using that method here, just as was done in most diffusivity studies with regard to bcc iron so far. Our detailed review of experimental impurity diffusivities above and below the Curie temperature [69] has revealed that the Girifalco α parameter, see equation 2.2, for all impurities in the dilute limit can be reasonably chosen as $\alpha = 0.10$, with the exception of iron self diffusion for which $\alpha = 0.16$ is in better agreement with the majority of experimental data.

The diffusivities of impurity elements in bcc iron calculated with PW91 agree well with the experimental results. The diffusivities of impurities in bcc iron are close together experimentally, which is reflected in the calculated results. The greatest deviation between calculated and experimental results are in overestimating the diffusivities of Mn, Zn, Nb, Ta, and Au in bcc iron figure 2.12. For those elements that are not compared to

2
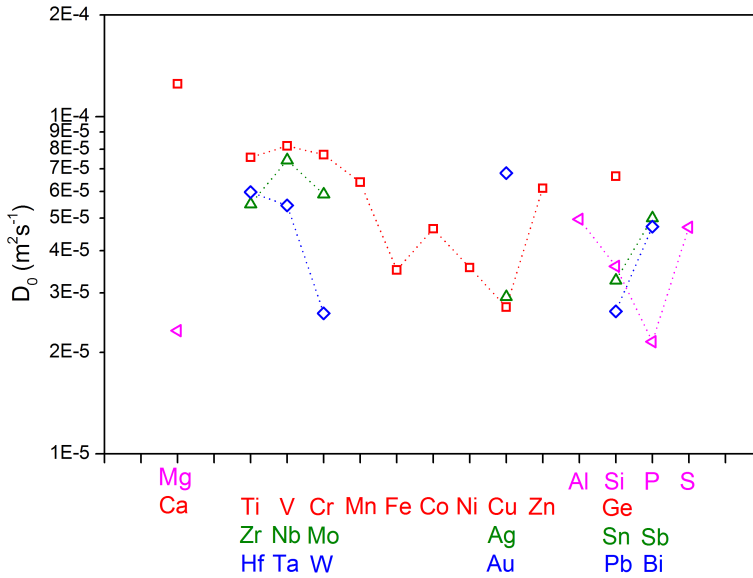
Figure 2.11: Prefactor to diffusion, calculated with 2.27. values are arranged by row and column of the periodic system, row 3 of the periodic system (purple triangles), row 4 of the periodic system (red squares), row 5 of the periodic system (green triangles), row 6 of the periodic system (blue diamonds). Dashed lines, between neighboring impurities, are guides to the eyes only.

experiments the diffusivities are presented in figure 2.13. Notably high diffusivities are found for Pb and Ca in bcc iron, this coincides with a very low solubility. The reason for this seem to be underestimated activation barriers, which is especially seen in the low temperature deviation between the PW91 line and experimentally measured points. In other cases there is an overestimation of diffusivity as calculated by PW91. The reason for this seems similar, but opposite, in the way that there is a discrepancy in the slope of the diffusivities.

The agreement with measured diffusivities is very good in most cases, especially considering the discrepancy between various experimental datasets of dilute impurity diffusion. The methodology presented here provides reliable results for the determination of diffusivity in bcc iron.

The results for the vacancy binding energies, migration barriers and diffusivities are compared (in the appendix) to the calculated results of[55, 57, 58, 61, 62, 89, 91, 94, 100, 105] for which migration barriers were found to be very similar in all cases. Differences are found in vacancy formation energies, which is very sensitive to the type of exchange-correlation functional.

One general trend captured very well in the calculations is that all diffusivities are very close together for impurities in bcc iron. This indicates a similar mechanism and
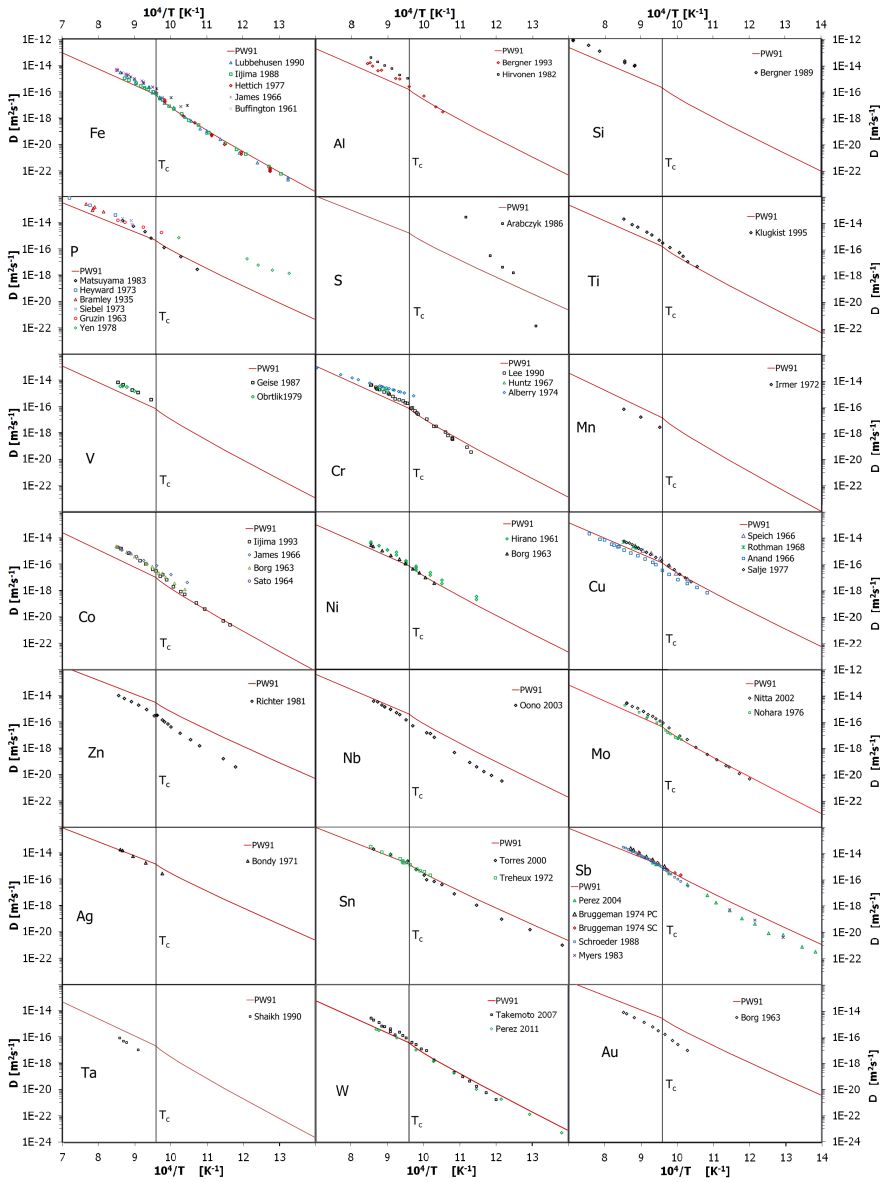
Figure 2.12: The diffusivity as calculated with the PW91 xc functional (red lines), compared to experimental data of Fe[4–8] self-diffusion and dilute impurity diffusion of; Al[9, 10], Si[11], P[12–17], S[18], Ti[19], V[20, 21], Cr[22–24], Mn[25], Co[3, 7, 26, 27], Ni[3, 28], Cu[29–32], Zn[33], Nb[34], Mo[35, 36], Ag[37], Sn[38, 39], Sb[40–43], Ta[44], W[45, 46], and Au[3]. The Curie temperature (T_C) is indicated by a vertical black line in all panels.

2
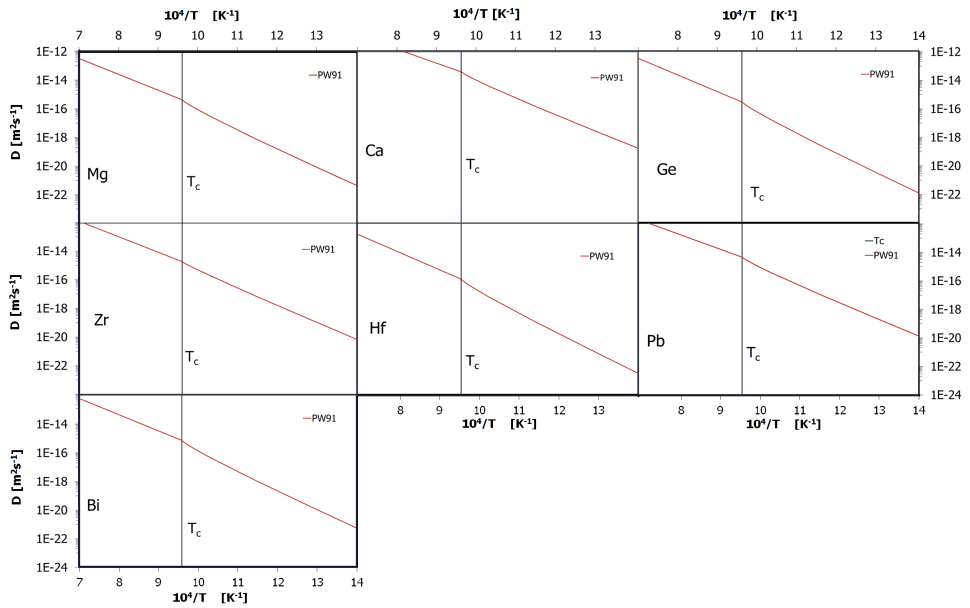
Figure 2.13: The impurity diffusion of elements Mg, Ca, Ge, Zr, Hf, Pb, and Bi in bcc iron. Diffusivities as calculated with the PW91 xc functional (red lines). The Curie temperature (T_C) is indicated by a vertical black line in all panels.

as well a rate of diffusion which is determined by the self-diffusion of vacancies in the iron matrix. The trend that the activation energy for diffusion is dependent on the column of the periodic system, is captured both by the diffusivity calculations and the comparison to experiments. This makes the trends captured by these calculations very useful to predict the diffusivities of those elements whose diffusivities have not yet been determined experimentally.

2.4. CONCLUSIONS

Diffusivities of a large number of impurities in bcc iron have been calculated by means of first-principle methods. The selection of the elements in the periodic table gives a good overview of all single-vacancy diffusing elements. The magnitude of the vacancy formation energies is highly dependent on the chosen exchange-correlation functional, unlike the magnitude of migration barriers.

The magnitudes of the nearest neighbor barriers, vacancy formation and binding energies are correlated to the position of the element in the periodic system; with low values on each end of the columns of the periodic system. This is compensated by the effective enthalpy barrier caused by the temperature dependence of the correlation factor. The diffusivity of any single-vacancy diffusing element in bcc iron is dominated by the diffusivity of a vacancy through the host. All single-vacancy diffusing elements are expected to follow the same trends that the calculated elements do. The activation energy for diffusion are presented in figure 2.10. The nearest-neighbor barrier for the elements strontium, barium, lanthanum, cerium is so low, that it likely does not diffuse through the single-vacancy mechanism. It is more plausible that they form an impurity-vacancy complex which requires another vacancy to diffuse.

All elements except Co, Mn, and Ta show a faster diffusivity than iron self-diffusion, which is confirmed by the experimental data. The other elements show a good agreement with experiments. In bcc iron most substitutional elements diffuse within one order of magnitude faster than bcc iron self-diffusion. Some faster diffusing elements are Au, Pb, Ca. With Pb diffusing 2 orders of magnitude faster than Fe. For the other diffusivities, each impurity element in bcc iron seems to be limited by the self-diffusivity of vacancies in iron.

When considering the position of the element in the periodic table, trends in the rates of diffusivities of impurity element in bcc iron can be observed. With fast diffusing elements at the columns furthest away from Fe and elements in columns close to Fe with diffusivities similar to Fe self-diffusivity. Less important seems to be the row of the periodic system.

2.5. APPENDIX: TABLED DIFFUSIVITIES AND ENERGY BARRIERS

The following tables collect the vacancy binding enthalpies and entropies as calculated according to the procedure laid out in the main article. The data are compared to literature values of other DFT papers. Two different exchange-correlation functionals were used to determine the vacancy formation and binding energies and migration barriers:

PW91 and PBEsol. For each literature source the exchange-correlation functional used and the calculated value is indicated. Unless indicated otherwise, the values reported here were calculated by the authors.

2.5.1. DIFFUSIVITY PARAMETERS

The self-diffusivity and impurity diffusivity of elements in bcc iron, are calculated using the procedures described in this chapter. The activation energies and the prefactor for diffusion as calculated in this thesis are compared to values from literature.

Table 2.2: Calculated activation energies for diffusion in bcc-iron in paramagnetic state (ΔQ_{PM}), ferromagnetic state (ΔQ_{FM}), and the prefactor (D_0). The activation energies and the prefactor (D_0) are calculated with equations 24 and 25, The data are obtained using different exchange-correlation fucntionals as indicated in the table. All energies are in eV and the D_0 is in m^2s^{-1}.

xc type	$Q_{PM}(eV)$	$Q_{FM}(eV)$	D_0 (m^2s^{-1})
Fe			
PW91	2.440	2.830	3.5e-05
PBEsol	2.912	3.328	1.3e-04
PBE	-	2.66[100]	5.9e-7[100]
PBE	2.48[58]	2.87[58]	6.7e-5[58]
PW91	2.46[89]	2.85[89]	-
PW91	-	2.67[57]	-
PBE	2.47[91]	2.85[91]	2.99e-5[91]
PBE	2.26[62]	2.88[62]	1.16e-4[62]
Mg			
PW91	2.210	2.431	2.3e-05
PBEsol	2.634	2.898	2.2e-05
Al			
PW91	2.392	2.631	5.0e-05
PBEsol	2.812	3.093	4.2e-05
Si			
PW91	2.337	2.570	3.6e-05
PBEsol	2.814	3.095	4.1e-05
P			
PW91	2.210	2.431	2.2e-05
PBEsol	2.683	2.952	2.2e-05
S			
PW91	2.157	2.373	4.7e-05
PBEsol	2.624	2.886	4.9e-05
Ca			
PW91	1.966	2.162	1.3e-04
PBEsol	2.402	2.642	1.2e-04
Ti			
PW91	2.415	2.656	7.6e-05
PBEsol	2.860	3.146	7.4e-05

Table 2.2: Calculated activation energies for diffusion in bcc-iron in paramagnetic state (ΔQ_{PM}), ferromagnetic state (ΔQ_{FM}), and the prefactor (D_0). The activation energies and the prefactor (D_0) are calculated with equations 24 and 25, The data are obtained using different exchange-correlation fucntionals as indicated in the table. All energies are in eV and the D_0 is in m^{2}s^{-1}.

xc type	$Q_{PM}(eV)$	$Q_{FM}(eV)$	D_0 (m^{2}s^{-1})
PBE	-	2.26[100]	1.0e-6[100]
V			
PW91	2.497	2.747	8.2e-05
PBEsol	2.948	3.242	8.3e-05
PW91	2.32[89]	2.60[89]	-
Cr			
PW91	2.484	2.732	7.7e-05
PBEsol	2.938	3.232	7.7e-05
PW91	2.32[89]	2.63[89]	-
Mn			
PW91	2.380	2.618	6.4e-05
PBEsol	2.785	3.063	5.7e-05
PW91	2.12[89]	2.44[89]	-
Co			
PW91	2.616	2.877	4.7e-05
PBEsol	3.070	3.377	4.7e-05
Ni			
PW91	2.415	2.656	3.6e-05
PBEsol	2.873	3.161	3.6e-05
Cu			
PW91	2.341	2.576	2.7e-05
PBEsol	2.795	3.075	2.7e-05
Zn			
PW91	2.372	2.609	6.1e-05
PBEsol	2.822	3.105	6.0e-05
Ge			
PW91	2.355	2.590	6.7e-05
PBEsol	2.815	3.096	6.8e-05
Zr			
PW91	2.162	2.378	5.5e-05
PBEsol	2.611	2.872	5.4e-05
PBE	-	2.42[100]	1.2e-6[100]
Nb			
PW91	2.327	2.560	7.4e-05
PBEsol	2.781	3.059	7.4e-05
Mo			
PW91	2.409	2.650	5.9e-05
PBEsol	2.865	3.152	5.4e-05

2

Table 2.2: Calculated activation energies for diffusion in bcc-iron in paramagnetic state (ΔQ_{PM}), ferromagnetic state (ΔQ_{FM}), and the prefactor (D_0). The activation energies and the prefactor (D_0) are calculated with equations 24 and 25, The data are obtained using different exchange-correlation fucntionals as indicated in the table. All energies are in eV and the D_0 is in $m^2 s^{-1}$.

xc type	$Q_{PM}(eV)$	$Q_{FM}(eV)$	D_0 (m^2s^{-1})
PBE	2.43[58]	2.60[58]	6.3e-5[58]
Ag			
PW91	2.128	2.340	2.9e-05
PBEsol	2.587	2.845	2.8e-05
Sn			
PW91	2.141	2.355	3.3e-05
PBEsol	2.597	2.857	3.2e-05
Sb			
PW91	2.204	2.424	5.0e-05
PBEsol	2.668	2.935	5.2e-05
Hf			
PW91	2.201	2.421	6.0e-05
PBEsol	2.649	2.914	5.8e-05
PBE	1.67[58]	1.75[58]	-
Ta			
PW91	2.333	2.566	5.5e-05
PBEsol	2.791	3.070	5.3e-05
PBE	2.22[58]	2.35[58]	-
PBE	2.17[61]	2.30[61]	4.04e-6[61]
PW91	2.15[89]	2.27[89]	-
W			
PW91	2.450	2.695	2.6e-05
PBEsol	2.932	3.226	2.7e-05
PBE	2.58[58]	2.80[58]	1.4e-4[58]
PBE	2.52[61]	2.74[61]	1.38e-4[61]
PW91	2.50[89]	2.72[89]	-
Au			
PW91	2.152	2.367	6.8e-05
PBEsol	2.626	2.888	6.2e-05
PBE	2.11[61]	2.64[61]	2.1e-5[61]
Pb			
PW91	2.027	2.229	2.6e-05
PBEsol	2.487	2.735	2.7e-05
Bi			
PW91	2.044	2.249	4.7e-05
PBEsol	2.512	2.763	4.8e-05

2.5.2. Vacancy binding free energy and jump attempt frequency

The impurity-vacancy binding free energy consists of an enthalpy term and a change in entropy term. Where possible the obtained values were compared to literature.

Table 2.3: Calculated impurity-vacancy binding enthalpies ($\Delta H_{vib,X\square}(\mathbf{R}_1)$), calculated with equation 22, and impurity-vacancy binding entropies ($\Delta\Delta S_{vib,X\square}(\mathbf{R}_1)$), calculated with equation 23 are presented. Also the species dependent nearest neighbour jump frequency ($\tilde{\nu}_X$), calculated with equation 12 is shown. The data are obtained using different exchange-correlation functionals as indicated in the table. The vacancy and impurity binding entropies we calculated only for PW91 and are presented in units of k_B ($\Delta S_\square^b$ (-)).

xc type	$\Delta H_{vib,X\square}(\mathbf{R}_1)$ (eV)	$\Delta\Delta S_{vib,X\square}(\mathbf{R}_1)$ (k_B)	$\tilde{\nu}_X$ (THz)
Mg			
PW91	-0.459	-0.49	4.73
PBEsol	-0.5151	-	-
Al			
PW91	-0.317	-0.38	4.98
PBEsol	-0.348	-	-
Si			
PW91	-0.302	-0.22	3.58
PBEsol	-0.3015	-	-
PW91	-0.23[57]	-	-
P			
PW91	-0.377	0.12	1.86
PBEsol	-0.3697	-	-
PW91	-0.31[57]	-	-
S			
PW91	-0.544	-0.15	0.44
PBEsol	-0.5397	-	-
Ca			
PW91	-1.239	1.55	1.07
PBEsol	-1.2843	-	-
Ti			
PW91	-0.244	0.15	10.30
PBEsol	-0.2576	-	-
PBE	0.26[100]	-	-
V			
PW91	-0.065	0.41	11.11
PBEsol	-0.0681	-	-
PW91	-0.06[89]	-	-
PW91	-0.03[57]	-	-
Cr			
PW91	-0.053	0.41	10.14
PBEsol	-0.0531	-	-
PW91	-0.06[89]	-	-
PW91	-0.03[57]	-	-

Table 2.3: Calculated impurity-vacancy binding enthalpies ($\Delta H_{vib,X\square}(\boldsymbol{R}_1)$), calculated with equation 22, and impurity-vacancy binding entropies ($\Delta\Delta S_{vib,X\square}(\boldsymbol{R}_1)$), calculated with equation 23 are presented. Also the species dependent nearest neighbour jump frequency ($\tilde{\nu}_X$), calculated with equation 12 is shown. The data are obtained using different exchange-correlation functionals as indicated in the table. The vacancy and impurity binding entropies we calculated only for PW91 and are presented in units of k_B ($\Delta S_\square^b$ (-)).

xc type	$\Delta H_{vib,X\square}(\boldsymbol{R}_1)$ (eV)	$\Delta\Delta S_{vib,X\square}(\boldsymbol{R}_1)$ (k_B)	$\tilde{\nu}_X$ (THz)
Mn			
PW91	−0.140	0.12	5.56
PBEsol	-0.1966	-	-
PW91	−0.20[89]	-	-
PW91	−0.09[57]	-	-
Co			
PW91	0.018	0.50	8.85
PBEsol	0.0145	-	-
PW91	0.06[57]	-	-
Ni			
PW91	-0.094	0.23	10.43
PBEsol	-0.1016	-	-
PW91	−0.03[57]	-	-
Cu			
PW91	-0.248	-0.24	2.97
PBEsol	-0.2505	-	-
PW91	−0.17[57]	-	-
Zn			
PW91	-0.339	-0.23	3.05
PBEsol	-0.347	-	-
Ge			
(PW91	-0.464	-0.39	2.51
PBEsol	-0.4633	-	-
Zr			
PW91	-0.724	0.50	3.38
PBEsol	-0.7415	-	-
PBE	−0.78[100]	-	-
Nb			
PW91	-0.362	0.38	6.77
PBEsol	-0.3593	-	-
Mo			
PW91	-0.182	0.38	8.18
PBEsol	-0.1684	-	-
PBE	−0.17[58]	-	-
PW91	−0.08[57]	-	-
Ag			
PW91	-0.517	0.05	2.51
PBEsol	-0.512	-	-

Table 2.3: Calculated impurity-vacancy binding enthalpies ($\Delta H_{vib,X\square}(\mathbf{R}_1)$), calculated with equation 22, and impurity-vacancy binding entropies ($\Delta\Delta S_{vib,X\square}(\mathbf{R}_1)$), calculated with equation 23 are presented. Also the species dependent nearest neighbour jump frequency ($\tilde{\nu}_X$), calculated with equation 12 is shown. The data are obtained using different exchange-correlation functionals as indicated in the table. The vacancy and impurity binding entropies we calculated only for PW91 and are presented in units of k_B ($\Delta S_{\square}^b$ (-)).

xc type	$\Delta H_{vib,X\square}(\mathbf{R}_1)$ (eV)	$\Delta\Delta S_{vib,X\square}(\mathbf{R}_1)$ (k_B)	$\tilde{\nu}_X$ (THz)
Sn			
PW91	-0.720	-0.01	2.54
PBEsol	-0.7219	-	-
Sb			
PW91	-0.745	0.19	4.71
PBEsol	-0.7406	-	-
Hf			
PW91	-0.598	0.51	3.36
PBEsol	-0.6026	-	-
PBE	$-0.65^{[58]}$	-	-
Ta			
PW91	-0.317	0.30	6.03
PBEsol	-0.3053	-	-
PBE	$-0.32^{[58]}$	-	-
PBE	$-0.33^{[61]}$	-	-
PW91	$-0.33^{[89]}$	-	-
W			
PW91	-0.155	0.23	7.64
PBEsol	-0.1348	-	-
PBE	$-0.14^{[58]}$	-	-
PBE	$-0.17^{[61]}$	-	-
PW91	$-0.20^{[89]}$	-	-
PW91	$-0.06^{[57]}$	-	-
Au			
PW91	-0.469	1.26	3.43
PBEsol	-0.4582	-	-
PBE	$-0.32^{[61]}$	-	-
PW91	$-0.33^{[57]}$	-	-
Pb			
PW91	-0.960	-0.09	2.18
PBEsol	-0.9541	-	-
Bi			
PW91	-1.019	0.46	2.91
PBEsol	-1.012	-	-

2.5.3. Migration barrier energies

The barrier for vacancy jumps as function of the distance from from the impurity element. The jump barrier were compared to literature values.

Table 2.4: Calculated migration barriers in bcc-iron ($\Delta H_{mig,i}$), calculated with equation 15, comparison of various xc formulations. All barrier energies are in eV including the effective correlation enthalpy barrier (ΔH_c), which is calculated with equation 20.

xc type	$\Delta H_{mig,nn}$	$\Delta H_{mig,12}$	$\Delta H_{mig,21}$	$\Delta H_{mig,13}$	$\Delta H_{mig,31}$	$\Delta H_{mig,15}$	$\Delta H_{mig,51}$	ΔH_c
Fe								
PW91	0.702	0.702	0.702	0.702	0.702	0.702	0.702	0
PBEsol	0.703	0.703	0.703	0.703	0.703	0.703	0.703	0
PBE	0.64[58]	-	-	-	-	-	-	-
PW91	0.69[89]	-	-	-	-	-	-	-
PW91	0.65[57]	-	-	-	-	-	-	-
PBE	0.65[105]	-	-	-	-	-	-	-
USPP	0.62[94]	-	-	-	-	-	-	-
Mg								
PW91	0.295	1.156	0.615	0.738	0.333	0.689	0.346	0.468
PBEsol	0.282	1.214	0.646	0.767	0.311	0.705	0.311	0.506
Al								
PW91	0.467	0.921	0.574	0.774	0.479	0.753	0.498	0.362
PBEsol	0.464	0.956	0.581	0.773	0.444	0.760	0.478	0.360
Si								
PW91	0.487	0.749	0.556	0.893	0.583	0.824	0.531	0.281
PBEsol	0.492	0.772	0.564	0.890	0.574	0.826	0.530	0.301
PW91	0.44[57]	-	-	-	-	-	-	-
USPP	0.42[94]	-	-	-	-	-	-	-
P								
PW91	0.393	0.700	0.582	0.988	0.580	0.863	0.461	0.315
PBEsol	0.394	0.713	0.580	0.982	0.573	0.860	0.461	0.328
PW91	0.34[57]	-	-	-	-	-	-	-
S								
PW91	0.151	0.784	0.614	1.026	0.459	0.849	0.308	0.644
PBEsol	0.148	0.794	0.613	1.009	0.438	0.830	0.293	0.659
Ca								
PW91	0.020	1.987	0.934	1.268	0.138	1.072	0.021	1.252
PBEsol	0.005	2.000	1.018	1.296	0.119	1.099	0.010	1.295
Ti								
PW91	0.377	1.103	0.677	0.729	0.495	0.715	0.527	0.395
PBEsol	0.365	1.120	0.686	0.735	0.487	0.720	0.521	0.413
PBE	0.42[100]	1.14[100]	0.70[100]	0.75[100]	0.52[100]	0.75[100]	0.58[100]	-
PBE	0.35[105]	-	-	-	-	-	-	-

Table 2.4: Calculated migration barriers in bcc-iron ($\Delta H_{mig,i}$), calculated with equation 15, comparison of various xc formulations. All barrier energies are in eV including the effective correlation enthalpy barrier (ΔH_c), which is calculated with equation 20.

xc type	$\Delta H_{mig,nn}$	$\Delta H_{mig,12}$	$\Delta H_{mig,21}$	$\Delta H_{mig,13}$	$\Delta H_{mig,31}$	$\Delta H_{mig,15}$	$\Delta H_{mig,51}$	ΔH_c
V								
PW91	0.528	0.833	0.677	0.672	0.606	0.691	0.661	0.160
PBEsol	0.522	0.839	0.678	0.671	0.602	0.691	0.660	0.166
PW91	0.50[89]	-	-	-	-	-	-	-
PW91	0.57[57]	-	-	-	-	-	-	-
Cr								
PW91	0.536	0.693	0.658	0.690	0.645	0.665	0.645	0.128
PBEsol	0.540	0.698	0.661	0.691	0.644	0.666	0.646	0.126
PW91	0.53[89]	-	-	-	-	-	-	-
PW91	0.58[57]	-	-	-	-	-	-	-
PBE	0.58[55]	0.69[55]	0.65[55]	0.67[55]	0.63[55]	0.64[55]	0.62[55]	-
PBE	0.52[105]	-	-	-	-	-	-	-
Mn								
PW91	0.406	0.635	0.598	0.684	0.576	0.655	0.564	0.241
PBEsol	0.418	0.643	0.602	0.688	0.571	0.940	0.845	0.233
PW91	0.48[89]	-	-	-	-	-	-	-
PW91	1.02[57]	-	-	-	-	-	-	-
USPP	1.03[94]	-	-	-	-	-	-	-
Co								
PW91	0.737	0.619	0.738	0.713	0.738	0.677	0.712	-0.009
PBEsol	0.744	0.622	0.741	0.717	0.741	0.681	0.714	-0.009
PW91	0.72[57]	-	-	-	-	-	-	-
Ni								
PW91	0.624	0.592	0.690	0.715	0.656	0.653	0.611	-0.002
PBEsol	0.641	0.595	0.693	0.720	0.654	0.648	0.598	-0.006
PW91	0.70[57]	-	-	-	-	-	-	-
PBE	0.68[55]	0.55[55]	0.69[55]	0.70[55]	0.67[55]	0.62[55]	0.59[55]	-
USPP	0.68[94]	-	-	-	-	-	-	-
Cu								
PW91	0.507	0.738	0.646	0.734	0.510	0.668	0.501	0.230
PBEsol	0.540	0.698	0.661	0.691	0.644	0.666	0.646	0.227
PW91	0.65[57]	-	-	-	-	-	-	-
USPP	0.54[94]	-	-	-	-	-	-	-
Zn								
PW91	0.421	0.887	0.632	0.775	0.461	0.730	0.469	0.409
PBEsol	0.427	0.901	0.643	0.781	0.456	0.738	0.465	0.410

2

2

Table 2.4: Calculated migration barriers in bcc-iron ($\Delta H_{mig,i}$), calculated with equation 15, comparison of various xc formulations. All barrier energies are in eV including the effective correlation enthalpy barrier (ΔH_c), which is calculated with equation 20.

xc type	$\Delta H_{mig,nn}$	$\Delta H_{mig,12}$	$\Delta H_{mig,21}$	$\Delta H_{mig,13}$	$\Delta H_{mig,31}$	$\Delta H_{mig,15}$	$\Delta H_{mig,51}$	ΔH_c
Ge								
PW91	0.385	0.910	0.589	0.916	0.465	0.842	0.415	0.545
PBEsol	0.379	0.920	0.600	0.918	0.460	0.845	0.412	0.559
Zr								
PW91	0.110	1.614	0.799	0.956	0.293	0.822	0.214	0.863
PBEsol	0.108	1.623	0.819	0.972	0.290	0.841	0.213	0.880
PBE	0.16[100]	1.62[100]	0.81[100]	0.96[100]	0.32[100]	0.86[100]	0.23[100]	-
Nb								
PW91	0.344	1.248	0.731	0.758	0.430	0.726	0.440	0.450
PBEsol	0.344	1.242	0.734	0.757	0.431	0.729	0.445	0.449
Mo								
PW91	0.550	0.979	0.686	0.685	0.529	0.705	0.574	0.156
PBEsol	0.563	0.968	0.685	0.680	0.535	0.703	0.582	0.135
PBE	0.54[58]	-	-	-	-	-	-	-
PW91	0.57[57]	-	-	-	-	-	-	-
Ag								
PW91	0.448	1.017	0.698	0.721	0.312	0.681	0.328	0.296
PBEsol	0.477	0.997	0.707	0.726	0.316	0.692	0.339	0.273
Sn								
PW91	0.411	1.302	0.656	0.931	0.271	0.855	0.239	0.537
PBEsol	0.417	1.299	0.667	0.937	0.266	0.864	0.232	0.537
Sb								
(PW91	0.495	1.284	0.657	1.014	0.309	0.921	0.243	0.546
PBEsol	0.501	1.276	0.673	1.021	0.310	0.931	0.242	0.549
Hf								
PW91	0.234	1.510	0.743	0.870	0.324	0.783	0.289	0.656
PBEsol	0.233	1.505	0.760	0.872	0.318	0.794	0.293	0.658
PBE	0.18[58]	-	-	-	-	-	-	-
Ta								
PW91	0.484	1.213	0.703	0.730	0.444	0.732	0.471	0.273
PBEsol	0.487	1.197	0.712	0.726	0.448	0.733	0.469	0.264
PBE	0.44[58]	-	-	-	-	-	-	-
PW91	0.44[89]	-	-	-	-	-	-	-
W								
PW91	0.723	0.973	0.682	0.672	0.538	0.720	0.611	-0.001
PBEsol	0.740	0.955	0.680	0.666	0.548	0.718	0.629	-0.006
PBE	0.71[58]	-	-	-	-	-	-	-
PW91	0.71[89]	-	-	-	-	-	-	-
PW91	0.79[57]	-	-	-	-	-	-	-

Table 2.4: Calculated migration barriers in bcc-iron ($\Delta H_{mig,i}$), calculated with equation 15, comparison of various xc formulations. All barrier energies are in eV including the effective correlation enthalpy barrier (ΔH_c), which is calculated with equation 20.

xc type	$\Delta H_{mig,nn}$	$\Delta H_{mig,12}$	$\Delta H_{mig,21}$	$\Delta H_{mig,13}$	$\Delta H_{mig,31}$	$\Delta H_{mig,15}$	$\Delta H_{mig,51}$	ΔH_c
Au								
PW91	0.580	0.942	0.715	0.714	0.350	0.686	0.351	0.146
PBEsol	0.624	0.911	0.715	0.729	0.369	0.695	0.357	0.117
PW91	0.76[57]	-	-	-	-	-	-	-
Pb								
PW91	0.247	1.489	0.725	1.051	0.189	0.923	0.109	0.814
PBEsol	0.253	1.469	0.735	1.054	0.188	0.938	0.110	0.811
Bi								
PW91	0.303	1.529	0.729	1.128	0.197	0.991	0.100	0.836
PBEsol	0.308	1.507	0.745	1.137	0.201	1.006	0.101	0.841

2

2.5.4. Impurity element elastic interaction energies

The energies associated to straining the matrix beyond its equilibrium and the dipole energy associated to the effect of defects on their mirror images contribute to the total free energy of supercells. This effect has been taken into account and the relevant values are reported here.

Table 2.5: The elastic interaction energies of a defect (either single impurity or impurity-vacancy complex) with its own periodic image in a 4×4×4 supercell as computed with the Aneto computer program of Varvenne et al. [66]. Note that half this energy is assigned to the total energy of the defect itself. The energies are in eV per supercell. In the first column the element is listed, the rest is the energy for nearest neighbors of vacancy and impurity.

-	Fe127-X	1st	2nd	3rd	4th	5th
Ag	1.29e-09	2.74e-03	2.48e-05	1.91e-04	4.04e-05	8.05e-04
Al	2.58e-11	9.84e-04	1.69e-04	8.81e-05	6.45e-05	1.68e-04
Au	5.58e-11	2.00e-03	6.97e-05	1.53e-04	1.19e-05	8.93e-04
Bi	2.29e-09	4.97e-03	3.23e-03	5.35e-04	2.57e-05	8.78e-04
Ca	9.66e-10	1.37e-02	5.14e-02	8.73e-04	1.77e-04	1.10e-03
Co	2.29e-11	1.04e-06	6.71e-06	7.27e-06	1.14e-05	5.80e-06
Cr	1.12e-09	1.57e-04	1.73e-04	4.69e-06	6.45e-05	1.45e-05
Cu	5.44e-10	4.61e-04	1.82e-05	3.44e-05	1.00e-04	8.62e-05
Fe	0	2.58e-09	-	-	-	-
Ge	7.28e-08	4.48e-04	1.80e-08	7.75e-05	1.04e-04	5.62e-05
Hf	7.46e-09	5.29e-03	4.62e-03	1.72e-04	5.28e-05	3.86e-04
Mg	3.11e-10	3.53e-03	2.41e-04	1.66e-04	4.90e-05	3.88e-04
Mn	1.73e-10	4.83e-04	5.10e-04	2.08e-06	1.21e-04	4.65e-05
Mo	1.32e-08	9.06e-04	1.86e-06	1.42e-05	1.80e-05	1.27e-04
Nb	3.28e-08	2.31e-03	8.57e-04	3.30e-05	2.98e-05	2.21e-04
Ni	5.58e-10	1.09e-04	1.32e-04	4.07e-06	6.03e-05	4.84e-05
P	3.43e-09	2.24e-06	6.96e-05	1.77e-04	1.63e-04	6.72e-05
Pb	1.08e-11	4.96e-03	1.44e-03	4.99e-04	3.81e-05	9.95e-04
S	2.70e-10	2.07e-05	9.05e-04	3.71e-04	1.65e-04	2.81e-04
Sb	1.04e-08	2.41e-03	7.52e-04	3.38e-04	2.28e-05	3.62e-04
Si	1.06e-08	1.04e-04	1.15e-04	9.99e-05	1.15e-04	4.30e-06
Sn	2.98e-07	3.19e-03	2.27e-04	3.11e-04	3.12e-05	6.05e-04
Ta	3.33e-09	2.10e-03	3.43e-04	4.59e-05	2.94e-05	2.61e-04
Ti	1.16e-09	1.34e-03	8.62e-05	2.32e-05	1.96e-05	6.41e-05
V	7.40e-10	2.58e-04	1.19e-05	7.04e-07	3.44e-05	2.41e-05
W	1.09e-08	8.24e-04	8.80e-06	1.76e-05	1.85e-05	1.21e-04
Zn	6.92e-10	6.91e-04	2.56e-06	4.64e-05	1.14e-04	1.63e-04
Zr	8.86e-09	7.08e-03	6.99e-03	1.81e-04	6.70e-05	4.27e-04

2.5.5. TRANSITION STATE ELASTIC INTERACTION ENERGIES

The energies associated to straining the matrix beyond its equilibrium and the dipole energy associated to the effect of defects on their mirror images contribute to the total free energy of supercells. This effect has been taken into account and the relevant values are reported here.

Table 2.6: The elastic interaction energies of a defect in transition state (A jumping vacancy some distance away from the impurity) with its own periodic image in a 4×4×4 supercell as computed with the Aneto computer program of Varvenne et al. [66]. Note that half this energy is assigned to the total energy of the defect itself. Transition states are indicated by the initial and final states as indicated by the neighbor shell distance between vacancy and solute atom. Units are eV.

elements	$1 \rightarrow 1$	$1 \rightarrow 2$	$1 \rightarrow 3$	$1 \rightarrow 5$
Ag	1.22e-02	4.11e-03	2.10e-03	7.57e-03
Al	5.49e-03	2.49e-03	1.69e-03	5.27e-03
Au	1.12e-02	3.93e-03	3.10e-03	6.38e-03
Bi	1.20e-02	4.96e-03	2.93e-03	7.22e-03
Ca	1.89e-02	6.01e-03	3.22e-03	4.59e-03
Co	1.05e-03	1.67e-03	1.80e-03	1.78e-03
Cr	1.23e-03	1.67e-03	1.15e-03	2.81e-03
Cu	3.44e-03	2.10e-03	1.64e-03	3.77e-03
Fe	1.83e-03	-	-	-
Ge	1.88e-03	2.05e-03	1.89e-03	3.60e-03
Hf	1.45e-02	5.50e-03	1.66e-03	7.79e-03
Mg	1.20e-02	3.63e-03	1.66e-03	8.69e-03
Mn	2.72e-03	1.82e-03	1.25e-03	2.87e-03
Mo	3.98e-03	2.92e-03	1.20e-03	5.38e-03
Nb	7.80e-03	4.16e-03	1.24e-03	7.53e-03
Ni	2.01e-03	1.73e-03	1.79e-03	2.51e-03
P	9.50e-05	2.95e-03	3.86e-03	1.32e-03
Pb	1.29e-02	4.87e-03	2.80e-03	7.35e-03
S	6.11e-04	5.34e-03	5.17e-03	6.33e-04
Sb	7.49e-03	4.02e-03	2.49e-03	6.34e-03
Si	9.44e-04	1.75e-03	2.12e-03	2.75e-03
Sn	1.05e-02	4.25e-03	2.43e-03	7.43e-03
Ta	8.36e-03	4.24e-03	1.28e-03	6.99e-03
Ti	6.07e-03	3.36e-03	1.24e-03	5.60e-03
V	2.08e-03	2.14e-03	1.01e-03	3.50e-03
W	4.32e-03	3.21e-03	1.26e-03	4.58e-03
Zn	4.30e-03	2.26e-03	1.55e-03	4.53e-03
Zr	1.48e-02	5.14e-03	1.75e-03	7.69e-03

REFERENCES

[1] C. D. Versteylen, N. H. van Dijk, and M. H. F. Sluiter, *First-principles analysis of solute diffusion in dilute bcc Fe-X alloys,* Phys. Rev. B **96**, 094105 (2017).

[2] G. Neumann and C. Tuijn, *Self-Diffusion and Impurity Diffusion in Group III Metals,* in *314 Self-diffusion and Impurity Diffusion in Pure Metals 1st Ed.* (Elsevier, 2008) pp. 121–148.

[3] R. J. Borg and D. Y. F. Lai, *The diffusion of gold, nickel, and cobalt in alpha iron: A study of the effect of ferromagnetism upon diffusion,* Acta Metall. **11**, 861 (1963).

[4] M. Lübbehusen and H. Mehrer, *Self-diffusion in α-iron: The influence of dislocations and the effect of the magnetic phase transition,* Acta Metall. Mater. **38**, 283 (1990).

[5] Y. Iijima and K. Hirano, *Self-diffusion and isotope effect in α-iron,* Acta Metall. **36**, 2811 (1988).

[6] G. Hettich, H. Mehrer, and K. Maier, *Self-diffusion in ferromagnetic α-iron,* Scr. Metall. **11**, 795 (1977).

[7] D. W. James and G. M. Leak, *Self-diffusion and diffusion of cobalt in alpha and delta-iron,* Philos. Mag. **14**, 701 (1966).

[8] F. S. Buffington, K. Hirano, and M. Cohen, *Self diffusion in iron,* Acta Metall. **9**, 434 (1961).

[9] D. Bergner and Y. Khaddour, *Impurity and Chemical Diffusion of Al in BCC and Fcc Iron,* Defect Diffus. Forum **95-98**, 709 (1993).

[10] J. Hirvonen and J. Räisänen, *Diffusion of aluminum in ion-implanted alpha iron,* J. Appl. Phys. **53**, 3314 (1982).

[11] D. Bergner, Y. Khaddour, and S. Lörx, *Diffusion of Si in bcc- and fcc-Fe,* Defect Diffus. Forum **66-69**, 1407 (1990).

[12] T. Matsuyama, H. Hosokawa, and H. Suto, *Tracer diffusion of P in Iron and iron alloys,* Trans. Japan Inst. Met. **8**, 589 (1983).

[13] T. Heyward and J.I. Goldstein, *Ternary diffusion in the a and phases of the Fe-Ni-P system,* Met. Trans. **4**, 2335 (1973).

[14] A. Bramley, F. W. Haywood, A. T. Cooper, and J. T. Watts, *the Diffusion of Non-Metallic Elements in Iron and Steel,* Trans. Faraday Soc. **31**, 707 (1934).

[15] G. Siebel, *Diffusion du phosphore dans le fer,* C. R. Acad. Sci. **256**, 4661 (1963).

[16] P. L. Gruzin and V. V. Mural, *no title,* Fiz. Met. Met. **16**, 551 (1963).

[17] A. C. Yen, W. R. Graham, and G. R. Belton, *The segregation of phosphorus to the free surface of a ferritic iron alloy at 723 to 823 K,* Metall. Trans. A **9**, 31 (1978).

[18] W. Arabczyk, M. Militzer, H.-J. Müssig, and J. Wieting, *Activation energy of supher diffusion in ferromagnetic alpha-iron determined by surface segregation studies,* Scr. Metall. **20**, 1549 (1986).

[19] P. Klugkist and C. Herzig, *Tracer diffusion of titanium in α-iron,* Phys. Status Solidi **148**, 413 (1995).

[20] J. Geise and C. Herzig, *Impurity diffusion of vanadium and self-diffusion in iron,* Z. Met. **78**, 291 (1987).

[21] K. Obrtlík and J. Kučera, *Diffusion of vanadium in the Fe-V system,* Phys. Status Solidi **53**, 589 (1979).

[22] C.-G. Lee, Y. Iijima, T. Hiratani, and K.-i. Hirano, *Diffusion of Chromium in alpha iron,* Mater. Trans. JIM **31**, 255 (1990).

[23] A.-M. A. Huntz, M. Aucouturier, and P. Lacombe, *Mesure des coefficients de diffusion en volume et intergranulaire du chrome Radioactif dans le fer alpha,* C. R. Acad. Sci. Paris Ser. C **265**, 554 (1967).

[24] P. J. Alberry and C. W. Haworth, *Alberry (1974) # Interdiffusion of Cr Mo and W in Iron.pdf,* Met. Sci. J. **8**, 407 (1974).

[25] V. Irmer and M. Feller-Kniepmeier, *Diffusion of manganese in α-iron single crystals of different purity,* J. Phys. Chem. Solids **33**, 2141 (1972).

[26] Y. Iijima, K. Kimura, C.-G. Lee, and K. Hirano, *Impurity Diffusion and Isotope Effect of Cobalt in α-Iron,* Mater. Trans. JIM **34**, 20 (1993).

[27] B. Kosaburo, *Diffusion of Co60 into By Kosaburo,* Trans. Japan Inst. Met. **212**, 91 (1963).

[28] K. Hirano, M. Cohen, and B. Averbach, *Diffusion of nickel into iron,* Acta Metall. **9**, 440 (1961).

[29] G. Speich, J. Gula, and R.M. Fisher, *The Electron Microprobe,* in *The Electron Microprobe*, edited by D. W. T.D. McKinley, K.F. Heinrich (Wiley, New York, 1966) p. 525.

[30] S. Rothman, N. Peterson, C. Walter, and L. Nowicki, *Diffusivity of Copper in Iron,* J. Appl. Phys. **39**, 5041 (1968).

[31] M. S. Anand and R. P. Agarwala, *Diffusion of copper in iron,* J. Appl. Phys. **37**, 4248 (1966).

[32] G. Salje and M. Feller-Kniepmeier, *The diffusion and solubility of copper in iron,* J. Appl. Phys. **48**, 1833 (1977).

2

[33] I. Richter, *Diffusion of Zn in alpha-Fe Single Crystals,* Phys. Status Solidi **68**, 289 (1981).

[34] N. Oono, H. Nitta, and Y. Iijima, *Diffusion of niobium in .ALPHA.-iron,* Mater. Trans. **44**, 2078 (2003).

[35] H. Nitta, T. Yamamoto, R. Kanno, K. Takasawa, T. Iida, Y. Yamazaki, S. Ogu, and Y. Iijima, *Diffusion of molybdenum in α-iron,* Acta Mater. **50**, 4117 (2002).

[36] K. Nohara and K.-i. Hirano, *self-diffusion in the Fe-Mo system Nohara,* J. Jpn. Inst. Met. **40**, 1053 (1976).

[37] A. Bondy and V. Levy, *Etude de la diffusion de l'argent dans le fer alpha.* C. R. Acad. Sci. Paris Ser. C **272**, 19 (1971).

[38] D. N. Torres, R. A. Perez, and F. Dyment, *Diffusion of tin in α-iron,* Acta Mater. **48**, 2925 (2000).

[39] D. Treheux, D. Marchive, J. Delagrange, and P. Guiraldenq, *Determination des coefficients d'heterodiffusion a dilution infinie dans le fer α,* C. R. Acad. Sci. Ser. C **274**, 1260 (1972).

[40] R. A. Pérez, D. N. Torres, and F. Dyment, *Sb diffusion in α-Fe,* Appl. Phys. A Mater. Sci. Process. **81**, 787 (2005).

[41] G. A. Bruggeman and J. A. Roberts, *The diffusion of antimony in alpha iron,* Metall. Trans. A **6**, 755 (1975).

[42] A. Schröder and M. Feller-Kniepmeier, *The Ferromagnetic Diffusion Anomaly of the Diffusion System Iron-Antimony,* Phys. Stat. Sol. **107**, 107 (1988).

[43] S. Myers, *Nontraditional Methods in Diffusion*, edited by G. E. Murch, H. K. Birnbaum, and J. R. Cost (Metallurgical Society of AIME, New York, NY, 1984) p. 137.

[44] Q. A. Shaikh, *Interdiffusion measurement of niobium and tantalum in iron base alloys,* Mater. Sci. Technol. **6**, 1177 (1990).

[45] S. Takemoto, H. Nitta, Y. Iijima, and Y. Yamazaki, *Diffusion of tungsten in α-iron,* Philos. Mag. **87**, 1619 (2007).

[46] R. A. Pérez and D. N. Torres, *W diffusion in paramagnetic and ferromagnetic α-Fe,* Appl. Phys. A Mater. Sci. Process. **104**, 329 (2011).

[47] B. Medasani, M. Haranczyk, A. Canning, and M. Asta, *Vacancy formation energies in metals: A comparison of MetaGGA with LDA and GGA exchange-correlation functionals,* Comput. Mater. Sci. **101**, 96 (2015).

[48] T. Hickel, B. Grabowski, F. Körmann, and J. Neugebauer, *Advancing density functional theory to finite temperatures: methods and applications in steel design,* J. Phys. Condens. Matter **24**, 053202 (2012).

[49] J. Janssen, N. Gunkelmann, and H. M. Urbassek, *Influence of C concentration on elastic moduli of α-Fe$_{1-x}$C$_x$ alloys,* Philos. Mag. **96**, 1448 (2016).

[50] G. Steinle-Neumann, L. Stixrude, and R. E. Cohen, *First-Principles Elastic Constants for the hcp Transition Metals Fe, Co, and Re at High Pressure,* Phys. Rev. B **60**, 791 (1999), 9904431 [cond-mat] .

[51] D. Simonovic and M. H. F. Sluiter, *Impurity diffusion activation energies in Al from first principles,* Phys. Rev. B **79**, 054304 (2009).

[52] L. Huber, I. Elfimov, J. Rottler, and M. Militzer, *Ab initio calculations of rare-earth diffusion in magnesium,* Phys. Rev. B **85**, 144301 (2012).

[53] B. C. Zhou, S. L. Shang, Y. Wang, and Z. K. Liu, *Data set for diffusion coefficients of alloying elements in dilute Mg alloys from first-principles,* Data Br. **5**, 900 (2015).

[54] M. Krčmar, C. L. Fu, A. Janotti, and R. C. Reed, *Diffusion rates of 3d transition metal solutes in nickel by first-principles calculations,* Acta Mater. **53**, 2369 (2005).

[55] S. Choudhury, L. Barnard, J. D. Tucker, T. R. Allen, B. D. Wirth, M. Asta, and D. Morgan, *Ab-initio based modeling of diffusion in dilute bcc Fe-Ni and Fe-Cr alloys and implications for radiation induced segregation,* J. Nucl. Mater. **411**, 1 (2011).

[56] J. D. Tucker, R. Najafabadi, T. R. Allen, and D. Morgan, *Ab initio-based diffusion theory and tracer diffusion in Ni-Cr and Ni-Fe alloys,* J. Nucl. Mater. **405**, 216 (2010).

[57] C. Domain, *Ab initio modelling of defect properties with substitutional and interstitials elements in steels and Zr alloys,* J. Nucl. Mater. **351**, 1 (2006).

[58] S. Huang, D. L. Worthington, M. Asta, V. Ozolins, G. Ghosh, and P. K. Liaw, *Calculation of impurity diffusivities in α-Fe using first-principles methods,* Acta Mater. **58**, 1982 (2010).

[59] E. Vincent, C. S. Becquart, and C. Domain, *Ab initio calculations of vacancy interactions with solute atoms in bcc Fe,* Nucl. Instrum. Methods Phys. Res. B **228**, 137 (2005).

[60] C. S. Becquart and C. Domain, *Ab initio contribution to the study of complexes formed during dilute FeCu alloys radiation,* Nucl. Instrum. Methods Phys. Res. B **202**, 44 (2003).

[61] H. Ding, S. Huang, G. Ghosh, P. K. Liaw, and M. Asta, *A computational study of impurity diffusivities for 5d transition metal solutes in α-Fe,* Scr. Mater. **67**, 732 (2012).

[62] L. Messina, M. Nastar, N. Sandberg, and P. Olsson, *Systematic electronic-structure investigation of substitutional impurity diffusion and flux coupling in bcc iron,* Phys. Rev. B **93**, 184302 (2016).

[63] Y. Iijima, *Diffusion in high-purity iron: Influence of magnetic transformation on diffusion,* J. Phase Equilibria Diffus. **26**, 466 (2005).

[64] L. Girifalco, *Vacancy concentration and diffusion in order-disorder alloys,* J. Phys. Chem. Solids **25**, 323 (1964).

[65] L. Ruch, D. R. Sain, H. L. Yeh, and L. A. Girifalco, *Analysis of diffusion in ferromagnets,* J. Phys. Chem. Solids **37**, 649 (1976).

[66] C. Varvenne, F. Bruneval, M. C. Marinica, and E. Clouet, *Point defect modeling in materials: Coupling ab initio and elasticity approaches,* Phys. Rev. B **88**, 134102 (2013).

[67] D. C. Wallace, *Thermodynamics of Crystals*, Dover books on physics (Dover Publications, 1998) pp. 180–183.

[68] A. S. Arrott and B. Heinrich, *Application of magnetization measurements in iron to high temperature thermometry,* J. Appl. Phys. **52**, 2113 (1981).

[69] C. Versteylen, N. van Dijk, and M. Sluiter, *to be submitted,* to be Submitted .

[70] G. H. Vineyard, *Frequency factors and isotope effects in solid state rate processes,* J. Phys. Chem. Solids **3**, 121 (1957).

[71] A. D. Le Claire, *Solvent self-diffusion in dilute b . c . c . solid solutions,* Philos. Mag. **21**, 819 (1970).

[72] M. J. Jones and A. D. Le Claire, *Solvent self-diffusion in dilute b.c.c. solid solutions,* Philos. Mag. **26**, 1191 (1972).

[73] J. Neuhaus, W. Petry, and a. Krimmel, *Phonon softening and martensitic transformation in α-Fe,* Phys. B Condens. Matter **234**-**236**, 897 (1997).

[74] A. V. Ruban and V. I. Razumovskiy, *Spin-wave method for the total energy of paramagnetic state,* Phys. Rev. B **85**, 174407 (2012).

[75] H. Ding, V. I. Razumovskiy, and M. Asta, *Self diffusion anomaly in ferromagnetic metals: A density-functional-theory investigation of magnetically ordered and disordered Fe and Co,* Acta Mater. **70**, 130 (2014).

[76] F. Körmann, B. Grabowski, B. Dutta, T. Hickel, L. Mauger, B. Fultz, and J. Neugebauer, *Temperature dependent magnon-phonon coupling in bcc Fe from theory and experiment,* Phys. Rev. Lett. **113**, 165503 (2014).

[77] S. Baroni, S. De Gironcoli, A. Dal Corso, and P. Giannozzi, *Phonons and related crystal properties from density-functional perturbation theory,* Rev. Mod. Phys. **73**, 515 (2001), arXiv:0012092v1 [arXiv:cond-mat] .

[78] G. Kresse and J. Furthmüller, *Efficiency of ab-initio total energy calculations for metals and semiconductors using a plane-wave basis set,* Comput. Mater. Sci. **6**, 15 (1996).

[79] G. Kresse and J. Furthmüller, *Efficient iterative schemes for ab initio total-energy calculations using a plane-wave basis set,* Phys. Rev. B **54**, 11169 (1996).

[80] P. E. Blöchl, *Projector Augmented-Wave Method,* Phys. Rev. B **50**, 17953 (1994).

[81] G. Kresse and D. Joubert, *From ultrasoft pseudopotentials to the projector augmented-wave method,* Phys. Rev. B **59**, 1758 (1999).

[82] G. Henkelman and H. Jonsson, *Improved tangent estimate in the nudged elastic band method for finding minimum energy paths and saddle points,* J. Chem. Phys. **113**, 9978 (2000).

[83] J. P. Perdew and Y. Wang, *Accurate and Simple Analytic Representation of the Electron-Gas Correlation-Energy,* Phys. Rev. B **45**, 13244 (1992).

[84] J. P. Perdew, J. A. Chevary, S. H. Vosko, K. A. Jackson, M. R. Pederson, D. J. Singh, and C. Fiolhais, *Erratum: Atoms, molecules, solids, and surfaces: Applications of the generalized gradient approximation for exchange and correlation,* Phys. Rev. B **46**, 6671 (1992).

[85] J. P. Perdew, A. Ruzsinszky, G. I. Csonka, O. A. Vydrov, G. E. Scuseria, L. A. Constantin, X. Zhou, and K. Burke, *Restoring the Density-Gradient Expansion for Exchange in Solids and Surfaces,* Phys. Rev. Lett. **100**, 136406 (2008).

[86] P. Haas, F. Tran, and P. Blaha, *Calculation of the lattice constant of solids with semilocal functionals,* Phys. Rev. B **79**, 085104 (2009).

[87] R. Nazarov, T. Hickel, and J. Neugebauer, *Vacancy formation energies in fcc metals: Influence of exchange-correlation functionals and correction schemes,* Phys. Rev. B **85**, 144118 (2012).

[88] Y. Jiang, J. R. Smith, and G. R. Odette, *Formation of Y-Ti-O nanoclusters in nanostructured ferritic alloys: A first-principles study,* Phys. Rev. B **79**, 064103 (2009).

[89] C. Zhang, J. Fu, R. Li, P. Zhang, J. Zhao, and C. Dong, *Solute/impurity diffusivities in bcc Fe: A first-principles study,* J. Nucl. Mater. **455**, 354 (2014).

[90] D. Murali, M. Posselt, and M. Schiwarth, *First-principles calculation of defect free energies: General aspects illustrated in the case of bcc Fe,* Phys. Rev. B **92**, 064103 (2015).

[91] X. Gao, H. Ren, C. Li, H. Wang, Y. Ji, and H. Tan, *First-principles calculations of rare earth (Y, la and Ce) diffusivities in bcc Fe,* J. Alloys Compd. **663**, 316 (2016).

2

[92] A. Glensk, B. Grabowski, T. Hickel, and J. Neugebauer, *Breakdown of the arrhenius law in describing vacancy formation energies: The importance of local anharmonicity revealed by Ab initio thermodynamics,* Phys. Rev. X **4**, 011018 (2014).

[93] J. P. Perdew, K. Burke, and M. Ernzerhof, *Generalized Gradient Approximation Made Simple,* Phys. Rev. Lett. **77**, 3865 (1996).

[94] E. Vincent, C. S. Becquart, and C. Domain, *Atomic kinetic Monte Carlo model based on ab initio data: Simulation of microstructural evolution under irradiation of dilute Fe-CuNiMnSi alloys,* Nucl. Instrum. Methods Phys. Res. B **255**, 78 (2007).

[95] G. Lucas and R. Schäublin, *Vibrational contributions to the stability of point defects in bcc iron: A first-principles study,* Nucl. Instrum. Methods Phys. Res. B **267**, 3009 (2009).

[96] L. Messina, M. Nastar, T. Garnier, C. Domain, and P. Olsson, *Exact ab initio transport coefficients in bcc Fe-X (X=Cr, Cu, Mn, Ni, P, Si) dilute alloys,* Phys. Rev. B **90**, 104203 (2014).

[97] L. Messina and M. Nastar, *http://link.aps.org/supplemental/ 10.1103/PhysRevB.93.184302*, Tech. Rep. (1800).

[98] T. Ohnuma, N. Soneda, and M. Iwasawa, *First-principles calculations of vacancy-solute element interactions in body-centered cubic iron,* Acta Mater. **57**, 5947 (2009).

[99] P. Olsson, T. P. C. Klaver, and C. Domain, *Ab initio study of solute transition-metal interactions with point defects in bcc Fe,* Phys. Rev. B **81**, 054102 (2010).

[100] D. Murali, B. K. Panigrahi, M. C. Valsakumar, and C. S. Sundar, *Diffusion of y and Ti/Zr in bcc iron: A first principles study,* J. Nucl. Mater. **419**, 208 (2011).

[101] *A fit of three parameters to just four data points is questionable in any case,* .

[102] G. Boisvert and L. J. Lewis, *Self-diffusion on low-index metallic surfaces: Ag and Au (100) and (111),* Phys. Rev. B **54**, 2880 (1996).

[103] M. C. Marinica, C. Barreteau, D. Spanjaard, and M. C. Desjonquères, *Diffusion rates of Cu adatoms on Cu(111) in the presence of an adisland nucleated at fcc or hcp sites,* Phys. Rev. B - Condens. Matter Mater. Phys. **72**, 115402 (2005).

[104] T. Marumo, S. Fujikawa, and K.-i. Hirano, *Diffusion of zirconium in aluminium,* J. Japan Inst. Light Met. **23**, 17 (1973).

[105] A. Claisse and P. Olsson, *First-principles calculations of (Y, Ti, O) cluster formation in body centred cubic iron-chromium,* Nucl. Instrum. Methods Phys. Res. B **303**, 18 (2013).

3

MAGNETIC ACTIVATION ENERGY FOR DIFFUSION IN BCC IRON

Da ubriaco è difficile acchiappare un gatto nero in una stanza buia;
soprattutto quando non c'è...

Italian proverb

A rather remarkable feature of diffusion behaviour in bcc-iron, is the deviation from the Arrhenius relation around the Curie temperature. The activation barrier for diffusion is lower in the paramagnetic state than in the ferromagnetic state. This change in activation energy occurs gradually, and most strongly in the vicinity of the Curie temperature. Apart from the activation barrier for diffusion, there is a marked shear modulus softening around the Curie temperature. The degree of magnetic ordering and the magnetic contribution to the free energy can be used as a way to fit the temperature dependence of the activation barrier. The Girifalco model relates the change in activation barrier to the degree of magnetic order, and the Jönsson model relates the change in activation barrier to the total magnetic enthalpy. Both models can lead to similar results over the temperature range in which diffusion in bcc iron is conventionally measured, but give different values for the activation barrier in paramagnetic state. A comparison is made between experimental data and modelling results for both models. The fitting of a wide selection of experimental data shows that it is within reason to state that the effect of magnetic order on the activation energy is species independent. The species-independent fitting parameter used to determine the effect of magnetic order on the activation energy is $\alpha = 0.10(1)$.

3.1. INTRODUCTION

The diffusive transport of elements in a crystal is a thermally activated process. In the case of substitutional diffusion, the rate of diffusivity depends on the concentration of vacancies, and the jump rate. If the energy for the formation of a vacancy and the energy barrier are independent of temperature, the diffusivity (D) can be described by an Arrhenius relation,

$$D = D_0 \exp\left(-\frac{Q}{k_B T}\right).$$ (3.1)

Where the prefactor D_0, the activation energy for diffusion Q, and the Boltzmann constant k_B are constants and the diffusivity D is a function of temperature T. In bcc-iron, there is a deviation from this Arrhenius relation. The deviation from the Arrhenius relation takes place for diffusivity at the ferromagnetic-to-paramagnetic transition (T_C). For pure iron (and sufficiently dilute binary iron alloys) the transition temperature T_C is 1043 K.
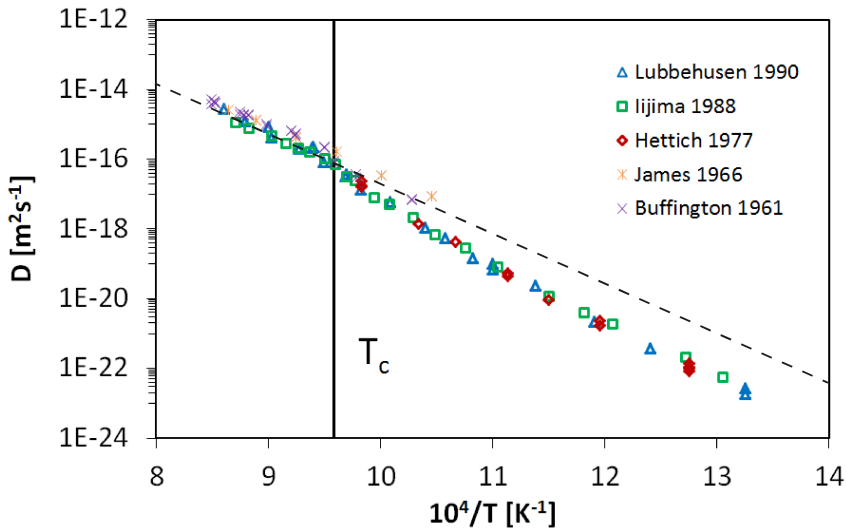
Figure 3.1: Experimental data of iron self-diffusivity as a function of the inverse temperature [1–5]. The Curie temperature is indicated as T_C, and the dashed line is an extrapolation of Arrhenius behaviour of the paramagnetic state above T_C.

This deviation could in principle be attributed to a temperature dependence of D_0 and/or Q. Both the pre-exponential factor and the activation energy may change with the degree of ferromagnetic order. Buffington and coworkers [5] presented D_0 and Q for ferromagnetic and for paramagnetic bcc iron as separate phases. They noted that, for a constant activation barrier, the change in D_0 would have to be 4 orders of magnitude, which seems unlikely. They therefore concluded that there is a different activation barrier for diffusion in the paramagnetic state, compared to the ferromagnetic state.

The narrow temperature range studied in many diffusivity measurements did not

allow for a more detailed description of the diffusivity in paramagnetic and in ferromagnetic states. Hettich and coworkers [3] were the first to measure diffusivities over a wide temperature range of more than 300 K, all below the Curie temperature. The diffusivity was found to deviate from the Arrhenius relation, an observation which is often called the anomalous effect in bcc iron, later observations confirmed this [1, 2].

3.2. MAGNETIC ORDER

The Curie temperature is the transition temperature above which no long-ranged ferromagnetic order exists. The ground state of bcc iron at 0 K is the fully aligned ferromagnetic state. The magnetic alignment is gradually weakened with increasing temperatures, until long-ranged ferromagnetic ordering is lost at T_C. The reduced spontaneous magnetisation $s = M_s(T)/M_s(0)$, has been measured by Bergmann and coworkers [6], and the data have been fitted by Arrott and coworkers [7], see figure 3.2.

$$s = \frac{(1-\tau)^B}{(1 - B\tau + A\tau^{3/2} - C\tau^{7/2})}, \tag{3.2}$$

with $\tau = T/T_C$, $B = 0.368$, $A = 0.110$, and $C = 0.129$. At the Curie temperature
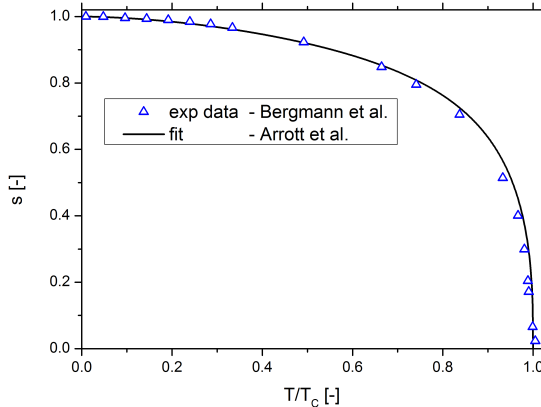
Figure 3.2: Normalised spontaneous magnetisation $s = M_s(T)/M_s(0)$ of bcc iron as function of the normalised temperature (T/T_C).

long-range order is lost, but short-range order in the magnetic alignment persists. The magnetic free energy therefore also develops above the Curie temperature. The magnetic free energy can be approximated through the Inden model for magnetic heat capacity, as done by Hillert and Jarl [8]. They used a Taylor expansion to approximate the magnetic free energy. Alternatively, the magnetic specific heat of bcc iron can be described by a fit to experiments, as done by Chuang and coworkers [9]. They also successfully apply the same method to approximating the magnetic specific heats of nickel and cobalt. The results of the normalized magnetic enthalpy as function of normalized temperature are shown in figure 3.3.
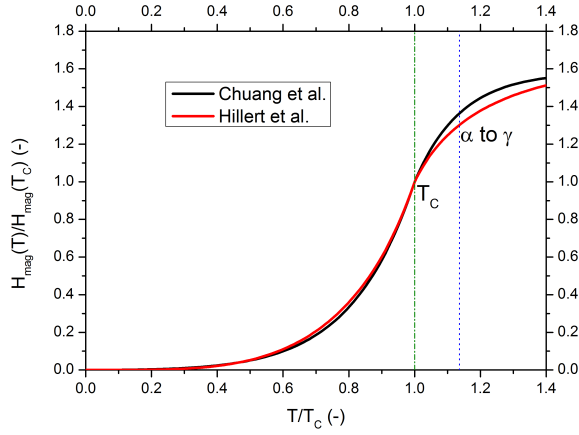
Figure 3.3: The relative magnetic enthalpy $H_{mag}/H_{mag}(T_C)$ as function of T/T_C. Obtained from the magnetic enthalpy equations of Chuang and coworkers [9], and of Hillert and Jarl [8]. The Curie temperature is indicated as T_C, and the transition temperature in pure iron between α-iron (bcc), and γ-iron (fcc).

Note that pure iron transforms from bcc to fcc at 1.14 T/T_C, which means that the extrapolated magnetic free energy in bcc phase for temperatures above 1.14 T_C cannot be observed in pure iron.

The deviation of the diffusivity from Arrhenius relation is only one of the effects associated with magnetic ordering in bcc iron. The phonon spectrum of iron softens at high temperatures for certain modes, as was measured by Vallera [10] and Neuhaus and coworkers[11]. This phonon softening coincides with a reduction in stiffness in certain crystallographic directions. The stiffness tensor describing directional stiffness of a cubic crystal has 3 degrees of freedom only;

$$C_{ijkl} = \begin{bmatrix} C_{11} & C_{12} & C_{12} & 0 & 0 & 0 \\ C_{12} & C_{11} & C_{12} & 0 & 0 & 0 \\ C_{12} & C_{12} & C_{11} & 0 & 0 & 0 \\ 0 & 0 & 0 & C_{44} & 0 & 0 \\ 0 & 0 & 0 & 0 & C_{44} & 0 \\ 0 & 0 & 0 & 0 & 0 & C_{44} \end{bmatrix}. \tag{3.3}$$

The influence of temperature on the stiffness tensor of bcc-iron is significant when the Curie temperature is approached, as was measured by Dever [12], see figure 3.4. The softening of the shear modulus

$$C' = \frac{C_{11} - C_{12}}{2}, \tag{3.4}$$

is an indication that the shear in bcc iron is affected by the spin alignment, especially between the second and first nearest neighbors [12].

To summarize, the loss of magnetic spin alignment in bcc iron causes:
(i) the reduction in free energy associated to magnetism as spins lose order both over long range below T_C and also at short range above T_C. therefore this reduction occurs
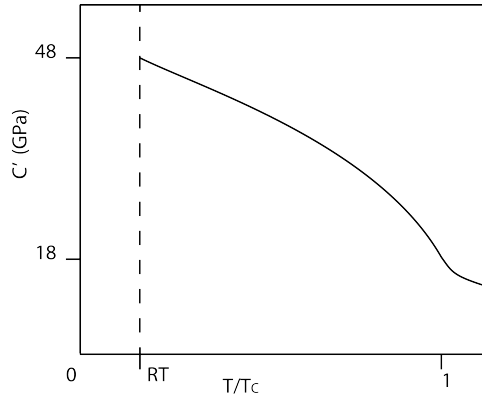
Figure 3.4: Shear modulus C' as function of normalized temperature T/T_C (figure adapted from Dever [12]).

partially above the Curie temperature, figure 3.3.

(ii) phonon softening and a shear modulus softening.

(iii) The effect on the diffusivity is due to a variation in the effective jump barrier Q, which manifests itself as a deviation from linear Arrhenius behaviour.

3.3. MODELS FOR MAGNETIC ENTHALPY OF DIFFUSION

Since the discovery of the deviation of the diffusivity from Arrhenius relation in bcc iron, attempts were made to explain the effect. The deviation from Arrhenius relation was found to be related to the activation energy, which means there is a contribution of the activation energy for diffusion Q that is dependent on the degree of magnetic order. The most important models describing this magnetic contribution to the activation barrier are made by Girifalco and by Jönsson. Both of these models propose a magnetic dependence on the activation barrier for diffusion and describe the magnitude of the magnetic activation barrier as function of magnetic parameters.

The origins of this effect however are still unclear, but there are proposed solutions. Borg [13] analyzed the effect of magnetism on the diffusivity in bcc iron, and related the effective magnetic activation energy to the marked softening of stiffness directions in bcc-iron close to the Curie temperature. Hettich and coworkers [3] applied the logic of Borg, and used the Girifalco model to describe the diffusivity of bcc iron, as function of the magnetic order parameter.

For both the Girifalco and the Jönsson model, the magnetic contribution to the activation energy for diffusion, is a fraction of the magnetic energy of interacting spins in the material. The enthalpy associated to spin alignment can be described with a magnetic Ising Hamiltonian with spin S (up or down) where the exchange interaction between spins J is constant:

$$H = -J \sum_{i,j} S_i S_j. \tag{3.5}$$

The magnetic energy of interacting spins depends on their alignment and the ionic positions. A fraction of the energy difference between paramagnetic and ferromagnet-

icly ordered lattices, is responsible for the reduction in magnetic activation barrier for diffusion.

In the Girifalco model, this effect only exists due to the loss of long-rang magnetic order below the Curie temperature, while in the Jönsson model, all magnetic spin alignment plays a role (both long-range and short-range), which means that part of the deviation is above the Curie temperature. Applying either model gives accurate results when fitting the temperature-dependence of the diffusivity around T_C. However, there is a difference in the obtained activation energies for diffusion between the paramagnetic and ferromagnetic states ΔQ_{PM-FM}. Experimental data for impurity diffusion in bcc iron allows us to discriminate between both models.

3.3.1. GIRIFALCO MODEL

The magnetic contribution to the activation energy was determined by Girifalco [14]. The exchange energy arises from the exchange integral J, and the spontaneous magnetisation, see figure 3.2. The activation energy for diffusion is proposed to be of the following form:

$$Q(T) = Q_{PM}(1 + \alpha s^2). \tag{3.6}$$

The parameter α determines the effective magnetic exchange. The magnetic energy affects the activation barrier, which was determined by fitting experimental data to the models' equations by Ruch and coworkers [15]. Their analysis provided that the magnetic interaction parameter in bcc iron is $\alpha = 0.112$. More recent reports on self-diffusivity resulted in $\alpha = 0.16$ [3] and $\alpha = 0.156(3)$ [2]. The implicit assumption in this model is that short-range magnetic ordering plays no role in the barrier for diffusion. This model has been used to capture the deviation from Arrhenius relation of many diffusing elements [2, 3, 16, 16–27]. Since the parameter α could be dependent on the diffusion element in bcc iron, an attempt was made to estimate the values of α for each impurity element. Iijima and coworkers [28] found that α depends on the species of impurity element diffusion in iron. They proposed a relationship between the change in magnetic moments of the first and second nearest neighbours due to the impurity element and the value of α. This relationship was based on observations of diffusion of the elements: Ti, Cr, Fe, Co, Nb, Mo in bcc iron. This method was later applied by Ding and coworkers [29], in order to predict α in the context of *first-principles* diffusivity calculations. The difference between the activation energy for diffusion in paramagnetic and in ferromagnetic state for the Girifalco model is between 10 and 16% of the paramagnetic activation barrier [2, 3].

3.3.2. JÖNSSON MODEL

The effect of magnetic order on the activation barrier for diffusion was described by Jönsson [30], using the magnetic enthalpy as described by Hillert and Jarl [8] (figure 3.3). Unlike the Girifalco model, in the Jönsson model the activation barrier depends on the energy associated with all magnetic order (short-range and long-range).

This model was applied by Messina and coworkers to model the magnetic contribution to the activation energy for diffusion [31, 32]. The activation energy for diffusion

is considered to depend on temperature as;

$$Q(T) = Q_{FM} - \xi H(T). \tag{3.7}$$

The normalised temperature dependent magnetic enthalpy used to calculate the activation barrier is defined as $H(T) = 1 - H_{mag}(T)/H_{mag}(0)$, where H_{mag} is the magnetic enthalpy, and with ξ as a fitting parameter, similar to α for the Girifalco model. The Jönsson model is applied in Dictra as part of the Thermocalc package [33]. Liu and coworkers [34] applied this model to experimental data and fitted the parameter ξ to different impurity elements in bcc iron. From those results, Messina and coworkers [32] concluded that the parameter is diffusing species independent. The difference between the activation energy for diffusion in paramagnetic and in ferromagnetic state obtained from this model is approximately 22% of the paramagnetic activation barrier [32].

3.3.3. MODEL COMPARISON

The different models describing the anomalous effect of bcc iron diffusion are reviewed by Lübbehusen [1], who reviewed 5 different models, of which some have several fitting parameters. Lübbehusen concluded that each gives a fit which is equivalent in accuracy. Therefore a choice to focus only on the two models with one fit parameter, namely the Girifalco model and the Jönsson model was made. However, it is difficult to obtain an accurate fit because the paramagnetic range of bcc α-iron is very limited (between 1043 and 1185 K). The accuracies of the measured diffusivities are not high enough to obtain an accurate fit over such a small temperature range. The data from bcc δ-iron can be used, which is the phase stable between 1766 K and 1811 K. When data from both bcc iron phases is used the activation energies obtained for iron self-diffusion are close to 2.5 eV [4, 35] (approximately 240 kJ/mol).

Determining the paramagnetic activation barrier in bcc iron by means of computational methods is a challenge. Ruban and Razumovskiy [36] have applied DFT spin-wave, EMTO-CPA, and Monte Carlo methods to simulate the paramagnetic state in bcc iron. They compared vacancy formation energies calculated with these different methods. The spin-wave method was also used to calculate the migration barrier in paramagnetic state, in order to obtain the paramagnetic activation for diffusion in pure iron, which was found to be 2.41 eV [37]. They also applied the same method to determine the difference in activation barriers in ferromagnetic state and in paramagnetic state of fcc Co, and found a negligible difference in the activation energies between the paramagnetic and ferromagnetic states.

The activation barrier for paramagnetic diffusion was also determined by Sandberg and coworkers by means of Monte Carlo methods with a Heisenberg Hamiltonian to obtain the magnetic contribution to the energy [38]. They reported the magnetic enthalpy and activation barrier for paramagnetic diffusion. The magnetic enthalpy was found to deviate from the experimentally observed values and the paramagnetic activation barrier using this approach is 2.26 eV.

The self-diffusion activation barrier for iron can be evaluated in alloys containing small percentages of bcc-stabilizing solute. This has been done in order to determine the self-diffusion activation barrier over a wider range of temperatures. Since the effect of the experimental errors in determining the diffusivity has a smaller effect on the error

Table 3.1: Bcc iron self-diffusion activation barriers determined in alloys which stabilise the bcc phase.

Alloy	Q_{PM} (eV)	ΔT (K)	source
Fe-5.7 at.%Al	2.55	1123-1458	Borg [40]
Fe-5.5 at.%Si	2.59	1013-1373	Million [39]
Fe-4.7 at.%Si	2.41	1173-1733	Borg [40]
Fe-2.0 at.%Ti	2.50	1173-1473	Borg [40]
Fe-1.8 at.% V	2.45	1173-1773	Borg [40]
Fe-5.3 at.% V	2.55	1173-1466	Borg [40]
Fe-2.5 at.%Sb	2.25	1169-1370	Borg [40]

in the experimentally determined activation barrier if the data is obtained over a wider range of temperatures, this allows for more confidence in the value of the activation energy for diffusion. Fe-4.7at.%Si is therefore an excellent model system to analyse the diffusivity of Fe in bcc at higher temperatures [39]. Borg and Lai have collected and analysed a large amount of data on high temperature Fe diffusion [40], with alloys containing Al, Si, Ti, V, and Sb (see table 3.1).

All but one of the activation energies for paramagnetic diffusion lie very close to the commonly more accepted activation energy for iron self-diffusion in paramagnetic state of 2.44 eV [41], 2.47 eV [42], 2.46 eV [43] and 2.48 eV [44]. This supports the Girifalco model, since the difference between paramagnetic and ferromagnetic activation barriers is 0.36 eV[37] as opposed to the value obtained by the Jönsson model of 0.62 eV [32].

3.4. FITTING OF EXPERIMENTAL DATA

Having established that the Girifalco model better agrees with experiments than the Jönsson model, it is now applied to reviewing experimental diffusivity data in bcc iron. In order to determine the species-dependent influence of magnetic order on the diffusion in bcc iron, the diffusion function is used to fit experimental data:

$$D = D_0 \exp\left(-\frac{Q_{PM}(1 + \alpha s^2)}{k_B T}\right), \qquad (3.8)$$

where the function s is obtained from Arrot [7]. The only fittable parameters are; Q_{PM}, D_0, and α. Previously, Iijima and coworkers [28] found a relationship between the magnitude of α and the effect of the nearest neighbour elements on the magnetic moments (ΔM_{1-2}). The amount of experimental datasets in their analysis was limited to 6. If more datasets are used to determine the value of α, one finds a large spread for α, and no clear relation between α and ΔM_{1-2} in figure 3.5. The trend that was observed by Iijima and coworkers [28] does not seem evident if more datasets are included in the analysis. The paramagnetic activation energies and the parameter α of these datasets suggest an inverse relation with activation energy. The activation energies of the impurity elements in bcc iron, used by Iijima and coworkers [28], are all higher than that of iron self-diffusion. This trend does not agree with more recent evaluations for the same elements [29, 41, 53]. The impurity diffusion activation energies seem to generally be smaller for elements in bcc iron, except for cobalt. This suggests that the
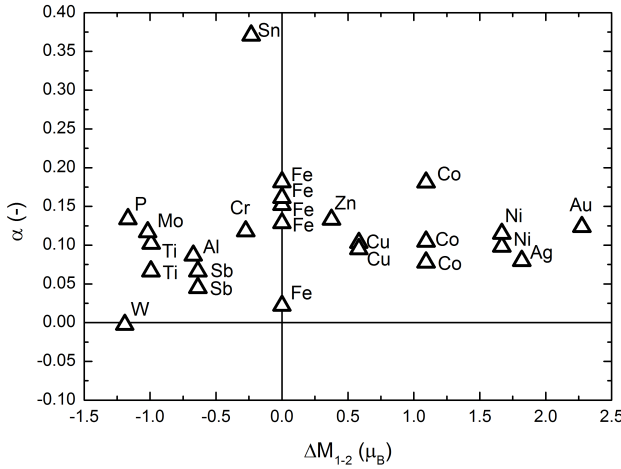
Figure 3.5: Fitted values of α versus the change in magnetic moment of nearest neighbours ΔM_{1-2}. For iron self-diffusion Fe [2–5] and the following solute elements; , Co [4, 16, 45], Ni [45, 46], Mo [20], Nb [18], Cr [23], Sn [24], Ag [47], Au [45], Zn [48], Cu [25, 49], Sb [19, 50] , P [51], and Al [26, 52].
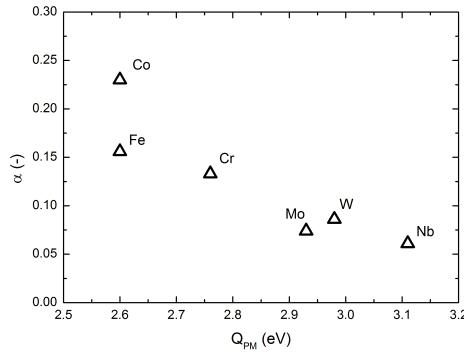

Figure 3.6: Parameter α and activation energy for diffusion Q_{PM} according to the data used in the paper by Iijima and coworkers [28].

relationship found might be the result of imprecise activation energies.

If the paramagnetic activation energy is fit in the paramagnetic temperature range, the value of α can be calculated for each measured diffusivity at different temperatures below T_C. The value of α now depends on the temperature range at which the paramagnetic activation energy Q_{PM} is fit. Pure iron self-diffusion can be analysed in the paramagnetic range range from T_C to the phase transformation temperature $T_{bcc \to fcc}$, or in the range from $T_C + 40$ K to $T_{bcc \to fcc}$. The fit for α is strongly dependent on
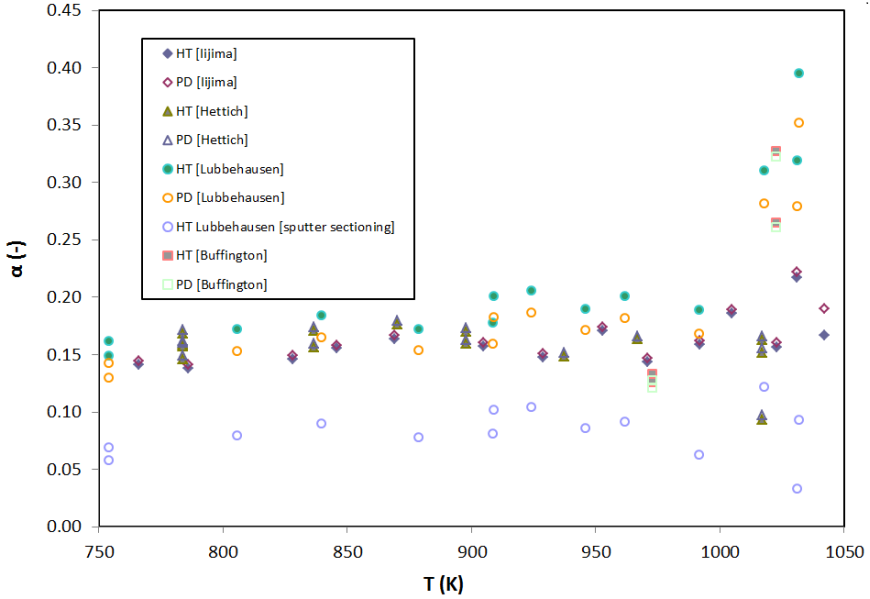
Figure 3.7: Experimental data of Iijima [2], Lübbehusen [1], and Buffington [5] was used to fit Q_{PM} in the temperature range above T_C and 40 K above T_C in order to obtain the value of α for each data point at different temperatures below T_C. For the data of Hettich [3], the Q_{PM} of Iijima and coworkers was used to fit α below T_C.

the temperature range of the fit of Q_{PM}, since the magnitude of the paramagnetic activation energy depends on the temperature range of the fit and the number of data points. This is an illustration of the fragility of this method, and the interdependence of the magnitude of the fitting parameters. Furthermore, it is clear from this figure that close to the Curie temperature, the reliability of the fit of parameter α is compromised significantly.

The maximum amount of available experimental datasets was used to obtain accurate fits for α. The nonlinear least-squares (NLLS) Marquardt-Levenberg algorithm was used fit the experimental data to the diffusion function. For each experimental data set, this results in fitted values with certain error margins. The accuracy of the fit can be approximated by analysing the magnitude of the error. The lowest possible error for the value of α was used and all parameter with an error > 0.025 were discarded.

3.5. Results & Discussion

From the results of the fits in figure 3.8, it can be concluded that there is no reason to assume a relationship between α and ΔM_{1-2}. The average value of α for impurity elements is $0.10(1)$. For iron self-diffusion, fits applied to a combination of all datasets gives $\alpha = 0.17(2)$ and the most reliable from literature $\alpha = 0.16$ [3] and $\alpha = 0.156(3)$ [2], leads us to $\alpha = 0.16(1)$. When these values of α for iron self-diffusion and for impurity diffusion are applied to known diffusion data, the Girifalco model seems to provide a
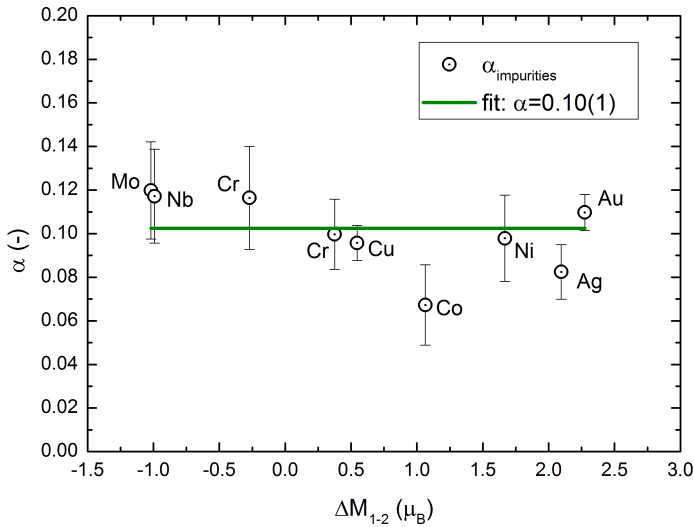
Figure 3.8: Datasets with sufficiently low fitting errors for α plot against the change in magnetisation ΔM_{1-2}. Datasets from: Cr [54], Co [45], Ni [45], Cu [25], Zn [48], Nb [18], Mo [20], Ag [47], Au [45] were used. The line corresponds to the average value of α.

good correction for the deviation from Arrhenius behaviour. In figure 3.9, experimental data of iron self-diffusion is plotted as function of $(1 + \alpha s^2)/(k_B T)$ (with $\alpha = 0.16$). This provides a logarithmic relation indicating that the deviation of the Arrhenius relation has been compensated by this correction.

The same approach is followed for iron self-diffusion (with $\alpha = 0.16$) and for impurity elements (with $\alpha = 0.10$) together in figure 3.10. The value of α was compared to many other impurity properties, such as migration barrier, vacancy binding, atomic size, or atomic mass with no relation found. It should be noted that also for the Hillert-Jarl model as used by Messina and coworkers[32], the fitting parameter ξ was chosen to be constant for all impurities diffusing in bcc iron, based on the Calphad analysis of Liu and coworkers [34]. The $\alpha = 0.10(1)$ approximation can be applied to a large selection of impurity data in order to test the validity of this assumption. The results are shown in figure 3.10 and show satisfactory agreement.

The reason behind the non-Arrhenius diffusion behaviour could be in the softening of a specific shear mode C' in the bcc crystal close to T_C [13, 63]. In other words there is a strong coupling between the spin order and the elastic stiffness properties. Softening of phonon modes and shear modes, has a particularly large effect on the bcc crystal structure. Perhaps a similar effect can be seen in Zr self-diffusion in body centered crystalline structure [13]. The non closely packed crystal structure could be required to show the non-Arrhenius behaviour. Where the phonon modes soften as well and the diffusivity deviates far from Arrhenius. This behaviour is assumed to be related to the

3
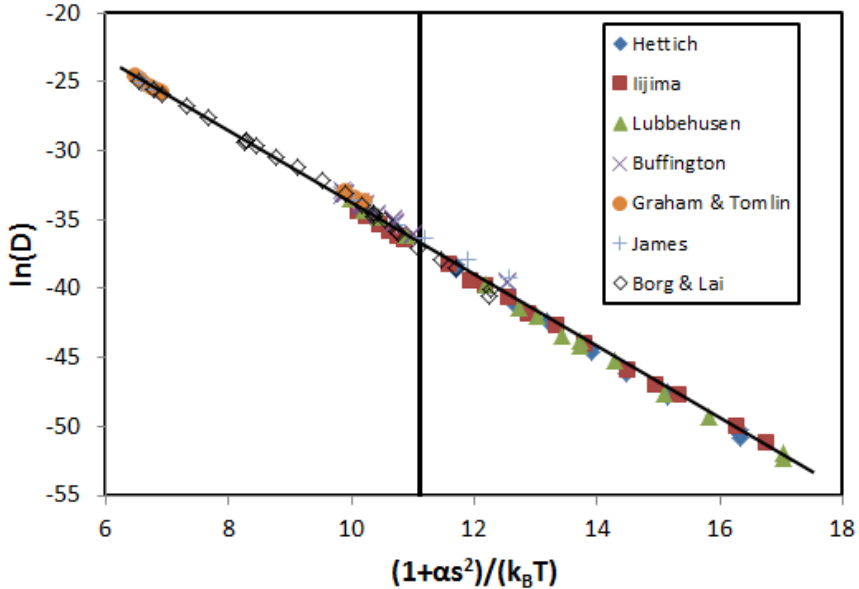
Figure 3.9: Plot of $\ln(D)$ for pure iron self-diffusion against $(1 + \alpha s^2)/(k_B T)$ with $\alpha = 0.16$. The straight line indicates that this fit is reasonable for this wide temperature range. Data of iron self-diffusion is taken from [1–5, 35, 40].

instability of the bcc phase, which could locally transform to an omega phase [64].

The deviation from Arrhenius behaviour makes the modelling of the diffusivity complicated [65], it is required to take into account phonon mode softening with temperature, as shown by Mikhin and Osetsky [66]. The effect is not quite so large in bcc Fe, but could be similar to bcc Zr diffusion. The softening of phonons have been calculated for bcc-iron [67–70], showing a magnon-phonon coupling which causes the remarkable softening of specific stiffness directions [10, 11]. Directionally phonon softening is a precursor for an unstable crystal structure. It is possible that this then affects the structure and electron density of the transition state and thereby the activation barrier for diffusion. The analysis of Ding and coworkers [37] shows that in fcc Cobalt there is barely any magnetic effect on the diffusivity. This could be due to the stability of this close-packed crystal structure. The difference with bcc iron cannot be explained by a significant difference in magnetic enthalpies, or in a significant difference in the magnitude of the magnetic moments, since the magnetic moments on atoms are very similar for cobalt and iron.

The bcc iron diffusivity around the Curie temperature has also been evaluated [28] for grain-boundary diffusion [21], and for dislocation pipe diffusion [22]. The deviation from Arrhenius relation is much more pronounced. This coincides with a much higher degree of ionic disorder, which in turn coincides with increased magnitudes of the spins. A special case is the equi-atomic Fe-Co alloy, which has a phase transformation from bcc to fcc at 1003 K. A deviation from linearity can be seen below this transition temperature, but not above it [71]. The deviation from Arrhenius relation due to the
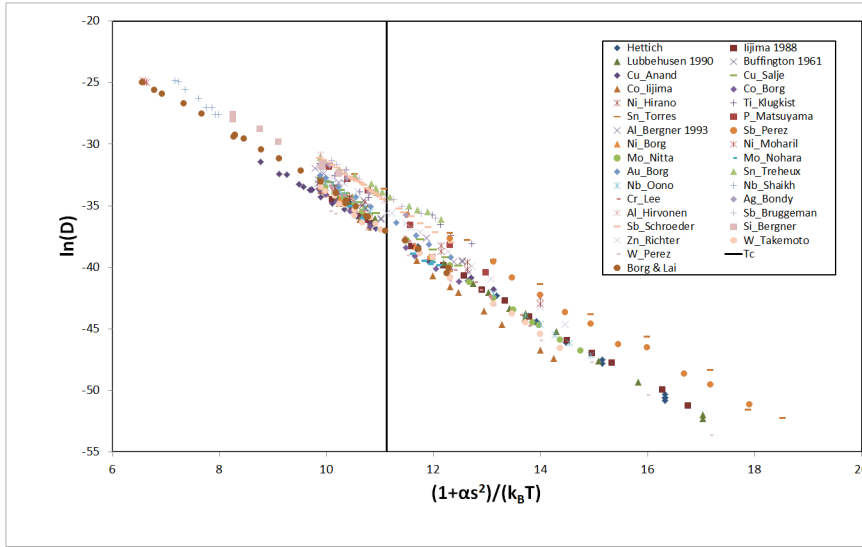
Figure 3.10: Plot of ln(D) against $(1 + \alpha s^2)/(k_B T)$. With $\alpha = 0.10$ for impurities and $\alpha = 0.16$ for iron self-diffusion. The validity of the approach is confirmed by the straight lines obtained. Data used: Fe [1–3, 5, 40], Cu [25, 49], Co [16, 45], Ni [45, 46, 55], Ti [27], Sn [24, 56], P [51], Al [26, 52], Sb [19, 50, 57], Mo [20, 58], Au [45], Nb [18, 59], Cr [23], Ag [47], V [60], Si [61], Zn [48], W [17, 62].

magnetic effect occurs only in the bcc crystal structure for this alloy and not at higher temperature in fcc, despite both these faces being below the Curie temperature.

Both the Jönsson model, and the Girifalco model lead to a similar conclusion: the magnitude of the interaction parameter is species independent. The only characteristic difference is in evaluating the magnetic effect on the barrier for diffusion as fraction of the energy related to short and long-range magnetic ordering, or only the energy related to long-range magnetic order. During an atomic jump through the transition state, the magnetic fluctuations cause magnetic clusters to flip with certain frequencies. The size of those clusters and their fluctuation time of magnetic cluster in paramagnetic state and in ferromagnetic state vary with temperature. This variation is particularly large close to the Curie temperature[72], which might be related to the activation energy for diffusion in paramagnetic state.

The actual mechanism behind the anomalous effect in diffusion of bcc iron seems to be based on the directional softening of shear modes in the bcc crystal. This can be related to the magnetic ordering. The phonon mode softening seems to be similar to softening observed in bcc-Zr, which shows a much more significant deviation from Arrhenius relation diffusion behaviour. The manner of determining the magnitude of this phenomenon should be based on calculation the temperature and magnetic order dependent phonon frequency spectra.

3.6. CONCLUSIONS

When predicting the magnetic effect on diffusion in bcc iron, for self-diffusion and for impurity diffusion the Girifalco model can be used with a constant $\alpha = 0.10(1)$ for all impurity elements. The deviation from Arrhenius behaviour seems to be due to stiffness and phonon mode softening close to the Curie temperature. Whether this is modelled using the Jönsson approach, or the Girifalco model seems almost equivalent. If we assume the value of the activation barrier for diffusing in ferromagnetic state Q_{FM} can be calculated. The greatest distinction between these models is the resulting paramagnetic activation barrier Q_{PM}, which is significantly lower when the Jönsson model is used. The low value of Q_{PM} does not agree with the most reliable first-principle modelling, and neither with most of the data of iron self-diffusion over a wide range of temperatures in the paramagnetic state, in binary Fe-X alloys. Therefore, the best method of modelling the effect of magnetism on the diffusivity within iron is the Girifalco model with $\alpha = 0.10(1)$ for impurity elements in iron. In the case of iron self-diffusion a higher effect is found in literature and the value of $\alpha = 0.16(1)$.

REFERENCES

[1] M. Lübbehusen and H. Mehrer, *Self-diffusion in α-iron: The influence of dislocations and the effect of the magnetic phase transition,* Acta Metall. Mater. **38**, 283 (1990).

[2] Y. Iijima and K. Hirano, *Self-diffusion and isotope effect in α-iron,* Acta Metall. **36**, 2811 (1988).

[3] G. Hettich, H. Mehrer, and K. Maier, *Self-diffusion in ferromagnetic α-iron,* Scr. Metall. **11**, 795 (1977).

[4] D. W. James and G. M. Leak, *Self-diffusion and diffusion of cobalt in alpha and delta-iron,* Philos. Mag. **14**, 701 (1966).

[5] F. S. Buffington, K. Hirano, and M. Cohen, *Self diffusion in iron,* Acta Metall. **9**, 434 (1961).

[6] U. Bergmann, S. D. Shastri, D. P. Siddons, B. W. Batterman, and J. B. Hastings, *Temperature Dependence of nuclear forward scattering of synchrotron radiation in α-57Fe,* Phys. Rev. B **50**, 5957 (1994).

[7] A. S. Arrott and B. Heinrich, *Application of magnetization measurements in iron to high temperature thermometry,* J. Appl. Phys. **52**, 2113 (1981).

[8] M. Hillert and M. Jarl, *A model for alloying in ferromagnetic metals,* Calphad **2**, 227 (1978).

[9] Y. Y. Chuang, R. Schmid, and Y. A. Chang, *Magnetic contributions to the thermodynamic functions of pure Ni, Co, and Fe,* Metall. Trans. A **16**, 153 (1985).

[10] V. A.M., *High Temperature Phonons in Iron,* J. Phys. **12**, 398 (1981).

[11] J. Neuhaus, W. Petry, and a. Krimmel, *Phonon softening and martensitic transformation in α-Fe,* Phys. B Condens. Matter **234**-**236**, 897 (1997).

[12] D. J. Dever, *Temperature dependence of the elastic constants in α-iron single crystals: Relationship to spin order and diffusion anomalies,* J. Appl. Phys. **43**, 3293 (1972).

[13] R. J. Borg, *Diffus. body-centered cubic Met.* (Chapman & Hall, London, 1965) p. 225.

[14] L. Girifalco, *Activation energy for diffusion in ferromagnets,* J. Phys. Chem. Solids **23**, 1171 (1962).

[15] L. Ruch, D. R. Sain, H. L. Yeh, and L. A. Girifalco, *Analysis of diffusion in ferromagnets,* J. Phys. Chem. Solids **37**, 649 (1976).

[16] Y. Iijima, K. Kimura, C.-G. Lee, and K. Hirano, *Impurity Diffusion and Isotope Effect of Cobalt in α-Iron,* Mater. Trans. JIM **34**, 20 (1993).

[17] S. Takemoto, H. Nitta, Y. Iijima, and Y. Yamazaki, *Diffusion of tungsten in α-iron,* Philos. Mag. **87**, 1619 (2007).

[18] N. Oono, H. Nitta, and Y. Iijima, *Diffusion of niobium in .ALPHA.-iron,* Mater. Trans. **44**, 2078 (2003).

[19] R. A. Pérez, D. N. Torres, and F. Dyment, *Sb diffusion in α-Fe,* Appl. Phys. A Mater. Sci. Process. **81**, 787 (2005).

[20] H. Nitta, T. Yamamoto, R. Kanno, K. Takasawa, T. Iida, Y. Yamazaki, S. Ogu, and Y. Iijima, *Diffusion of molybdenum in α-iron,* Acta Mater. **50**, 4117 (2002).

[21] A. Inoue, H. Nitta, and Y. Iijima, *Grain boundary self-diffusion in high purity iron,* Acta Mater. **55**, 5910 (2007).

[22] Y. Shima, Y. Ishikawa, H. Nitta, Y. Yamazaki, K. Mimura, M. Isshiki, and Y. Iijima, *Self-Diffusion along Dislocations in Ultra High Purity Iron,* Mater. Trans. **43**, 173 (2002).

[23] C.-G. Lee, Y. Iijima, T. Hiratani, and K.-i. Hirano, *Diffusion of Chromium in alpha iron,* Mater. Trans. JIM **31**, 255 (1990).

[24] D. N. Torres, R. A. Perez, and F. Dyment, *Diffusion of tin in α-iron,* Acta Mater. **48**, 2925 (2000).

[25] G. Salje and M. Feller-Kniepmeier, *The diffusion and solubility of copper in iron,* J. Appl. Phys. **48**, 1833 (1977).

[26] D. Bergner and Y. Khaddour, *Impurity and Chemical Diffusion of Al in BCC and FCC Iron,* Defect Diffus. Forum **95-98**, 709 (1993).

[27] P. Klugkist and C. Herzig, *Tracer diffusion of titanium in α-iron,* Phys. Status Solidi **148**, 413 (1995).

[28] Y. Iijima, *Diffusion in high-purity iron: Influence of magnetic transformation on diffusion,* J. Phase Equilibria Diffus. **26**, 466 (2005).

[29] H. Ding, S. Huang, G. Ghosh, P. K. Liaw, and M. Asta, *A computational study of impurity diffusivities for 5d transition metal solutes in α-Fe,* Scr. Mater. **67**, 732 (2012).

[30] B. Jönsson, *On ferromagnetic ordering and lattice diffusion,* Zeitschrift für Met. **83**, 349 (1992).

[31] L. Messina, M. Nastar, T. Garnier, C. Domain, and P. Olsson, *Exact ab initio transport coefficients in bcc Fe-X (X=Cr, Cu, Mn, Ni, P, Si) dilute alloys,* Phys. Rev. B **90**, 104203 (2014).

[32] L. Messina, M. Nastar, N. Sandberg, and P. Olsson, *Systematic electronic-structure investigation of substitutional impurity diffusion and flux coupling in bcc iron,* Phys. Rev. B **93**, 184302 (2016).

[33] J. O. Andersson, T. Helander, L. Hoglund, P. Shi, and B. Sundman, *Thermo-Calc & DICTRA, computational tools for materials science,* Calphad Comput. Coupling Phase Diagrams Thermochem. **26**, 273 (2002).

[34] Y. Liu, L. Zhang, Y. Du, and D. Liang, *Ferromagnetic ordering and mobility end-members for impurity diffusion in bcc Fe,* Calphad Comput. Coupling Phase Diagrams Thermochem. **33**, 732 (2009).

[35] D. Graham and D. H. Tomlin, *Self-diffusion in iron,* Philos. Mag. **8**, 1581 (1963).

[36] A. V. Ruban and V. I. Razumovskiy, *Spin-wave method for the total energy of paramagnetic state,* Phys. Rev. B **85**, 174407 (2012).

[37] H. Ding, V. I. Razumovskiy, and M. Asta, *Self diffusion anomaly in ferromagnetic metals: A density-functional-theory investigation of magnetically ordered and disordered Fe and Co,* Acta Mater. **70**, 130 (2014).

[38] N. Sandberg, Z. Chang, L. Messina, P. Olsson, and P. Korzhavyi, *Modeling of the magnetic free energy of self-diffusion in bcc Fe,* Phys. Rev. B **92** (2015), 10.1103/PhysRevB.92.184102.

[39] B. Million, *Diffusion of Fe-59 in α-Fe-Si alloys,* Czech. J. Phys. B **27**, 928 (1977).

[40] R. J. Borg and D. Y. F. Lai, *Diffusion in α-Fe-Si Alloys,* J. Appl. Phys. **41**, 5193 (1970).

[41] C. D. Versteylen, N. H. van Dijk, and M. H. F. Sluiter, *First-principles analysis of solute diffusion in dilute bcc Fe-X alloys,* Phys. Rev. B **96**, 094105 (2017).

[42] X. Gao, H. Ren, C. Li, H. Wang, Y. Ji, and H. Tan, *First-principles calculations of rare earth (Y, la and Ce) diffusivities in bcc Fe,* J. Alloys Compd. **663**, 316 (2016).

[43] C. Zhang, J. Fu, R. Li, P. Zhang, J. Zhao, and C. Dong, *Solute/impurity diffusivities in bcc Fe: A first-principles study,* J. Nucl. Mater. **455**, 354 (2014).

[44] S. Huang, D. L. Worthington, M. Asta, V. Ozolins, G. Ghosh, and P. K. Liaw, *Calculation of impurity diffusivities in α-Fe using first-principles methods,* Acta Mater. **58**, 1982 (2010).

[45] R. J. Borg and D. Y. F. Lai, *The diffusion of gold, nickel, and cobalt in alpha iron: A study of the effect of ferromagnetism upon diffusion,* Acta Metall. **11**, 861 (1963).

[46] K. Hirano, M. Cohen, and B. Averbach, *Diffusion of nickel into iron,* Acta Metall. **9**, 440 (1961).

[47] A. Bondy and V. Levy, *Etude de la diffusion de l'argent dans le fer alpha.* C. R. Acad. Sci. Paris Ser. C **272**, 19 (1971).

[48] I. Richter, *Diffusion of Zn in alpha-Fe Single Crystals,* Phys. Status Solidi **68**, 289 (1981).

[49] M. S. Anand and R. P. Agarwala, *Diffusion of copper in iron,* J. Appl. Phys. **37**, 4248 (1966).

[50] G. A. Bruggeman and J. A. Roberts, *The diffusion of antimony in alpha iron,* Metall. Trans. A **6**, 755 (1975).

[51] T. Matsuyama, H. Hosokawa, and H. Suto, *Tracer diffusion of P in Iron and iron alloys,* Trans. Japan Inst. Met. **8**, 589 (1983).

[52] J. Hirvonen and J. Räisänen, *Diffusion of aluminum in ion-implanted alpha iron,* J. Appl. Phys. **53**, 3314 (1982).

[53] P. K. Liaw, M. D. Asta, D. C. Dunand, M. E. Fine, G. Ghosh, C. Liu, H. Ding, S. Huang, M. Rawlings, Z. Sun, G. Song, and Z. Teng, *Computational design of creep resistant alloys and experimental validation in ferritic superalloys*, Tech. Rep. (2013).

[54] P. J. Alberry and C. W. Haworth, *Alberry (1974) # Interdiffusion of Cr Mo and W in Iron.pdf,* Met. Sci. J. **8**, 407 (1974).

[55] D. B. Moharil, I. Jin, and G. R. Purdy, *The effect of delta- ferrite formation on the post-solidification homogenization of alloy steels,* Metall. Trans. **5**, 59 (1974).

[56] D. Treheux, D. Marchive, J. Delagrange, and P. Guiraldenq, *Determination des coefficients d'heterodiffusion a dilution infinie dans le fer α,* C. R. Acad. Sci. Ser. C **274**, 1260 (1972).

[57] A. Schröder and M. Feller-Kniepmeier, *The Ferromagnetic Diffusion Anomaly of the Diffusion System Iron-Antimony,* Phys. Stat. Sol. **107**, 107 (1988).

[58] K. Nohara and K.-i. Hirano, *self-diffusion in the Fe-Mo system Nohara,* J. Jpn. Inst. Met. **40**, 1053 (1976).

[59] Q. A. Shaikh, *Interdiffusion measurement of niobium and tantalum in iron base alloys,* Mater. Sci. Technol. **6**, 1177 (1990).

[60] J. Geise and C. Herzig, *Impurity diffusion of vanadium and self-diffusion in iron,* Z. Met. **78**, 291 (1987).

[61] D. Bergner, Y. Khaddour, and S. Lörx, *Diffusion of Si in bcc- and fcc-Fe,* Defect Diffus. Forum **66-69**, 1407 (1990).

[62] R. A. Pérez and D. N. Torres, *W diffusion in paramagnetic and ferromagnetic α-Fe,* Appl. Phys. A Mater. Sci. Process. **104**, 329 (2011).

[63] C. Herzig, *Diffusion and Soft Phonons in BCC Metals,* in *Diffus. Mater.*, edited by A. L. Laskar, J. L. Bocquet, G. Brebec, and C. Monty (Springer Netherlands, Dordrecht, 1990) pp. 287–296.

[64] D. de Fontaine, *Simple models for the omega phase transformation,* Metall. Trans. A **19**, 169 (1988).

[65] M. I. Mendelev and B. S. Bokstein, *Molecular dynamics study of self-diffusion in Zr,* Phil.Mag. **90**, 637 (2010).

[66] A. G. Mikhin and Y. N. Osetsky, *On normal and anomalous self-diffusion in body-centred cubic metals: a computer simulation study,* J. Phys. Condens. Matter **5**, 9121 (1993).

[67] I. Leonov, A. I. Poteryaev, V. I. Anisimov, and D. Vollhardt, *Calculated phonon spectra of paramagnetic iron at the α-γ Phase transition,* Phys. Rev. B **85**, 020401 (2012).

[68] I. Leonov, A. I. Poteryaev, Y. N. Gornostyrev, A. I. Lichtenstein, M. I. Katsnelson, V. I. Anisimov, and D. Vollhardt, *Electronic correlations determine the phase stability of iron up to the melting temperature,* Sci. Rep. **4**, 5585 (2015).

[69] F. Körmann, B. Grabowski, B. Dutta, T. Hickel, L. Mauger, B. Fultz, and J. Neugebauer, *Temperature dependent magnon-phonon coupling in bcc Fe from theory and experiment,* Phys. Rev. Lett. **113**, 165503 (2014).

[70] F. Körmann, A. Dick, B. Grabowski, T. Hickel, and J. Neugebauer, *Atomic forces at finite magnetic temperatures: Phonons in paramagnetic iron,* Phys. Rev. B **85**, 125104 (2012).

[71] Y. Iijima and C. G. Lee, *Self-diffusion in B.C.C. and ordered phases of an equiatomic iron-cobalt alloy,* Acta Metall. Mater. **43**, 1183 (1995).

[72] W. Pepperhoff and M. Acet, *Const. Magn. Iron its Alloy.*, 1st ed., Engineering Materials and Processes (Springer, 2001) pp. 104–115.

3

4

FINITE ELEMENT MODELING OF CREEP CAVITY FILLING BY SOLUTE DIFFUSION

Double rainbow all the way across the sky! Oh my god. Oh my god. Oh god.
What does this mean? Oh. Oh my god. Oh. Oh. God. Its so bright,
oh my god its so bright and vivid!

Paul "Bear" Vasquez

In recently discovered self-healing creep steels, open-volume creep cavities are filled by the precipitation of supersaturated solute. These creep cavities form on the grain boundaries oriented perpendicular to the applied stress. The presence of a free surface triggers a flux of solute from the matrix, over the grain boundaries towards the creep cavities. We studied the creep cavity filling by finite element modeling and found that the filling time critically depends on (i) the ratio of diffusivities in the grain boundary and the bulk, and (ii) on the ratio of the intercavity distance and the cavity size. For a relatively large intercavity spacing, 3D transport is observed when the grain boundary and volume diffusivities are of a similar order of magnitude, while a 2D behavior is observed when the grain boundary diffusivity is dominant. Instead when the intercavity distance is small, the transport behavior tends to a 1D behavior in all cases, as the amount of solute available in the grain boundary is insufficient. A phase diagram with the transition lines is constructed.

4.1. INTRODUCTION

When metals are subjected to a load at high temperature, creep damage can occur in the form of creep cavities. These cavities grow under the influence of stress which can lead to failure. Generally, strategies are adopted to prevent creep damage to form, or slow down its growth [2, 3]. An alternative method in the form of self-healing has been proposed by Laha and coworkers [4] and Shinya [5], where selective precipitation of supersaturated solute at creep cavities hinders the creep cavity growth in stainless steels. This mechanism was modelled by Karpov and coworkers [6]. Zhang and coworkers subsequently demonstrated that precipitation of substitutional solute leads to the self-healing of creep cavities in Fe-Au and Fe-Mo alloys [7–9]. The creep defects and repairing precipitates were studied in detail for Fe-Au self-healing creep alloys, using X-ray nanotomography [10]. It was found that the creep cavity growth and the precipitate growth directly affect the strain rate of the alloys. Additional scanning electron microscopy studies indicated a close similarity between the precipitation mechanism at the outer surface [11], compared to the precipitation on the creep cavity surface within the material [10].

Creep cavity growth by the diffusional flux of vacancies over grain boundaries has been described by Herring [12], and Hull and Rimmer [13]. Who propose that the driving force for vacancies to migrate to the creep cavities is a function of the applied stress. The effect of strain rate in the bulk material on the creep cavity growth was treated in finite-element calculations by Needleman and Rice [14]. The role of stress states around creep cavities, and the effect of the intercavity distance implemented in the model proposed by Needleman and Rice was investigated by van der Giessen [15]. In all of these studies, the vacancy transport is solely along the grain-boundary, by grain-boundary diffusion.

Zener first treated the bulk-diffusion dominated growth of spherical precipitates in a homogeneous bulk material [16]. In the case of precipitate growth on grain-boundaries, both the diffusivity in bulk and on the grain-boundary play an essential role. The fast diffusion along grain boundaries acts as a collector plate to accumulate solute [17], or diffuse solute in the case of precipitate dissolution [18, 19].

The aim of the present paper is to quantitatively estimate the time required to fill a creep cavity by solute precipitation as a function of several key modelling parameters such as: the creep cavity size, the intercavity spacing, the concentration of supersaturated solute, the grain-boundary diffusivity, and the volume diffusivity. We also aim to show the influence of the diffusivities and intercavity distance on the 1D, 2D, or 3D character of the diffusion field and therefore its influence on the rate of filling. The growth rate of a precipitate can change character during the life-time of a material. This change of character can play a significant role in the behaviour of creep-resistant alloys, as they have long service lives at high temperature.

4.2. METHODS

The diffusional flux of substitutional solute towards the creep cavity is evaluated using finite element modeling (FEM). The modelling was performed using the Sepran software

[20, 21]. The diffusional flux $\vec{J}$ is modelled as,

$$\vec{J} = -\frac{D}{\Omega}\vec{\nabla}c, \tag{4.1}$$

where D is the diffusivity, Ω is the atomic volume (i.e. the volume of a single atom in the bcc crystalline iron), and c is the solute concentration in atomic fraction. Assuming that the driving force for diffusion originates only from a gradient in concentration ($\vec{\nabla}c$), and that the atomic volume of the solute atom is equal to the volume of an iron atom in the bcc lattice (Ω). The diffusional flux of solute towards a the volume of a lens-shaped cavity is evaluated at the surface of the cavity S:

$$\frac{dN}{dt} = -\oiint_S \vec{J} \cdot \vec{dS}. \tag{4.2}$$

The diffusional flux arriving at the creep-cavity surface S results in a number of ingressing atoms N per unit of time t. The precipitate then grows inside the creep cavity until the number of atoms that have ingressed is sufficient to fill the volume V of the original creep cavity ($N\Omega = V$). The fraction of filling f then corresponds to $f = N\Omega/V$ (with $f = 1$ at complete filling).

As indicated in figure 4.1, the simulation volume is a cylinder of radial dimension r and vertical dimension z. The simulation box has a radius λ, and a box height H. The grain boundary thickness amounts to $\delta = 0.5$ nm, the creep cavity radius is chosen to be $a = 50$ nm, and the atom volume of bcc iron is $\Omega = 0.0117$ nm^3 (for a lattice parameter of 0.286 nm).

The boundary conditions are: (1) the concentration at the edge of the creep cavity ($r = a$) is kept at a constant level c_1, (2) the starting concentration in the matrix and grain boundary is chosen to be equal to the nominal concentration c_0, and (3) at the edge of the simulation box ($r = \lambda$ and $z = H$), the diffusional flux is chosen to be zero. The box radius λ corresponds to half the intercavity spacing on the grain boundary ($z = 0$). A small box radius therefore corresponds to a high cavity concentration on the grain boundary. The box height H, was chosen to always be sufficiently large, so that the concentration remains equal to the nominal concentration at the vertical box edge, for the times up until complete filling.

The ratio λ/a is a characteristic parameter in the modelling of the creep cavity filling. In our simulations we used the following values for the intercavity ratios: $\lambda/a = 2$, 3, 5, 10, 20, 50, 100, 200, and 400. We varied the grain-boundary diffusivity (D_{gb}) over 9 orders of magnitude and the volume diffusivity D_V in the bulk of the matrix over 10 orders of magnitude. The shape of the cavities on grain edges, corners, and on precipitates has been analysed by Raj & Ashby [22]. The creep cavities that form on the grain boundaries are found to be self-similar over a large range of length scales. In this work we will only consider the lens-shaped cavities forming on straight grain-boundary edges perpendicular to the stress direction. For such a lens-shaped cavity, the volume is given by $V_{cav} = FV_{sphere}$ with

$$F = 1 - \frac{3}{2}\cos(\psi) + \frac{1}{2}\cos^3(\psi), \tag{4.3}$$

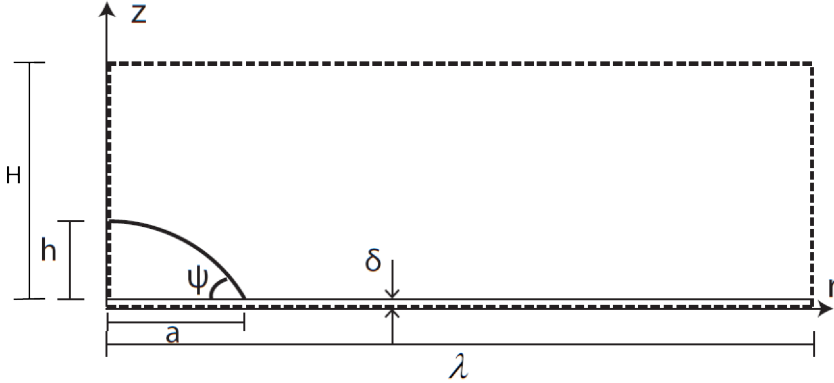Figure 4.1: Lens-shaped creep cavity defined by an opening angle ψ, a height h, and a radius a. The creep cavity is formed on a grain boundary with width δ. The simulation box is a cylinder with a radius λ and a height H.

where ψ is the opening angle and $V_{sphere} = 4\pi a^3/3$ is the volume of a sphere with radius a. For metals the equilibrium opening angle ψ is estimated at 75°, following the approach by Raj and Ashby [22], resulting in a scale factor of $F \approx 0.62$. The height of the creep cavity directly scales with the cavity radius a with $h/a = (1 - \cos\psi)/\sin(\psi) \approx 0.77$.

Throughout the simulations the nominal concentration is chosen to be $c_0 = 0.01$, with an edge concentration of $c_1 = 0.0001$, in order to reflect the experimental situation for self-healing in Fe-Au alloys [7, 8, 10]. As a consequence, the supersaturation Δc is comparable to the nominal concentration c_0.

4.3. RESULTS

In figure 4.2 the concentration profile at the time of creep cavity filling is shown for $\lambda/a = 20$ and $\lambda/a = 2$, and for three different ratio's of D_{gb}/D_V. It can be seen that the character of the diffusional field where the solute is depleted critically depends on both diffusivity and size ratio. The axially symmetric cavity can have either a 3D, 2D, or 1D diffusion field, depending on λ/a and D_{gb}/D_V. For the ratio of $\lambda/a = 2$ the diffusion field has a 1D character with a concentration gradient towards the grain boundary and the creep cavity. For the ratio of $\lambda/a = 20$, the diffusion field has a 3D character for $D_{gb}/D_V \approx 1$, and a 2D character for $D_{gb}/D_V \gg 1$.

In figure 4.3 the filling time of the creep cavity as a result of the diffusional solute flux towards the creep cavity is shown as a function of the grain-boundary diffusivity and the volume diffusivity, for different ratio's of λ/a. For the smallest ratio of $\lambda/a = 2$, the filling time is only controlled by D_V. This is consistent with the results of figure 4.2, where the diffusion field always shows a 1D character for $\lambda/a = 2$. For $\lambda/a = 5$ and $\lambda/a = 20$, in figure 4.3, a clear transition is observed for a specific ratio of diffusivities. For a relatively high grain-boundary diffusion, the grain boundary is depleted faster, leading to a 1D diffusion for most of the filling time. For $\lambda/a = 400$, both the grain boundary and volume diffusivity control the filling time. Based on these observations it

is useful to introduce a dimensionless time τ:

$$\tau = \frac{D_V t}{a^2}. \tag{4.4}$$

In figure 4.4, τ_{fill} is shown for different ratio's of λ/a. For the 1D and 3D conditions, where the volume diffusion is rate-limiting, the dimensionless filling time τ_{fill} is now independent of the volume diffusion D_V. For large values of λ/a, τ_{fill} is also independent of λ/a. For a large ratio of λ/a and $D_{gb}/D_V = 1$, the diffusion field has a 3D character. However, when the grain-boundary diffusivity is much larger than the volume diffusivity $D_{gb} \gg D_V$, the diffusion field shows a distinct 2D character. In figure 4.5, the dimensionless filling time (τ_{fill}) is plotted as function of the geometric ratio (λ/a) and the diffusivity ratio (D_{gb}/D_V). τ_{fill} is found to depend on both the ratio of diffusivities and the geometric ratio. For $\lambda/a > 50$ only the diffusivity ratio defines the dimensionless filling time. In this case, for high diffusivity ratios τ_{fill} scales as $t_{fill} \propto (D_{gb}/D_V)^{-1}$, as t_{fill} is then controlled by D_{gb} only.

The diffusion profile can be 3D, 2D, or 1D in nature. In order to evaluate which of these occurs, one can use the diffusion length at the filling $2\sqrt{Dt_{fill}}$. When the diffusion length for grain-boundary and/or volume diffusion exceeds the box radius λ, a cross-over in behavior occurs. In order to further evaluate the nature of the diffusion process, the amount of atoms ingressing in the creep cavity as function of time can approximated by a power law;

$$N(t) = Kt^\nu, \tag{4.5}$$

where N is the number of solute atoms collected in the cavity, K is a constant and ν is
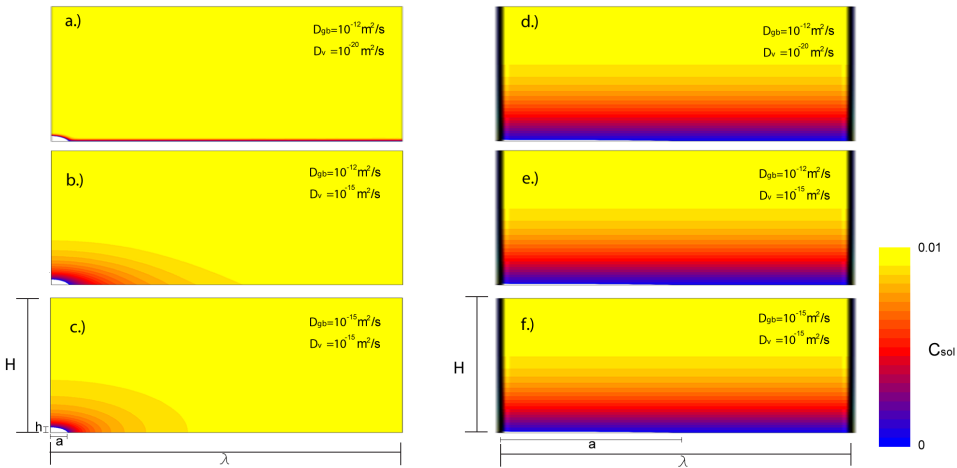
Figure 4.2: Solute concentration around the cavity at the time of filling. a.) $\lambda/a = 20$, and $D_{gb}/D_V = 10^8$. b.) $\lambda/a = 20$, and $D_{gb}/D_V = 10^3$. c.) $\lambda/a = 20$, and $D_{gb}/D_V = 1$. d.) $\lambda/a = 2$, and $D_{gb}/D_V = 10^8$. e.) $\lambda/a = 2$, and $D_{gb}/D_V = 10^3$. f.) $\lambda/a = 2$, and $D_{gb}/D_V = 1$. All data are for a supersaturation of $\Delta c = 0.01$. For $\lambda/a = 2$, the grain boundary contains insufficient solute, and as a result, a quasi-1D profile is observed at the time of filling, independent of the ratio D_{gb}/D_V.

4
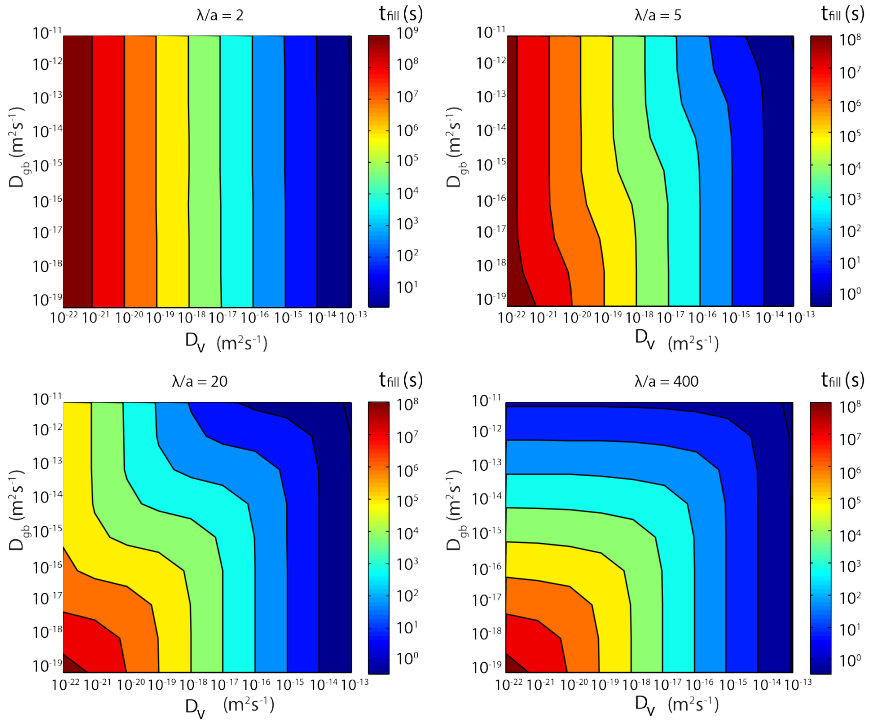
Figure 4.3: Filling time for different ratio's of λ/a (2, 5, 20, 400). The filling time depends only on the volume diffusivity for small λ/a, and evolves to the situation where both diffusivities contribute. All data are for a supersaturation level of $\Delta c = 0.01$.
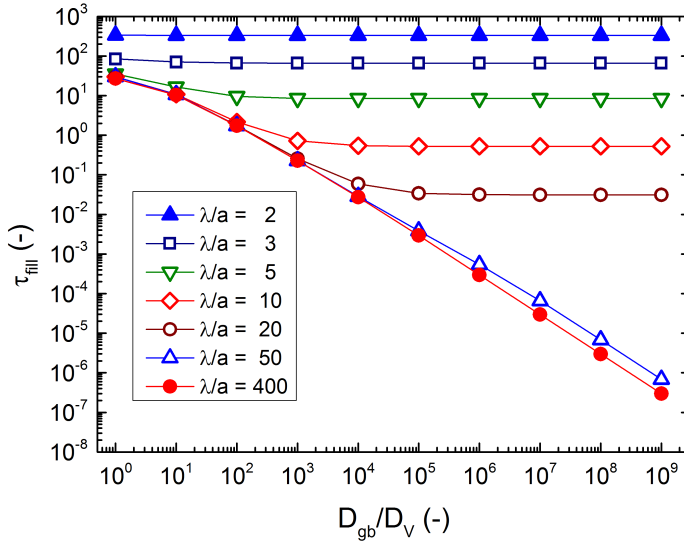
Figure 4.4: Dimensionless filling time τ_{fill}, as function of the diffusivity ratio D_{gb}/D_V. The ratio λ/a defines at which diffusivity ratio the diffusion length impinges the edge of the box at $r = \lambda$. All data are for a supersaturation of $\Delta c = 0.01$.
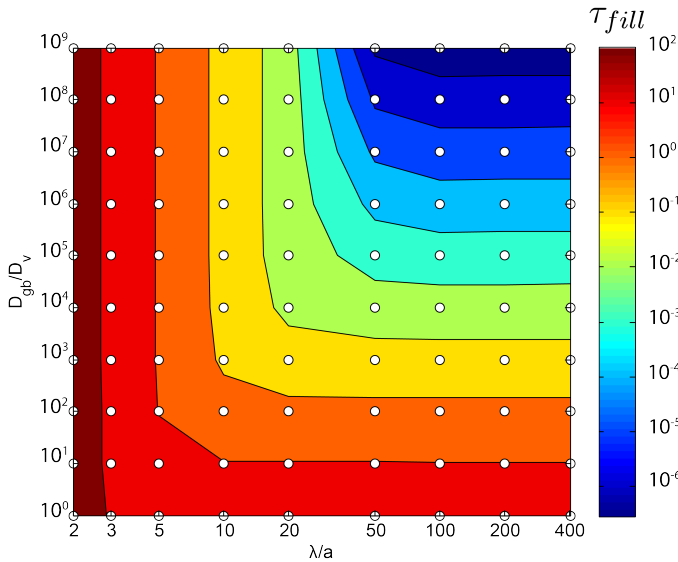
Figure 4.5: Dimensionless filling time τ_{fill} as a function of λ/a and D_{gb}/D_V. All data are for a supersaturation of $\Delta c = 0.01$.
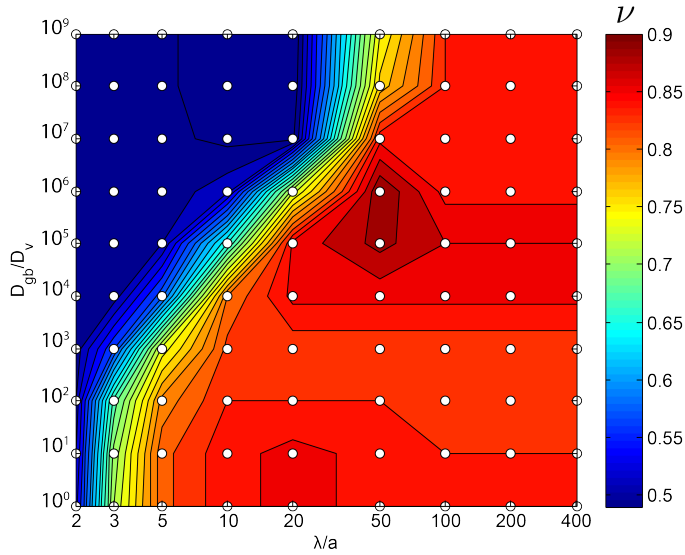
Figure 4.6: Time exponent ν for cavity filling kinetics as a function of λ/a and D_{gb}/D_V. All data are for a supersaturation of $\Delta c = 0.01$.

the time exponent, which can be obtained by fitting the simulation results for $N(t)$ to equation 4.5. $N(t)$ is obtained by integrating the atom flux from equation 4.2.

The time exponent for the filling kinetics of the creep cavity depends on the dimensional character: for 1D one finds $\nu = 0.5$, and for both 2D and 3D ν starts at 0.5 and gradually tends to 1.0 over time (see appendix I). As shown in figure 4.6, a 1D character ($\nu = 0.5$) is observed for low values of λ/a, while a 2D/3D character (with $\nu \approx 0.85$) is observed for high values of λ/a. This is consistent with the result from figures 2-5.

4.4. DISCUSSION

The dimensional character of the solute transport towards the cavity has a large effect on the filling time. For a small λ/a ratio the solute transport is purely 1D and is controlled by the diffusivity through the bulk towards the grain boundary and creep cavity. The diffusion length required for filling, can be estimated from the grain-boundary surface area (scaling as $S \propto \lambda^2$). The resulting 1D diffusion length $2\sqrt{D_V t_{fill}}$ scales as $V/S\Delta c$, where the volume of the creep cavity scales as $V \propto a^3$. This leads to a dimensionless filling time of $\tau_{fill} \propto (\lambda/a)^{-4}\Delta c^{-2}$. This scaling behavior can be observed for small λ/a in figure 4.4.

For larger λ/a ratios, the filling time depends on D_{gb}/D_V. When $D_{gb} = D_V$, the filling of the creep cavity takes on a 3D character. When the creep cavity is assumed to be spherical, the exact solution for the solute flux on the creep cavity boundary at $r = a$ is (see Appendix I):

$$J(r = a) = \frac{D_V \Delta c}{a}\left(1 + \frac{1}{\sqrt{\pi\tau}}\right). \tag{4.6}$$
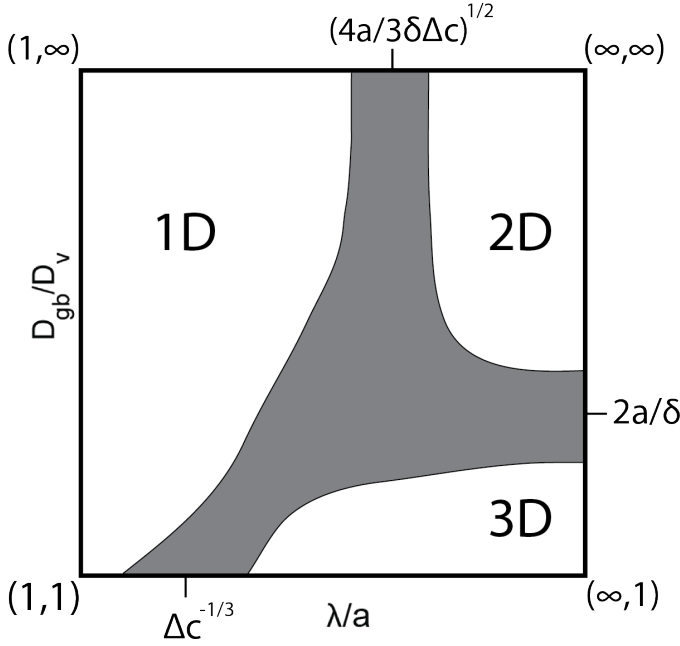
Figure 4.7: Phase diagram for the diffusional character of creep cavity filling by supersaturated solute, as a function of the diffusivity ratio D_{gb}/D_v and the characteristic length scale ratio λ/a. 3 different regimes with 1D, 2D, and 3D diffusion are observed. The characteristic values for the cross-over between these regimes are indicated.

The filling fraction then corresponds to $f(\tau) = 3\Delta c \left(\tau + \sqrt{\frac{4\tau}{\pi}}\right)$. The second term represents the quasi-1D behavior for short times ($f \propto \sqrt{\tau}$), and the first term refers to the behavior at large times ($f \propto \tau$). Based on the long-time contribution the dimensionless time to filling can be approximated as $\tau_{fill} \approx \frac{1}{3\Delta c}$.

When the diffusivity ratio D_{gb}/D_V increases ($D_{gb}/D_V \gg 1$), while the intercavity distance λ is large enough to provide the solute required to fill the cavity from the grain boundary ($\lambda/a \gg 1$), the diffusion is of 2D character. This means that the filling time depends only on the grain-boundary diffusivity and the grain-boundary width. For 2D diffusional behavior, the grain-boundary diffusivity is rate controlling, with a time exponent $\nu \approx 1$. A dimensionless filling time of the following form is now expected;

$$\tau_{fill} \propto \frac{1}{\Delta c} \frac{aD_V}{\delta D_{gb}}. \tag{4.7}$$

In figure 4.4, it is clear that only the grain-boundary diffusivity D_{gb} plays a role in filling, then $\tau_{fill} \propto D_V/D_{gb}$. For those cases where grain-boundary diffusion is dominant until impingement occurs (such as in $\lambda/a = 5$, 10, or 20), the 2D character of filling changes after impingement to 1D. After impingement, the value of τ_{fill} becomes constant. In figure 4.7 the nature of the transport behavior is indicated as function of λ/a and D_{gb}/D_V. For a high λ/a ratio, and for $D_{gb}/D_V = 1$, the character of the solute transport

is 3D. When the diffusivity ratio D_{gb}/D_V increases, the character changes to 2D, which is reflected by the cross-over in figure 4.5. For a small λ/a ratio, an increase in the ratio D_{gb}/D_V, leads to a fast impingement. This leads to a 1D character, where the filling time only depends on the volume diffusivity. This is clearly indicated by the change in time exponent ν in figure 4.6. The phase diagram of figure 4.7, schematically summarises the results of figures 4.5 and 4.6. In order to predict the type of behavior, we can estimate the transition points between 1D, 2D, and 3D behavior. For $\lambda/a \gg 1$ a cross-over between 2D and 3D behavior is expected when the flux through the grain boundary surface connecting the cavity $S_{gb} = 2\pi a\delta$ and the flux through the bulk surface connecting the cavity $S_V \approx 4\pi a^2$ are balanced. From the flux balance $D_{gb}S_{gb} = D_V S_V$ a transition is expected for $D_{gb}/D_V \approx 2a/\delta$. For the present model parameters this cross-over takes place at $2a/\delta = 200$. In the isotropic limit where $D_{gb} = D_V$, a cross-over is expected when the solute-depleted region impinges with the box radius λ. Assuming for simplicity a complete depletion, a mass balance gives $\frac{4}{3}\pi a^3 = \Delta c \frac{4}{3}\pi \lambda^3$ with a transition between the 1D and 3D character for $\lambda/a \approx \Delta c^{-1/3}$. For $\Delta c = 0.01$, this corresponds to $\lambda/a \approx 4.6$. For $D_{gb}/D_V \gg 1$ a cross-over is expected when the solute depleted region impinges with the box radius λ. Assuming for simplicity a complete depletion a mass balance, then, results in $\frac{4}{3}\pi a^3 = \Delta c\delta\pi\lambda^2$ with a transition between the 1D and 2D character for $\lambda/a \approx \sqrt{\frac{4a}{3\delta\Delta c}}$. For our simulation parameters this occurs at $\lambda/a \approx 115$.

Precipitate growth inside a creep cavity is very similar to the heterogeneous precipitate growth on a grain boundary. The difference between the case analysed here and heterogeneous growth of precipitates on grain boundaries is in the moving boundary. If the boundary is not static, the analysis of the growth of a precipitate is much more complicated. Glicksmann evaluated the moving-boundary problem of 3D precipitate growth in relation to the static-boundary case [23], and found that for small supersaturations the difference is negligible. A similar analysis has been done by Aaron and coworkers in the context of diffusional phase transformations [24].

The growth of a single precipitate on a relatively large grain boundary has been evaluated by Aaron and Aaronson [17], and by Brailsford and Aaron [25]. Brailsford and Aaron [25] report the growth rate of the precipitate thickness S and the radius R. The volumetric growth rate obtained from this analysis, is equivalent to the filling rate in our analysis ($f \propto t^\nu$). In the experimental data of Brailsford and Aaron, this volumetric time exponent of precipitate growth on a grain boundary is between 0.72 and 1.05. Aaron and Aaronson [17] found an experimental volumetric time exponent of 0.85. These results are in excellent agreement with our predicted time exponent for precipitate growth inside creep cavities with a large intercavity distance λ/a on grain-boundaries.

The transition between these two diffusion regimes; one dominated by grain-boundary diffusion and one dominated by bulk diffusion, has been observed by Yi and coworkers [26]. This is related to the depletion of solute from the grain boundary, and subsequently transporting solute from the bulk which can be depleted in later stages of precipitate growth. Yi and coworkers showed that in practical situations, the change in character can play a significant role in growth rate of precipitates on grain boundaries.

The transition between two regimes might have been observed for creep cavity growth as well. When single creep cavities in brass were monitored by Isaac and coworkers using X-ray tomography [27], it was found that the cavity growth rates can change abruptly

during the creep life-time.

The diffusional transport character of second phase particles or the growth of creep cavities is very sensitive to the intercavity or interprecipitate distance. For our case of precipitation inside creep cavities, the nucleation of new creep cavities during creep reduces the intercavity distance. This behavior has implications on the self-healing process of creep steels, where the interdistance between creep cavities decreases until coalescence joins them. Precipitates forming on the creep cavity surfaces can grow through 2D grain-boundary diffusion, or in later stages through 1D volume diffusion. The transitions in behavior are mapped and can thereby be predicted.

4.5. CONCLUSIONS

The filling of creep cavities located on grain boundaries perpendicular to the applied stress, through the diffusional flux of supersaturated solute is modelled using finite element methods. The time required for filling depends on the volume diffusivity D_V and grain-boundary diffusivity D_{gb} and on the intercavity spacing λ with respect to the creep cavity size a. For a relatively fast grain-boundary diffusivity the geometric factor λ/a determines whether the solute can be drained from the grain boundary, or has to come primarily from the bulk. For a relatively large intercavity spacing 3D transport is observed when the grain boundary and volume diffusivities are of a similar order of magnitude, while a 2D behavior is observed when the grain boundary diffusivity is dominant. Instead, when the intercavity distance is small, the transport behavior tends to a 1D behavior in all cases, as the amount of solute available in the grain boundary is insufficient. The various regimes could be identified when the normalised time for creep cavity filling was analysed with respect to the intercavity distance and the diffusivity ratios. The kinetics of the filling fraction for 1D transport scales as $f \propto t^{0.5}$, while for 2D and 3D transport an effective scaling of approximately $f \propto t^{0.85}$ is observed. Predictions are provided for the transitions between the 3 regimes. The three regimes identified and the transition between the regimes, are experimentally found in applications where precipitation growth or creep cavity growth is observed. The accurate prediction of this regime change is important for the correct description of the growth of second phase particles or creep cavities, during long service lives.

4.6. APPENDIX: IDEAL SOLUTIONS TO 3D, 2D AND 1D DIFFUSION PROBLEMS

The mass flux of solute in a medium depends for a large part on the geometry of the problem. Of particular interest for creep cavity filling is the time dependence of the flux at the edge of the creep cavity. In this appendix the time dependence of this flux is evaluated for ideal 3D, 2D, and 1D solute transport.

4.6.1. 3D SOLUTE TRANSPORT

For a spherical cavity and isotropic diffusion ($D_{gb}/D_V = 1$) without boundaries ($\lambda/a \to \infty$), the problem has been treated analytically [23]. For a constant diffusivity

we can start from the diffusion equation in spherical coordinates;

$$\frac{\partial c}{\partial t} = D_V \left(\frac{\partial^2 c}{\partial r^2} + \frac{2}{r}\frac{\partial c}{\partial r} \right). \tag{4.8}$$

For a static position of the boundary of the creep cavity ($r = a$) the concentration profile takes the following form [23],

$$\frac{c_0 - c(r,t)}{c_0 - c_1} = \frac{a}{r} \, \mathrm{erfc}\left(\frac{r-a}{2\sqrt{D_V t}} \right) \quad \text{for} \quad r \geq a. \tag{4.9}$$

The solute flux at the edge of the creep cavity $J(r = a) = -(D_V/\Omega)(\partial c/\partial r)$, determines the filling rate of the creep cavity. The development of the concentration profile determines the diffusional flux at the edge boundary resulting in

$$J(a) = -\frac{D_V \Delta c}{a\Omega}\left(1 + \frac{a}{\sqrt{\pi D_V t}}\right) = -\frac{D_V \Delta c}{a\Omega}\left(1 + \frac{1}{\sqrt{\pi \tau}}\right). \tag{4.10}$$

Where $\Delta c = c_0 - c_1$. For short times ($\tau \ll 1/\pi$), the second term, which represents 1D diffusion, prevails. This is logical as the diffusion length is short with respect to the cavity radius for short times. For longer times ($\tau \gg 1/\pi$) the steady-state growth of a precipitate proceeds as follows,

$$J(a) \approx -\frac{D_V \Delta c}{a\Omega} \quad \text{for} \quad \tau \gg \frac{1}{\pi} \tag{4.11}$$

The filling fraction is now obtained after integration of the flux over surface area and time. In the initial stage ($\tau \ll 1/\pi$) the time exponent for the filling fraction $f \approx t^v$ is $v = 0.5$. In the later stages of filling the dominant time exponent for the filling fraction ($f \propto t^v$) for isotropic 3D diffusion is $v = 1$. In practical cases $0.5 \leq v \leq 1$ can be found.

4.6.2. 2D SOLUTE TRANSPORT
For a cylindrical cavity and isotropic grain-boundary diffusion without boundaries ($\lambda/a \to \infty$), the 2D diffusion equation corresponds to [23]

$$\frac{\partial c}{\partial t} = D_{gb}\left(\frac{\partial^2 c}{\partial r^2} + \frac{1}{r}\frac{\partial c}{\partial r} \right). \tag{4.12}$$

The concentration profile is mathematically complex, but relatively quickly approaches an equilibrium shape. For this equilibrium situation $\partial c/\partial t = 0$, providing a general solution to the concentration profile of the form [28]

$$c(r) = A + B\ln(r). \tag{4.13}$$

With boundary condition $c(r = a) = c_1$ and $c(r = \lambda) = c_0$, the concentration profile becomes [28]

$$c(r) = \frac{c_1 \ln(\lambda/r) + c_0 \ln(r/a)}{\ln(\lambda/a)}. \tag{4.14}$$

The flux at the creep cavity surface is then;

$$J(a) = -\frac{D_{gb}\Delta c}{a\Omega}\frac{1}{\ln(\lambda/a)}.$$

(4.15)

This flux corresponds to the solution for long times (steady-state). For short times, the diffusion length is small compared to the cavity radius, and in analogy to the case for 3D diffusion, the diffusional flux should effectively be 1D in nature, with $J(a) = -(D_{gb}\Delta c/\Omega\sqrt{\pi D_{gb}t})$. The filling fraction is obtained after surface and time integration of the flux. The dominant time exponent for the filling fraction ($f \propto t^v$) for isotropic 2D diffusion is $v = 1$ in the later stages of filling, as can be seen from equation 4.15. For short times $v = 0.5$ is expected. In practical cases $0.5 \leq v \leq 1$ can be found. The cross-over between the solution for short and long times is expected to take place when $2\sqrt{D_{gb}t} \approx a$, which leads to $\tau \approx (1/4)(D_v/D_{gb})$.

The flux rapidly stabilizes to a constant value, which is similar to the case of 3D symmetric cavity filling. This solution is similar to the simplified solution of Herring [12], describing the axial diffusional growth of creep cavities, which means that like the 3D case, the time exponent for the diffusional flux tends to $v = 1$ for large times.

4.6.3. 1D solute transport
In planar geometry (1D), the diffusion equation corresponds to;

$$\frac{\partial c}{\partial t} = D_V\left(\frac{\partial^2 c}{\partial r^2}\right).$$

(4.16)

The well-known concentration profile, for boundary conditions $c(r = a) = c_1$ and $c(r = \lambda) = c_0$, is of the form

$$\frac{c_0 - c(r,t)}{c_0 - c_1} = \mathrm{erfc}\left(\frac{r - a}{2\sqrt{D_V t}}\right).$$

(4.17)

The flux at the edge of the creep cavity is now

$$J(a) = -\frac{D_V \Delta c}{\Omega}\frac{1}{\sqrt{\pi D_V t}} = -\frac{D_V \Delta c}{a\Omega}\frac{1}{\sqrt{\pi\tau}}.$$

(4.18)

The filling fraction is obtained after surface and time integration of the flux. The time exponent for the filling fraction ($f \propto t^v$) for 1D diffusion is always $v = 0.5$.

REFERENCES

[1] C. D. Versteylen, N. K. Szymański, M. H. Sluiter, and N. H. van Dijk, *Finite element modelling of creep cavity filling by solute diffusion,* Philos. Mag. **98**, 864 (2018).

[2] F. Abe, T.-U. Kern, and R. Viswanathan, *Woodhead Publ.* (Boca Raton, 2008).

[3] K. Maruyama, K. Sawada, and J. Koike, *Strengthening mechanisms of creep resistant tempered martensitic steel,* ISIJ Int. **41**, 641 (2001).

[4] K. Laha, J. Kyono, S. Kishimoto, and N. Shinya, *Beneficial effect of B segregation on creep cavitation in a type 347 austenitic stainless steel,* Scr. Mater. **52**, 675 (2005).

[5] N. Shinya, *Self Healing of Mechanical Damage in Metallic Materials,* Adv. Sci. Technol. **54**, 152 (2008).

[6] E. G. Karpov, M. V. Grankin, M. Liu, and M. Ariyan, *Characterization of precipitative self-healing materials by mechanokinetic modeling approach,* J. Mech. Phys. Solids **60**, 250 (2012).

[7] S. Zhang, C. Kwakernaak, W. G. Sloof, E. Brück, S. van der Zwaag, and N. H. Van Dijk, *Self healing of creep damage by gold precipitation in iron alloys,* Adv. Eng. Mater. **17**, 598 (2015).

[8] S. Zhang, C. Kwakernaak, F. D. Tichelaar, W. G. Sloof, M. Kuzmina, M. Herbig, D. Raabe, E. Brück, S. van der Zwaag, and N. H. van Dijk, *Autonomous repair mechanism of creep damage in Fe-Au and Fe-Au-B-N alloys,* Metall. Mater. Trans. A **46**, 5656 (2015).

[9] S. Zhang, H. Fang, M. E. Gramsma, C. Kwakernaak, W. G. Sloof, F. Tichelaar, M. Kuzmina, M. Herbig, D. Raabe, E. Brück, S. van der Zwaag, and N. H. van Dijk, *Autonomous filling of grain-boundary cavities during creep loading in Fe-Mo alloys,* Metall. Mater. Trans. A **47**, 4831 (2016).

[10] H. Fang, C. D. Versteylen, S. Zhang, Y. Yang, P. Cloetens, D. Ngan-Tillard, E. Brück, S. van der Zwaag, and N. H. van Dijk, *Autonomous filling of creep cavities in Fe-Au alloys studied by synchrotron X-ray nano-tomography,* Acta Mater. **121**, 352 (2016).

[11] W. W. Sun, H. Fang, N. H. van Dijk, S. van der Zwaag, and C. R. Hutchinson, *Linking surface precipitation in Fe-Au alloys to its self-healing potential during creep loading,* Metall. Mater. Trans. A **48**, 2109 (2017).

[12] C. Herring, *Diffusional viscosity of a polycrystalline solid,* J. Appl. Phys. **21**, 437 (1950).

[13] D. Hull and D. E. Rimmer, *The growth of grain-boundary voids under stress,* Philos. Mag. **4**, 673 (1959).

4

[14] A. Needleman and J. R. Rice, *Plastic Creep Flow Effects in the Diffusive Cavitation of Grain Boundaries,* Acta Metall. **28**, 1315 (1980).

[15] E. van der Giessen, M. W. D. van der Burg, A. Needleman, and V. Tvergaard, *Void growth due to creep and grain boundary diffusion at high triaxialities,* J. Mech. Phys. Solids **43**, 123 (1995).

[16] C. Zener, *Theory of growth of spherical precipitates from solid solution,* J. Appl. Phys. **20**, 950 (1949).

[17] H. Aaron and H. I. Aaronson, *Growth of grain boundary precipitates in Al-4% Cu by interfacial diffusion,* Acta Metall. **16**, 789 (1968).

[18] H. B. Aaron and G. R. Kotler, *Second phase dissolution,* Metall. Trans. **2**, 393 (1971).

[19] H. I. Aaronson, M. Enomoto, and J. K. Lee, *Mechanism of diffusional phase transformations in metals and alloys* (CRC Press, Boca Raton, 2010).

[20] A. van den Berg, G. Segal, and D. A. Yuen, *SEPRAN: A versatile finite-element package for a wide variety of problems in geosciences,* J. Earth Sci. **26**, 89 (2015).

[21] G. Segal, *http://ta.twi.tudelft.nl/sepran/sepran.html,* (2015).

[22] R. Raj and M. F. Ashby, *Intergranular fracture at elevated temperature,* Acta Metall. **23**, 653 (1975).

[23] M. E. Glicksman, *Diffusion in Solids: Field Theory, Solid-State Principles, and Applications* (John Wiley & Sons, Inc., New York, NY, 1999) pp. 136–142.

[24] H. B. Aaron, D. Fainstein, and G. R. Kotler, *Diffusion-limited phase transformations: A comparison and critical evaluation of the mathematical approximations,* J. Appl. Phys. **41**, 4404 (1970).

[25] A. D. Brailsford and H. B. Aaron, *Growth of grain-boundary precipitates,* J. Appl. Phys. **40**, 1702 (1969).

[26] G. Yi, M. L. Free, Y. Zhu, and A. T. Derrick, *Capillarity effect controlled precipitate growth at the grain boundary of long-term aging Al 5083 alloy,* Metall. Mater. Trans. A **45**, 4851 (2014).

[27] A. Isaac, K. Dzieciol, F. Sket, and A. Borbely, *In-situ microtomographic characterization of single-cavity growth during high-temperature creep of leaded brass,* Metall. Mater. Trans. A Phys. Metall. Mater. Sci. **42**, 3022 (2011).

[28] J. Crank, *Oxford Univ. Press*, 2nd ed. (Oxford University Press, 1975) pp. 71–84.

5

A NEW DESIGN PRINCIPLE FOR CREEP-RESISTANT MATERIALS

If you try and take a cat apart to see how it works,
the first thing you have on your hands is a non-working cat.

Douglas Adams

Achieving higher energy efficiency and reduced carbon dioxide emission requires development of materials that retain strength at high temperature. To further improve current creep resistant materials new design principles are needed. The new design principle engineers a vacancy flux in order to limit creep void growth by selective precipitation and simultaneously counters bulk deformation by preventing grain boundary relaxation. Selective precipitation can produce a countercurrent of vacancies away from creep cavities and thereby prevent cavity growth and grain boundary relaxation leading to significantly extended service life of newly developed creep-resistant steels. The key to determining the efficiency of the autonomous repair lies in the relative diffusivity and the available solute inside the host matrix.

Creep damage prevents reliable and low-cost application of high-temperature steam turbines, which are an important link in the chain of high-efficiency energy conversion technologies. Creep strain in metals is attributed to grain-boundary sliding and bulk deformation. The approaches used to increase creep life are based on the formation of small and stable precipitates on grain boundaries and in the bulk, to delay grain-boundary sliding and bulk deformation, and by retaining up to high temperature high dislocation densities [1, 2]. The failure mode is in many cases due to the growth and coalescence of creep cavities on grain boundaries [3]. A costly approach to avoid such failure modes involves eliminating grain boundaries altogether by forming structural components out of a favorably-oriented single crystal [2].

Here we will focus on a new, potentially more practical, method. The growth of creep voids is controlled by the flux of vacancies [4, 5]. The vacancies originate from the grain boundaries, rather than from the bulk, because the vacancy formation energy is lower at the grain boundary than in the bulk. Ishida and McLean [6] discovered that the free volume required to form vacancies on the grain boundary originates from the ingress of dislocations. Dislocations are defects that destroy perfect packing and therefore are associated with excess volume. When dislocations annihilate in grain boundaries they create strain and deposit excess volume. It has been shown that for low-angle grain boundaries [7] and for twins [8], the boundaries can get more disordered, and therefore become higher energy boundaries due to the ingress of dislocations. These disordered grain boundaries provide a better barrier for the ingress of new dislocations in the form of a back stress. Eventually, the grain boundary relaxes the accumulated strain under the expulsion of excess volume, in the form of vacancies [9, 10]. Following the arguments by Hull and Rimmer [5], we propose that the vacancies then drain to creep cavities on the grain boundary, causing these cavities to grow and ultimately coalesce.

The growth of creep cavities can be countered by creating a vacancy flux in the opposite direction, away from the cavities. The Darken analysis gives a recipe for creating such a flux: utilize a substitutional solute with a (i) strong driving force to go from the bulk towards the cavity and (ii) with high solute mobility compared to the host species. As the flux is the product of mobility, activity and chemical potential gradient, it is clear that the difference of solute chemical potential in the bulk and in the cavity should be as large as possible. This can be achieved by maximizing the chemical potential in the bulk by solute supersaturation, and by selecting a solute that forms highly stable precipitates in the cavity. Experimentally it has been observed that the presence of supersaturated solute in the bulk can result in an autonomous filling of creep cavities [11–14]. The solute that segregates at the cavity surfaces is found to be transported along the grain boundaries [11] and form precipitates at free surfaces and inside cavities [13]. The fluxes of solute atoms and vacancies are illustrated in figure 5.1. As the vacancy counter flux reduces the net flux of vacancies to the creep cavities the growth rate of the cavities is slowed down. This extends the life-time if cavity coalescence is the failure mechanism. The reduced drainage of vacancies has other consequences as well.

When vacancies are not expelled by the grain boundary, the strain relaxation cannot proceed. The highly strained grain-boundary region provides a back stress for the ingress of dislocations as was shown in various computer simulations [15, 16], see figure 5.2.
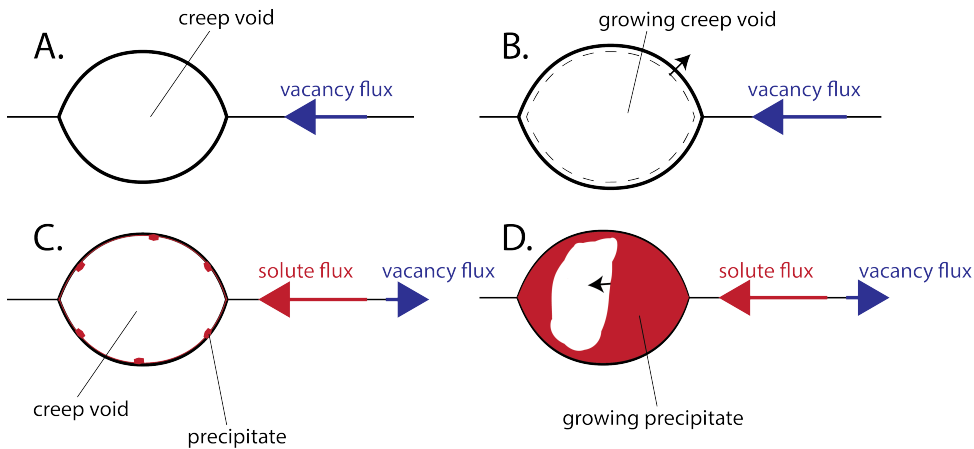
Figure 5.1: Schematic representation of creep cavity growth and precipitation inside a creep cavity. (A) vacancy flux towards creep cavity. (B) creep cavity growth is controlled by the vacancy flux. (C) segregation of solute at the creep cavity surface induces a vacancy flux in opposite direction. (D) the solute flux causes filling of the creep cavity and retention of vacancies at grain boundaries.

Just as in the Hall-Petch effect, such a back stress retards further dislocation movement, which manifests itself as a reduction of the strain rate. Apart from a more effective barrier for dislocation movement, this failure to dissipate dislocations, leads to a higher dislocation density in the material, which is in concurrence with the observations by Zhang and coworkers [12].

The strain rate and time to failure under creep are found to be inversely proportional in agreement with the Monkman-Grant relation. The reduction in strain rate, therefore increases the creep life time. The reduction in cavity growth rate and the reduction in strain rate can thus be achieved by the selective precipitation at the creep cavities by a substitutional solute from the bulk. Solute elements that are likely to act in such a manner in bcc-iron should: (i) display a strong tendency to accumulate, and ultimately precipitate, selectively at a creep cavity surface (ii) be an element with a retrograde solubility line in the phase diagram with iron, such that it can be in supersaturation at creep temperatures, and (iii) be sufficiently mobile in iron, such that the flux of the solute exceeds the flux of the iron host. At first sight this list of requirements appears difficult to fulfill. Diffusivities of substitutional solutes are generally close to those of iron self-diffusion, while higher diffusivities often occur for elements with very low solubility [17]. However, iron has a rather high surface energy [18], so that there are many elemental solutes in iron that segregate to its free surfaces.

In the context of creep alloys, autonomous repair has been investigated for austenitic stainless steels [19, 20] and for ferritic Fe-Cu, Fe-Au [11–14], and Fe-Mo [21] alloys. In these studies solute elements are brought in a supersaturated state and subsequently made to precipitate during creep. It was found that up to 80% of the creep cavities could be filled by selective precipitation [12]. This autonomous repair mechanism has been demonstrated to significantly extend the creep lifetime. Not all precipitating solutes are equally effective, however. In bcc iron a fixed 1 atomic percent oversaturated gold
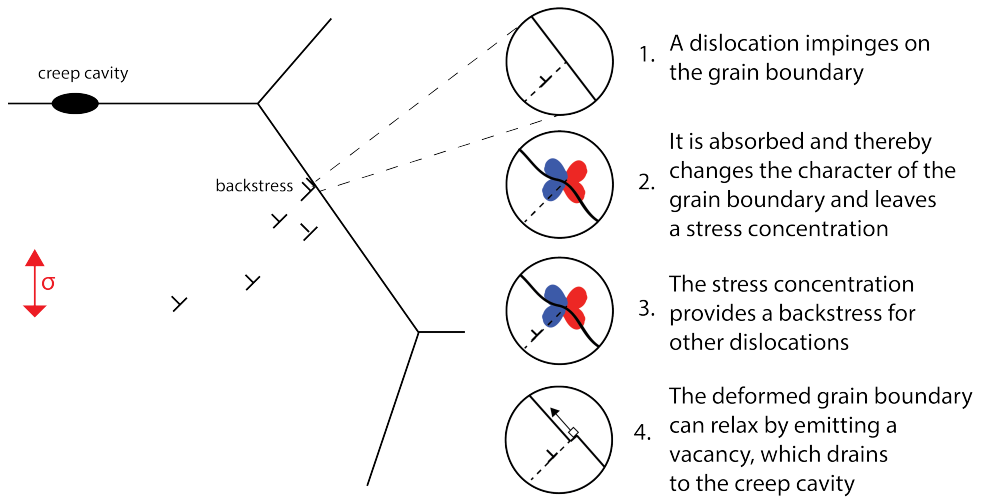
Figure 5.2: Schematic microstructure evolution during creep. A creep cavity on a grain boundary under stress grows by diffusional flux of vacancies. The vacancies are formed at the grain boundaries at locations where dislocations impinge. Dislocations travel through a grain and annihilate at the grain boundaries, where they leave a stress concentration. This prevents the ingress of more dislocation, until the grain boundary can relax by emitting vacancies. Thus vacancy formation at grain boundaries and bulk strain rate are coupled.

retards creep much more than copper [12]. The high effectiveness of gold cannot be explained by the mechanical properties of the gold-rich precipitates because these are rather soft at elevated creep temperatures. Gold is, however, more effective at generating a vacancy counter flux. It has a lower surface energy than copper, especially in relation to iron [18], and it has a higher mobility in iron as well [17].

In aluminum alloys the vacancy counter flux mechanism appears to have been observed already. Yousefiani and coworkers [22] showed that creep strain-rates in 7075 aluminum alloys can be reduced by almost an order of magnitude by overheating the alloy prior to exposure to creep. During the overheating treatment precipitates with zinc and magnesium are completely dissolved. Solutes such as zinc and magnesium have significantly lower surface energies than aluminum and thus can be expected to segregate towards free surfaces and locally form precipitates. Indeed, during creep the overheated material forms large precipitates on the strained grain boundaries where cavities are expected, just as was seen in Fe-Au alloys [11–14]. Whereas the conventionally heat treated material fails through cavity coalescence and grain-boundary sliding, the overheated material fails through constrained cavitation and bulk deformation - just as one would expect on the basis of the counter flux description. In aluminum alloys a similar effect has been observed, with magnesium segregation towards cavities [23].

The principle of vacancy counter-flux does not necessarily interfere with the currently common design principle of inter- and intragranular precipitation. The formation of gold-rich precipitates in cavities does not interfere with the precipitation of various carbides and borides because gold generally is hardly soluble in these phases. Therefore, it

can be used in conjunction with conventional design principles to further enhance the performance of industrial creep-resistant alloys. Recent results in Fe-Mo alloys indicate that the proposed mechanism is not limited to Fe Au but is expected to be generic for metallic alloys with suitable solutes.

5

REFERENCES

[1] F. Abe, T.-U. Kern, and R. Viswanathan, *Woodhead Publ.* (Boca Raton, 2008).

[2] T. M. Pollock and S. Tin, *Nickel-Based Superalloys for Advanced Turbine Engines: Chemistry, Microstructure and Properties,* J. Propuls. Power **22**, 361 (2006).

[3] M. F. Ashby, C. Gandhi, and D. M. Taplin, *Overview No. 3 Fracture-mechanism maps and their construction for f.c.c. metals and alloys,* Acta Metall. **27**, 699 (1979).

[4] C. Herring, *Diffusional viscosity of a polycrystalline solid,* J. Appl. Phys. **21**, 437 (1950).

[5] D. Hull and D. E. Rimmer, *The growth of grain-boundary voids under stress,* Philos. Mag. **4**, 673 (1959).

[6] Y. Ishida and D. McLean, *The formation and growth of cavities in creep,* Met. Sci. **38**, 171 (1967).

[7] N. R. Tao, Z. B. Wang, W. P. Tong, M. L. Sui, J. Lu, and K. Lu, *An investigation of surface nanocrystallization mechanism in Fe induced by surface mechanical attrition treatment,* Acta Mater. **50**, 4603 (2002).

[8] F. Zhang, X. Feng, Z. Yang, J. Kang, and T. Wang, *Dislocation-Twin Boundary Interactions Induced Nanocrystalline via SPD Processing in Bulk Metals,* Sci. Rep. **5**, 8981 (2015).

[9] M. Upmanyu, D. Srolovitz, L. Shvindlerman, and G. Gottstein, *Vacancy generation during grain boundary migration,* Interface Sci. **6**, 287 (1998).

[10] R. J. Dikken, *Friction and plasticity of micro- and nano-scale metal contacts*, Ph.D. thesis, Technische Universiteit Delft (2017).

[11] S. Zhang, C. Kwakernaak, F. D. Tichelaar, W. G. Sloof, M. Kuzmina, M. Herbig, D. Raabe, E. Brück, S. van der Zwaag, and N. H. van Dijk, *Autonomous repair mechanism of creep damage in Fe-Au and Fe-Au-B-N alloys,* Metall. Mater. Trans. A **46**, 5656 (2015).

[12] S. Zhang, C. Kwakernaak, W. G. Sloof, E. Brück, S. van der Zwaag, and N. H. Van Dijk, *Self healing of creep damage by gold precipitation in iron alloys,* Adv. Eng. Mater. **17**, 598 (2015).

[13] H. Fang, C. D. Versteylen, S. Zhang, Y. Yang, P. Cloetens, D. Ngan-Tillard, E. Brück, S. van der Zwaag, and N. H. van Dijk, *Autonomous filling of creep cavities in Fe-Au alloys studied by synchrotron X-ray nano-tomography,* Acta Mater. **121**, 352 (2016).

[14] W. W. Sun, H. Fang, N. H. van Dijk, S. van der Zwaag, and C. R. Hutchinson, *Linking surface precipitation in Fe-Au alloys to its self-healing potential during creep loading,* Metall. Mater. Trans. A **48**, 2109 (2017).

5

[15] A. Elzas and B. Thijsse, *Dislocation impacts on iron/precipitate interfaces under shear loading,* Model. Simul. Mater. Sci. Eng. **24**, 085006 (2016).

[16] R. J. Dikken, B. J. Thijsse, and L. Nicola, *Impingement of edge dislocations on atomically rough contacts,* Comput. Mater. Sci. **128**, 310 (2017).

[17] C. D. Versteylen, N. H. van Dijk, and M. H. F. Sluiter, *First-principles analysis of solute diffusion in dilute bcc Fe-X alloys,* Phys. Rev. B **96**, 094105 (2017).

[18] R. Tran, Z. Xu, B. Radhakrishnan, D. Winston, W. Sun, K. A. Persson, and S. Ping Ong, *Data Descriptor: Surface energies of elemental crystals,* Sci. Data **3**, 160080 (2016).

[19] K. Laha, J. Kyono, S. Kishimoto, and N. Shinya, *Beneficial effect of B segregation on creep cavitation in a type 347 austenitic stainless steel,* Scr. Mater. **52**, 675 (2005).

[20] K. Laha, J. Kyono, and N. Shinya, *An advanced creep cavitation resistance Cu-containing 18Cr-12Ni-Nb austenitic stainless steel,* Scr. Mater. **56**, 915 (2007).

[21] S. Zhang, H. Fang, M. E. Gramsma, C. Kwakernaak, W. G. Sloof, F. Tichelaar, M. Kuzmina, M. Herbig, D. Raabe, E. Brück, S. van der Zwaag, and N. H. van Dijk, *Autonomous filling of grain-boundary cavities during creep loading in Fe-Mo alloys,* Metall. Mater. Trans. A **47**, 4831 (2016).

[22] A. Yousefiani, F. A. Mohamed, and J. C. Earthman, *Creep rupture mechanisms in annealed and overheated 7075 Al under multiaxial stress states,* Metall. Mater. Trans. A **31**, 2807 (2000).

[23] M. Song, K. Du, C. Wang, S. Wen, H. Huang, Z. Nie, and H. Ye, *Geometric and chemical composition effects on healing kinetics of voids in Mg-bearing Al alloys,* Metall. Mater. Trans. A **47**, 2410 (2016).

5

6

A SIMPLE MODEL FOR CREEP-RESISTANT METALS

Off course, geometry is the ultimate abstraction.

stranger in a London supermarket

A self-consistent model is presented to predict the creep cavity growth and strain rates in metals from the perspective of self-healing. The creep cavity growth rate is found to be intricately linked to the strain rate. The self-healing process causes precipitates to grow inside creep cavities. Due to the Kirkendall effect, vacancies are transported away from the creep cavity during this selective precipitation which impedes their growth. The critical stress for self-healing can be derived and an analysis is made of the efficiency of self-healing elements in binary Fe-Cu, Fe-Au, Fe-Mo, and Fe-W alloys. Fe-Au is found to be the most efficient self-healing alloy. Fe-Mo and Fe-W alloys provide good alternatives that have the potential to be employed up to higher temperatures.

6.1. INTRODUCTION

High-temperature deformation and failure mechanisms in metals have attracted considerable academic and industrial attention since the 1950s [1–4]. The materials' response can be complicated since many processes are at play simultaneously, such as; dislocation glide and climb, jog and wall formation, vacancy formation and annihilation, and creep-cavity nucleation and growth. A key damage mechanism is the nucleation of creep cavities located at the grain boundaries oriented perpendicular to the applied load at elevated temperatures [5]. After nucleation, these cavities start to grow by the diffusion of vacancies [6] and eventually they coalesce with neighboring cavities formed on the same grain boundary. After coalescence a rapid damage growth is observed, resulting in macroscopic failure. In this failure mechanism the creep time is inversely proportional to the creep strain rate of the alloy. This behavior is known as the Monkman-Grant relation. Linking the strain rate to the cavity growth has been a key subject of interest [7–16].

Recently, the concept of self-healing has been explored to extend the lifetime of structural and functional man-made materials [17]. Autonomous repair of creep damage has been investigated by Laha and coworkers for stainless steels [18, 19] and by Zhang and coworkers for ferritic Fe-Au [20–23] and Fe-Mo alloys [24]. In these studies solute elements are brought in a supersaturated state and thereby show a strong tendency to segregate. It was found that up to 80% of the creep damage could be filled by selective precipitation growth at creep cavity surfaces [21]. This autonomous repair mechanism is demonstrated to significantly extend the lifetime, and thereby lead to a more creep-resistant metal. Where creep failure is largely controlled by the diffusion of vacancies, the self-healing of creep damage largely relies on the diffusion of supersaturated solute. This means that self-healing of creep damage requires a new theoretical framework to describe creep damage and healing, based on a delicate balance between the simultaneous diffusion of host atoms (vacancies) and solute atoms. The aim of this work is to link the transport mechanisms of excess vacancies, supersaturated solute and the macroscopic strain rate in creep-healing high-temperature metal alloys. A model is developed, based on the transport of vacancies between bulk, grain boundary, and creep cavities. The creep behaviour of the extensively studied binary Fe-Au(1 at.%) alloy [20–22] is used as an example to optimise the temperature and stress dependence for the healing of creep damage. The healing potential of Fe-Au alloys is compared to that of Fe-Cu, Fe-Mo and Fe-W alloys.

6.2. MODEL DESCRIPTION

6.2.1. CONSTRAINED GROWTH OF CREEP CAVITIES

As is shown in figure 6.1a, a creeping material generally deforms in three stages; an initial stage when load and temperature are first applied (stage I), a steady-state constant creep rate (stage II), and finally an accelerated creep rate until failure, (stage III). Under the influence of stress, creep cavities form at grain boundaries oriented perpendicular to the stress direction, as visualized in figure 6.1b.

The damage formation in creeping metals was first described by Hull & Rimmer [6]. In this model, creep cavities form on grain boundaries and grow through the diffusional
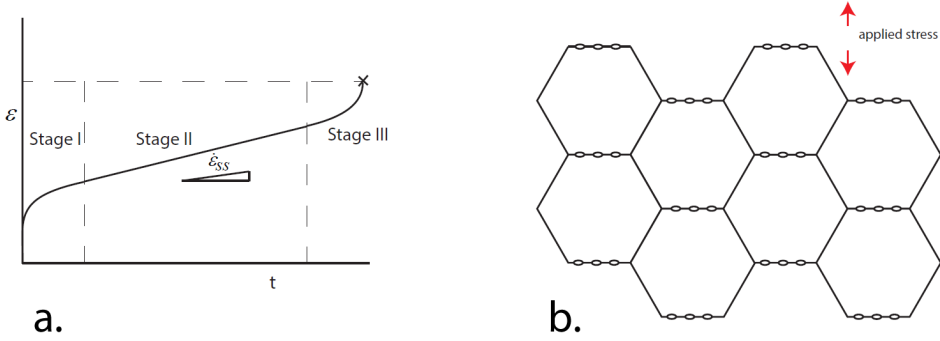
Figure 6.1: a. Strain-time curve of a metal under creep conditions. In stage II a steady-state strain rate ($\dot{\varepsilon}_{ss}$) is observed. b. Formation of creep cavities at grain boundaries oriented perpendicular to the applied stress direction.
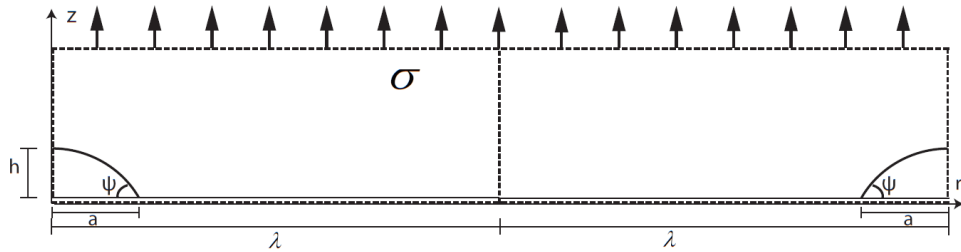

Figure 6.2: *Creep cavity of width 2a on a grain boundary in a metal under a stress σ, where the distance 2λ indicates the distance to the next creep cavity. The creep cavities are lens-shaped with a height h, and an opening angle ψ.*

flux of vacancies, which is driven by a gradient in chemical potential of a vacancy between a location far away from the creep cavity and at the cavity surface. Following Herring [1] and Hull & Rimmer [6], the gradient in chemical potential $\nabla\mu$ can be approximated by;

$$\nabla\mu \approx \frac{\sigma\Omega}{\lambda}. \tag{6.1}$$

The stress σ causes an increase in the chemical potential of a vacancy with volume Ω. At the edge of the creep cavity this stress is zero and far away from the cavity, at distance λ, it is equal to the applied stress. This stress dependence results in a gradient in vacancy concentration and a flux of vacancies towards the surface of the creep cavity. The cavity grows due to a diffusional vacancy flux over grain boundaries (vacancies are indicated by the symbol □);

$$J_\square = -\frac{1}{\Omega} \frac{D_\square^{gb} c_\square^{gb}}{k_B T} \nabla\mu \approx -\frac{D_\square^{gb} c_\square^{gb}}{k_B T} \frac{\sigma}{\lambda}, \tag{6.2}$$

where k_B is Boltzmann's constant and T is the temperature. The flux of vacancies towards the creep cavity $J_\square$, is a function of the vacancy diffusivity over the grain boundary $D_\square^{gb}$ (which is much faster than bulk diffusivity $D_\square^{bulk}$), and a function of the equilibrium vacancy concentration at the grain boundary, $c_\square^{gb}$ (in atom fraction). This approach of Hull & Rimmer [6] provides a diffusional flux, driven only by applied stress (they introduced a vacancy density $C_\square^{gb} = c_\square^{gb}/\Omega$). This flux contributes to the growth of the creep cavity by adding a volume Ω for each added vacancy. The creep cavity surface connecting the grain boundary is equal to $S = 2\pi a\delta$, where a is half the opening width of the creep cavity and δ is the grain boundary thickness.

The void growth rate $\dot{V} = J_\square S\Omega$ can now be described as;

$$\dot{V} = \frac{D_\square^{gb} c_\square^{gb}}{k_B T} \frac{\sigma}{\lambda} 2\pi a\delta\Omega. \tag{6.3}$$

During typical operating conditions, creep deformation is dominated by steady-state creep; also known as stage II creep (see figure 6.1). For these conditions, the time to failure t_f depends directly on the steady-state strain rate $\dot{\epsilon}_{ss}$. This is known as the Monkman-Grant relation [25]:

$$\dot{\epsilon}_{ss} t_f = C_{MG}, \tag{6.4}$$

where C_{MG} is the Monkman-Grant constant. At first glance equations 6.3 and 6.4 seem to contradict each other. Since $\dot{\epsilon}_{ss}$, is normally related to the bulk diffusivity and the void growth rate $\dot{V}$ to the grain boundary diffusivity.

The description of creep has been divided in microscopic damage descriptions [6, 26], and the macroscopic strain-rate description; i.e. the Monkman-Grant relationship [4, 25]. In order to explain the relation between this large-scale deformation model and the small scale damage model, the principle of constrained creep cavity growth was proposed. This constrained growth was first introduced by Ishida & McLean [7] to explain discrepancies between theoretical unconstrained cavity growth and experimentally observed creep curves. In their approach a grain boundary requires the ingress of a dislocation to form a vacancy. Thereby the steady-state creep strain rate $\dot{\epsilon}_{ss}$ is thereby coupled to the volumetric growth rate $\dot{V}$ of a creep cavity [4].

The link between the steady-state strain rate $\dot{\epsilon}_{ss}$ and the cavity growth rate $\dot{V}$ leads to the Monkman-Grant relation. Dyson [8] and Riedel [4] showed that in many cases the creep cavity growth rate will be limited by the strain rate of the material;

$$\dot{\epsilon}_{ss} = \frac{\dot{V}}{4\lambda^2 d}, \tag{6.5}$$

where d is the grain size, and $4\lambda^2$ is the grain-boundary surface area assigned to a single cavity.

Building on the ideas of Dyson, Rice [14] formulated a model where the rate of opening for creep cavities is a function of the strain rate by combining both effects. This

was worked out by Needleman & Rice [15] and Budiansky [27]. Van der Giessen and coworkers [16] analyzed this effect for different applied load combinations. However, these studies do not treat the case where the strain-rate is a limiting factor on the diffusional growth rate of a cavity, which is treated here. Cocks & Ashby [28] reviewed all different creep regimes and provided maps of the damage rate as a function of applied stress. This description can provide good agreement with experimental data [4] for conventional creep, but it does not accurately describe self-healing systems. It also does not provide an explanation why the strain rate and void growth rates are linked.

We follow the ideas of Ishida and McLean and assume that the ingress of a dislocation to the grain boundary can cause the formation of a vacancy, which in turn contributes to the growth of a creep cavity. If these vacancies are not formed continuously, the void growth rate would come to a stop. Thereby the growth rate of creep cavities and the creep strain rate are linked through the movement of dislocations, where the rate limiting step is the dislocation climb in the bulk (leading to an activation energy similar to the self-diffusion activation energy in the bulk).

The assumptions used in the proposed model are:
(i) creep cavities form at grain boundaries perpendicular to the loading direction.
(ii) Cavity growth rate and the steady-state strain rate are proportional.
(iii) Continuous formation of vacancies is required in order to maintain the cavity growth rate, these vacancies form predominantly as a result of dislocation ingress at grain boundaries. This means that the vacancy formation is the rate-limiting step for the diffusional growth of creep cavities.
(iv) The ingress of dislocation to a grain boundary can cause excess volume and stress concentrations to accumulate in the grain boundary. The relaxation of the excess volume and the stress concentration on the grain boundary can happen by draining vacancies from the grain boundary to the creep cavities.

6.2.2. Dislocation movement and vacancy transport

In the present models that describe creep cavity growth[6], the implicit assumption is that the vacancy concentration remains at equilibrium values at a characteristic distance from the creep cavity at all times. It is not a priori obvious that this should be true. In fact the concepts of Ishida and coworkers [7, 29] that a grain boundary requires the ingress of dislocations in order to be able to slide, can be combined with the proposal of Dyson [8, 30] that grain-boundary sliding is a constraint for the growth of creep cavities.

This means that the movement of dislocations, which controls the strain rate of metal that deforms under creep conditions, is also the rate-determining factor for cavity growth. This explains the Monkman-Grant relationship: the strain rate determines the time to failure by the formation of vacancies on the grain boundaries close in the diffusion zone of the creep cavities.

When a dislocation network has developed and the steady-state strain rate causes a certain number of dislocations per second to reach a grain boundary, each of them caries an open volume [31], of which part is transfered to the grain boundary when the dislocation impinges. The vacancy fraction in the grain boundary $c_\square^{gb}$ should depend on the rate at which vacancies are generated due to the influx of dislocations.

The strain rate of a metal depends on the mobile dislocation density [32] ρ_{disl}, the

climb velocity v_{cl} of a dislocation jog and the Burgers vector b, as described by the Orowan equation;

$$\dot{\epsilon} = b\rho_{disl}v_{cl}. \tag{6.6}$$

The strain rate depends on the stress through the dislocation density [33] and the climb velocity [34]. The stress-dependence of the strain rate is expressed with a power law as, $\dot{\epsilon} \propto \sigma^n$.

The stress dependence of the dislocation climb velocity [35] can be approximated by,

$$v_{cl} \approx \frac{D_{sd}f_{cl}\Omega}{b^2 k_B T}, \tag{6.7}$$

where D_{sd} is the self-diffusivity, and f_{cl} the force acting on a climbing dislocation. During stage II creep with a constant strain rate, the average collective dislocation movement is of interest for the deformation rate. The drift velocity of the dislocation network can be correlated to the individual movement of dislocations[36]. The collective climbing or gliding rate of dislocations in a dislocation network is unknown, but as an approximation the individual movement can be considered. The strain rate according to the Orowan equation (equation 6.6), can be linked to the Dyson equation (equation 6.5), in order to obtain an equation of the creep cavity growth;

$$\dot{\epsilon} = b\rho_{disl}v_{cl} = \frac{\dot{V}}{4\lambda^2 d}. \tag{6.8}$$

The creep-cavity growth rate $\dot{V}$ now depends on the influx of dislocations, and the volume associated to these dislocations. The density of dislocations transported to the grain boundary is associated to the creep void by length λ. The dislocation density is a function of the subgrain size [37], for an observed subgrain size (d_{sub}) of 1 μm in Fe-Au [20], the dislocation density $(\rho_{disl}) = 1\times10^{-12}$ m^{-2}. For Fe-Au, it was found experimentally [20–22], that at 550 °C and an applied load of 100 MPa, the strain rate ($\dot{\epsilon}$) = 2× 10^{-8} s^{-1}. The Burgers vector of bcc iron b = 2.5 Å. The climbing velocity of the collective dislocation network then (v_{cl}) = 8×10^{-11} m s^{-1}. The associated velocity of the dislocation network is approximately 1 Å/s. This value is of similar magnitude compared to the values found by Caillard for single dislocation kink movement, in the presence of solute [34].

As was discussed in the previous chapter, when a dislocation impinges on or near a grain boundary, it will provide a back stress on the following dislocations. The character of a grain boundary is altered by the absorption of a dislocation and its associated volume [38, 39]. This change in character, in the form of a stress concentration provides a repulsive barrier for the influx of the next dislocation [40]. The increase of volume in the grain boundary, leads to a more disordered structure and an excess vacancy concentration. We postulate that the relaxation of the excess volume and the stress concentration on the grain boundary can happen by draining vacancies from the grain boundary to the creep cavities. This flux of vacancies from a disordered section of grain boundary to the creep cavities, leads to a less disordered grain boundary and allows new dislocation to ingress into the grain boundary. This link of the grain deformation rate and the creep cavity growth rate causes the Monkman-Grant relation.

6.2.3. SELF-HEALING

Experimentally it has been observed that the presence of supersaturated solute can result in an autonomous filling of creep cavities and a significant extension of the creep life time [20–22]. It is found that the self-healing mechanism does not significantly affect the critical strain at rupture, but does reduce the steady-state strain rate, as schematically illustrated in figure 6.3. The solute that segregates at the free creep cavity surfaces is found to be transported along the grain boundaries from the supersaturated bulk. This flux of segregating solute competes with the vacancy flux, and thereby reduces both the cavity growth rate and the vacancy flux away from grain boundaries under stress towards the creep cavities. This process is known as the Kirkendall effect.
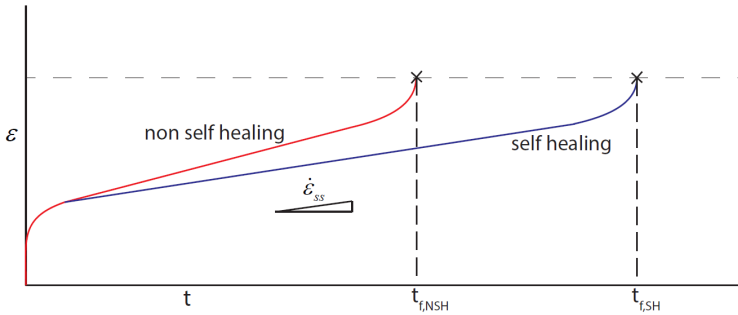
Figure 6.3: Evolution of strain with time for a non-self-healing and a self-healing metal. The non-self-healing metal has a shorter creep life time $t_{f,NSH}$, and a higher steady-state strain rate $\dot{\epsilon}_{ss}$. The time to failure is predominantly controlled by the strain rate in stage II.

6.2.4. SOLUTE TRANSPORT

After nucleation a diffusional growth of the precipitate initiates a flux of solute, driven by a chemical potential;

$$J_{sol} = -\frac{D_{sol}}{k_B T} \nabla \mu_{sol}. \tag{6.9}$$

The difference in chemical potential of solute atoms between precipitation in the bulk and on creep cavity surface, causes a preference for precipitate growth in the creep cavities. The terms playing a role are, the possibility for the precipitate to reduce the surface energy of the free surface of bulk material in the creep cavity, the possibility of reducing the surface energy of a precipitate and the reduction in stress concentration between the precipitate and the bulk material. The driving force for precipitation is then given by this chemical potential, but also by the supersaturated solute which remains in solution during service life. This is assumed to be the largest contribution to the self-healing process in metals, and it is measurable with atom probe tomography [20], the solute is then depleted from the grain boundary and neighboring bulk as a result of the diffusion towards the precipitate.
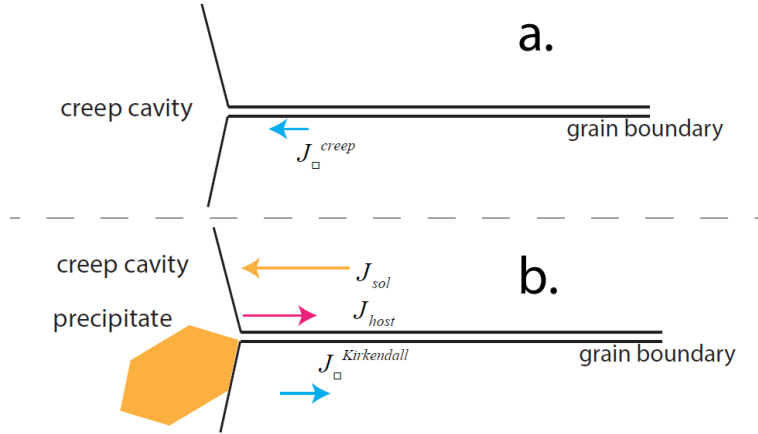
Figure 6.4: a. Schematic illustration of the vacancy transport near a creep cavity. The flux of vacancies through a grain boundary towards a creep cavity during stage II creep causes this creep cavity to grow. b. When precipitation occurs inside the creep cavity, a solute flux causes the precipitate to grow. The solute flux $\left(J_{sol}\right)$ causes a vacancy flux ($J_\square$) in the opposite direction due to the Kirkendall effect. The net vacancy flux can be zero, preventing the creep cavity to grow.

The difference in diffusivity of host and substitutional solute causes a net diffusion of vacancies in the direction opposite to the faster species. The flux balance of this process can be approximated with the following Darken equation which, in the dilute limit, can be simplified to:

$$J_{\square,out} = \frac{1}{\Omega}(D_{sol} - D_{host})\nabla c_{sol}. \tag{6.10}$$

where D_{host} is the diffusivity of the host atoms, D_{sol} is the diffusivity of the solute, and ∇c_{sol} is the concentration gradient of the solute. Assuming that the supersaturated solute Δc_{sol}^{gb} shows a concentration profile over the grain boundary with a characteristic length λ, the gradient can be approximated by $\Delta c_{sol} = \nabla c_{sol}^{gb}/\lambda$. This approximation is valid in the dilute limit, with negligible off-diagonal terms of the Onsager matrix [41, 42].

6.2.5. FLUX BALANCE AND CRITICAL STRESS

The opposite vacancy fluxes caused by the gradient in stress-induced chemical potential and by the solute gradient, result in a net vacancy flux, either towards or from the cavity. Self-healing can be achieved when,

$$J_{\square,out}^{gb} \geq J_{\square,in}^{gb}, \tag{6.11}$$

where the flux of vacancies over the grain boundary towards the creep cavity $J_{\square,in}$ has to be smaller (or equal) than the flux of vacancies in the opposite direction $J_{\square,out}$. As discussed in the appendix, the outflux of vacancies from the creep cavity is in most cases controlled by the diffusivity of solute through the bulk.

When the two fluxes are equal a critical stress can be defined below which diffusional creep can be self-healed. Combining equations 6.2, and 6.10, with $2\pi a \delta J^{gb}_{\square,out} = 8\lambda^2 J^{bulk}_{\square,out}$ (see appendix), the flux balance results in the critical stress for self-healing,

$$\sigma_{crit} = \frac{k_B T}{\Omega} \frac{4\lambda^3}{\pi a \delta l} \frac{\left(D^{bulk}_{sol} - D^{bulk}_{host}\right) \Delta c^{bulk}_{sol}}{D^{gb}_{\square} c^{gb}_{\square}}. \quad (6.12)$$

The critical stress for self-healing (σ_{crit}), depends on the solute diffusivity compared to the host diffusivity $\left(D^{bulk}_{sol} - D^{bulk}_{host}\right)$, the grain-boundary diffusivity $\left(D^{gb}_{\square}\right)$, the supersaturated solute concentration (Δc_{sol}), and vacancy concentration $\left(c^{gb}_{\square}\right)$. The length l is the diffusion length of the supersaturated solute in the bulk towards the grain boundary. The maximum distance $\left(l_{max} = \frac{\pi}{3} \frac{a^3}{\lambda^2 \Delta c_0 \Omega}\right)$ can be estimated from mass conservation (see appendix).

6.2.6. CAVITY GROWTH RATE FROM NET SOLUTE TRANSPORT
Creep cavity growth rate can be estimated from the net vacancy flux integrated over the creep void area connecting the grain boundary:

$$\dot{V} = 2\pi a \delta J^{gb}_{\square} \Omega. \quad (6.13)$$

The rate limiting factor for the void growth is the formation of vacancies, which is linked to the strain rate. The solute precipitation in the cavity is quickly limited by the bulk diffusional flux to the area surrounding the creep cavity $\left(4\lambda^2\right)$, see Appendix. For stage II creep where the supersaturated solute is transported exclusively to the creep cavities, it is possible to write the constrained cavity growth rate as;

$$\dot{V} = 2\pi a \delta \frac{D^{gb}_{\square} c^{gb}_{\square}}{k_B T} \frac{\Omega \sigma}{\lambda} - 8\lambda^2 \left(D^{bulk}_{sol} - D^{bulk}_{host}\right) \frac{\Delta c^{bulk}_{sol}}{l}. \quad (6.14)$$

The depletion of supersaturated solute from the bulk close to the grain boundaries is clearly observed by Zhang and coworkers [20]. This depleted zone points to a diffusion-controlled process. This proves that grain-boundary sliding is not rate-limiting to the deformation.

Using equation 6.8, the strain rate of self-healing creep steels can be formulated as:

$$\dot{\epsilon}_{ss} = \frac{\pi a \delta}{2\lambda^2 d} \frac{D^{gb}_{\square} c^{gb}_{\square}}{k_B T} \frac{\Omega \sigma}{\lambda} - \frac{2}{d} \left(D^{bulk}_{sol} - D^{bulk}_{host}\right) \frac{\Delta c^{bulk}_{sol}}{l} \quad (6.15)$$

6.3. MODEL PREDICTIONS
The predictions of this model are now compared to the experimental data of Fe-1at.%Cu and Fe-1at.%Au alloys [20–22]. The solubility of copper in bcc-iron is obtained from Chen and co-workers [43], the solubility of gold in bcc-iron from Okamota and co-workers [44], the molybdenum solubility [45], and tungsten solubility from Landolt-Börnstein [46]. The relevant part of the phase diagram (between 700 and 1400 K, and between

0 and 4 at.% atom fraction of impurity) is presented in figure 6.5 for Fe-Cu, Fe-Au, Fe-Mo, and Fe-W binary alloys.
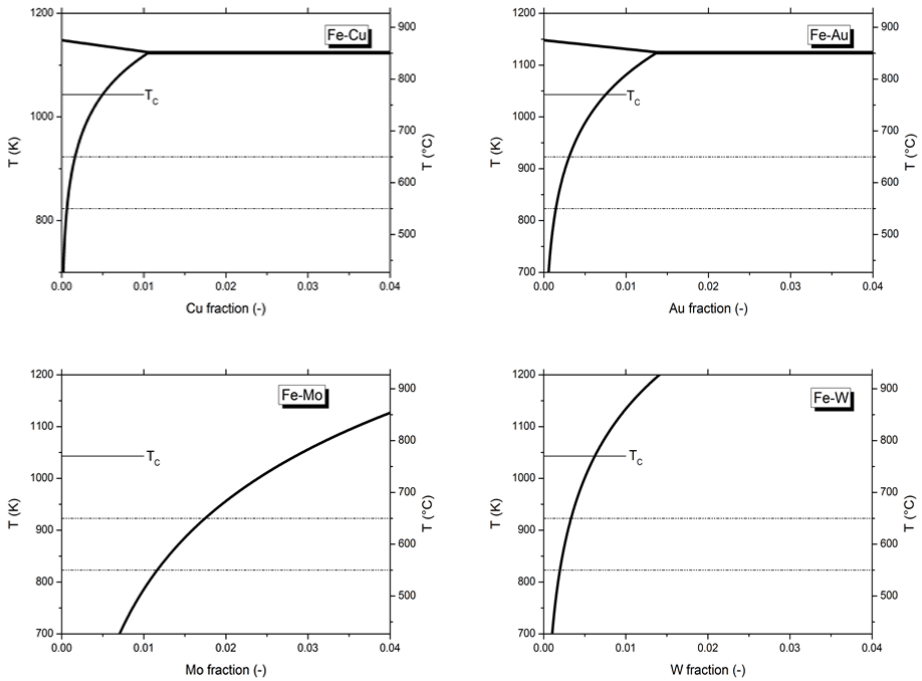

Figure 6.5: Phase diagrams for Fe-Cu, Fe-Au, Fe-Mo, and Fe-W binary alloys. With the creep temperatures 550 °C and 650 °C indicated as dashed lines. The magnetic Curie temperature (T_C) is indicated for reference. All fraction indicated in the figure are in atom%.

The grain-boundary self-diffusivity of iron was measured over a wide temperature range [47]. The grain-boundary vacancy formation enthalpy $\left(\Delta H^{gb}_{\Box,f}\right)$ is unknown, but a reasonable approximation is to assume the vacancy formation enthalpy at the grain boundary to be 50% of the activation energy for diffusion. In bcc iron there is a magnetic effect on the diffusivity, which is represented by the factor $\left(\alpha^{gb}\right)$ and the spontaneous magnetisation s. The bulk diffusivities and the influences of magnetic ordering on their activation energy for the substitutional elements used in bcc iron are obtained from the manuscript of Versteylen and coworkers [48, and references therein].

The diffusivity parameters, the vacancy concentrations, the volume of a vacancy, the thickness of a grain boundary, the considered creep cavity radius and spacing, and the applied stress that are used as modelling parameters to obtain the critical stresses for self-healing and the efficiency for self-healing are gathered in table 6.1. These model parameters are used to estimate the critical stress for self-healing of diffusional creep damage.

The critical stress was calculated for Fe-Au, Fe-Cu, Fe-Mo, and Fe-W alloys for

Table 6.1: Model parameters for self-healing creep steel, for Fe-Au, Fe-Cu, Fe-Mo, and Fe-W alloys.

variable	value	unit	reference
$Q_\square^{gb}$	0.58	eV	[47]
$\delta D_{0,\square}^{gb}$	6.35	10^{-15} m^{3}s^{-1}	[47]
α^{gb}	1.28	-	[47]
Q_{Fe}^{bulk}	2.83	eV	[48]
$D_{0,Fe}^{bulk}$	0.35	10^{-4} m^{2}s^{-1}	[48]
α_{Fe}^{bulk}	0.16	-	[48]
Q_{Au}^{bulk}	2.37	eV	[48]
$D_{0,Au}^{bulk}$	0.68	10^{-4} m^{2}s^{-1}	[48]
α_{Au}^{bulk}	0.10	-	[48]
Q_{Cu}^{bulk}	2.58	eV	[48]
$D_{0,Cu}^{bulk}$	0.27	10^{-4} m^{2}s^{-1}	[48]
α_{Cu}^{bulk}	0.10	-	[48]
Q_{Mo}^{bulk}	2.65	eV	[48]
$D_{0,Mo}^{bulk}$	0.59	10^{-4} m^{2}s^{-1}	[48]
α_{Mo}^{bulk}	0.10	-	[48]
Q_{W}^{bulk}	2.70	eV	[48]
$D_{0,W}^{bulk}$	0.26	10^{-4} m^{2}s^{-1}	[48]
α_{W}^{bulk}	0.10	-	[48]
$\Delta H_{\square,form}^{gb}$	0.29	eV	-
δ	0.5	10^{-9} m	-
d	30	10^{-6} m	-
a	0.5	10^{-6} m	-
λ	5	10^{-6} m	-
Ω	11.7	10^{-30} m^3	[49]

different solute contents (figure 6.6) assuming that all supersaturated solute experiences a driving force for the selective precipitation at the creep cavity surfaces. The self-healing process in Fe-1at.%Au, is found to be functional up to relatively high stresses, due to the high diffusivity of Au in the Fe bulk. At high temperatures the efficiency drops quickly, which is caused by; (i) the decrease in amount of supersaturated solute available for self-healing and (ii) the diffusivities of solute and host are getting closer to each other at high temperatures. In addition, the activation energy for grain-boundary diffusion shows a considerable temperature evolution close to the Curie temperature [47].

The supersaturation can also be expressed as a homologous temperature T_H, which indicates (on the absolute temperature scale) the relative temperature compared to the temperature at which the solute is fully dissolved [51]. Note that this depends on the amount of solute present and is an indication for the driving force for precipitation. For reference the supersaturation and the homologous temperature at $T = 550$ and 650 ℃ are listed in table 6.2.

The mechanism that reduces the growth rate of the creep cavities, also functions
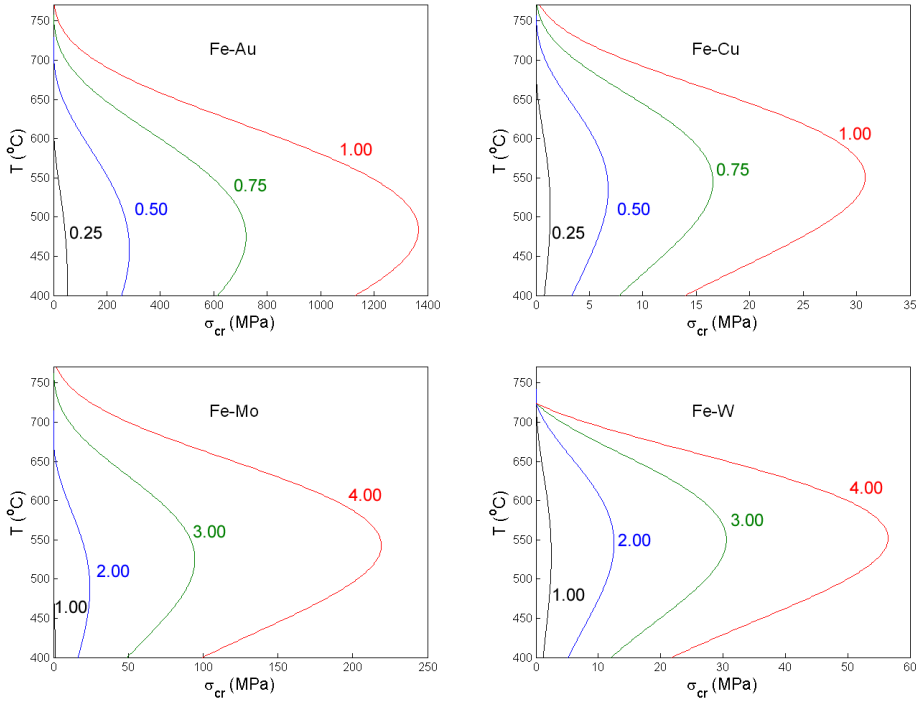
Figure 6.6: Critical stress σ_{crit} for the self-healing of creep damage as a function of temperature T for different compositions of binary Fe-Au, Fe-Cu, Fe-Mo and Fe-W alloys. The nominal solute concentration (in at.%) is indicated for each curve. molybdenum (Mo) and tungsten (W), are more soluble at high temperatures and therefore analysed for higher solute contents.

Table 6.2: Supersaturation and homologous temperature (T_H) of different solute containing alloys, at a temperature of 550°C and in brackets (650°C).

alloy	concentration (at.%)	supersaturation (at.%)	T_H (-)
Au	0.25	0.10 (0.00)	0.92 (1.03)
-	0.50	0.35 (0.19)	0.83 (0.94)
-	0.75	0.60 (0.44)	0.79 (0.89)
-	1.00	0.85 (0.69)	0.76 (0.85)
Cu	0.25	0.19 (0.09)	0.85 (.095)
-	0.50	0.44 (0.34)	0.79 (0.88)
-	0.75	0.69 (0.59)	0.76 (0.85)
-	1.00	0.94 (0.84)	0.73 (0.83)
Mo	1.00	0.00 (0.00)	1.05 (1.17)
-	2.00	0.84 (0.25)	0.86 (0.96)
-	3.00	1.84 (1.25)	0.78 (0.87)
-	4.00	2.84 (2.25)	0.73 (0.82)
W	1.00	0.80 (0.67)	0.73 (0.81)
-	2.00	1.80 (1.67)	0.65 (0.73)
-	3.00	2.80 (2.67)	0.61 (0.69)
-	4.00	3.80 (3.67)	0.59 (0.66)

at stresses higher than the previously determined critical stress for self-healing. In this range ($\sigma > \sigma_{cr}$), the reduction in creep strain rate can be expressed in a parameter η;

$$\eta = 1 - \frac{\dot{\epsilon}(\Delta c_{sol})}{\dot{\epsilon}(0)} = \frac{k_B T}{\Omega \sigma} \frac{4\lambda^3}{\pi a \delta l} \frac{(D_{sol}^{bulk} - D_{host}^{bulk})\Delta c_{sol}^{bulk}}{D_{\square}^{gb} c_{\square}^{gb}}. \tag{6.16}$$

The efficiency of the self-healing process goes to zero at very high stresses and to $\eta = 1$ at the critical stress. In figure 6.7 the efficiency of self-healing is indicated as a function of stress and temperature at different Au concentrations. The addition of molybdenum and tungsten in solid solution is common for creep steels [52]. The addition is generally related to the formation of nanoprecipitates in creep steels. When they are added to remain in solution however the amount which can be solutionized at high temperatures is much higher than for copper or gold, see figure 6.5. The efficiency of self-healing can therefore be analysed for higher nominal concentrations, see figure 6.8.

The efficiency and critical stress for self-healing strongly depends on the relative distance between cavities compared to the size of the creep cavities; $\frac{\lambda}{a}$. The difference in bulk diffusivities between Cu and Au, predict that the self-healing process will work approximately 3 times more efficient for Fe-Au than for Fe-Cu at the same degree of supersaturation. This is in concurrence with what was found in experiments [50]. As expected, temperature has a large effect on the efficiency of self-healing since the self-healing and damage formation processes are diffusional in nature.

Self-healing behavior has potentially been observed in Al-Mg alloys as well [53], where voids were filled by segregation of Mg to a void site. Examples for (partial) self-healing of creep damage by precipitation may also have been observed in other
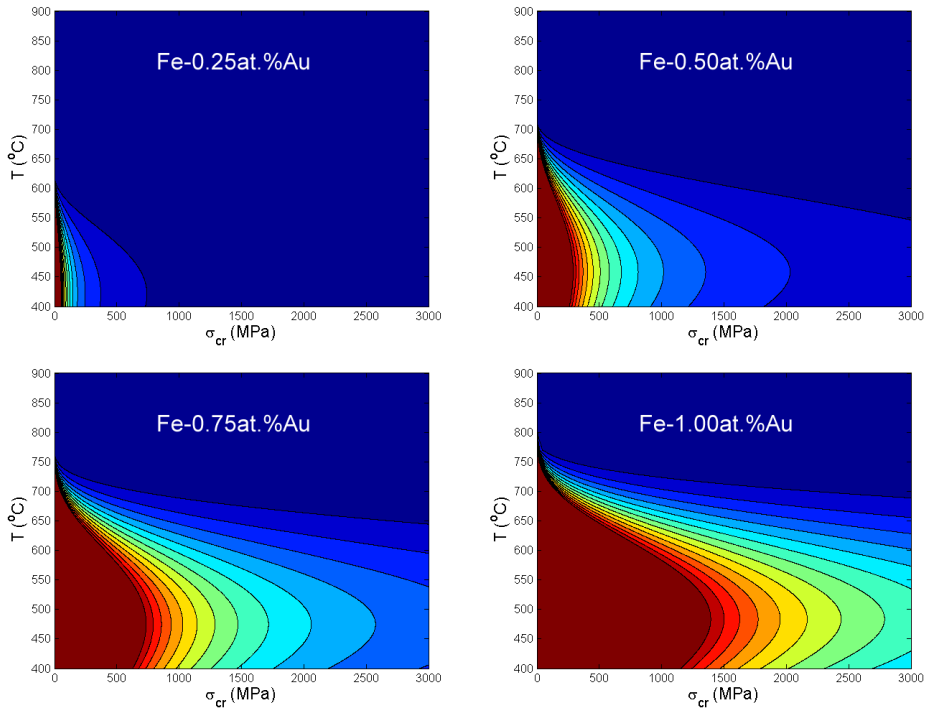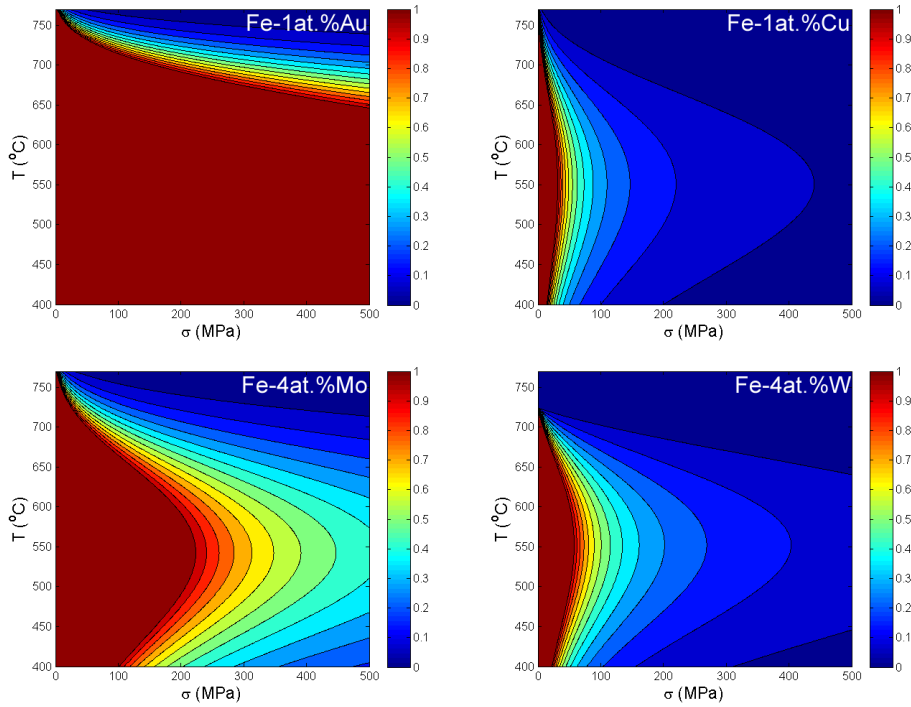
6

Figure 6.7: Self-healing efficiency $\eta = 1 - \frac{\dot{\epsilon}(\Delta c_{sol})}{\dot{\epsilon}(0)}$, as a function of stress and temperature. The critical stress for complete self-healing ($\eta = 1$) as function of temperature is indicated by the red line. The Fe-Au healing is indicated as function of concentration between 0.25% and 1% of nominal concentration. Partial self-healing ($\eta < 1$) is indicated by the other colors. The ferromagnetic transition temperature (T_C) for the bcc Fe matrix is indicated.

Figure 6.8: Self-healing efficiency $\eta = 1 - \frac{\dot{\epsilon}(\Delta c_{sol})}{\dot{\epsilon}(0)}$, as a function of stress and temperature. The critical stress for complete self-healing ($\eta = 1$) as function of temperature is indicated by the red line. Fe-Cu and Fe-Au contain 1% nominal concentration of solute, and Fe-W and Fe-Mo are indicated with 4% nominal concentration of solute. Partial self-healing ($\eta < 1$) is indicated by the other colors. The ferromagnetic transition temperature (T_C) for the bcc Fe matrix is indicated.

metals. For instance, Yousefiani and coworkers [54] presented the creep strain-rates of overheated aluminum alloys. In their samples the precipitates of a 7075 aluminum alloy were dissolved at high temperatures, which caused lower creep strain-rates, and bulky precipitates that form in a similar nature to those formed at creep damage sites in Fe-Au and Fe-Mo alloys [20, 21, 24].

6.4. CONCLUSIONS

A model was presented which predicts that supersaturated solutes can be used to strongly reduce stage II creep rates and thereby extend creep lifetimes. This process can be complementary to conventional methods for creep-resistant metals. The creep cavity growth rate and the strain rate in metal alloys are closely linked during steady-state creep. The creep cavities grow through the drainage of vacancies from grain boundaries on which the cavities nucleate. The vacancy formation on the grain boundaries is linked to the rate of ingress of dislocations to that grain boundary. During the selective precipitate growth process in the creep cavities, a transport of solute atoms takes place. The creep cavities grow by a diffusional flux of vacancies under a chemical potential gradient that originates from the applied stress. This vacancy flux can be countered by a flux of substitutional solute towards creep cavities. The growth of precipitates can thereby reduce growth-rates of a creep cavities, reduce the strain-rate, and increase the creep lifetime. The self-healing efficiency can be described as a function of the amount of supersaturated solute and the relative diffusivities, assuming selective precipitation at the free creep cavity surfaces. It is found that Au is the most efficient solute element for self-healing of creep damage, the addition of Au to a creep-resistant steel is thought to have little effect on other precipitates and could be implemented in creep-resistant steels. Mo and W provide a good and low-cost alternative that have potential for self-healing as long as they remain in supersaturation. For this to be true a higher amount of solute can be added.

6.5. APPENDIX: FLOW RESISTANCE FOR SOLUTE DIFFUSION

Starting from the local flux of solute atoms described by Fick's law,

$$\vec{J}_{sol} = -\frac{1}{\Omega} D_{sol} \vec{\nabla} c_{sol} \tag{6.5.17}$$

and assuming a flow through a volume with a uniform cross section A and a length L the total current of solute (in number of atoms per unit of time) can be expressed as:

$$I = \frac{\dot{V}}{\Omega} = \int_A \vec{J}_{sol} \cdot d\vec{S} = \frac{\Delta c_{sol}}{R}. \tag{6.5.18}$$

The flow resistance then corresponds to:

$$R = \frac{L}{A D_{sol}} \tag{6.5.19}$$

Assuming that; (i) most of the solute that flows to the creep cavity originates from the bulk (grain boundary volume is low compared to the creep cavity volume) and (ii)

we only consider the time scales where the bulk diffusion is significant. Under these conditions we can approximate the diffusional flow of solute atoms as a bulk diffusion and a grain boundary diffusion process in series.

The flow resistance for the bulk diffusion can be approximated by assuming that the effective cross section equals two times the grain boundary surface available for an individual cavity $A_{bulk} = 8\lambda^2$ (to account for the bulk diffusion from both sides of the grain boundary) and that $L_{bulk} \approx l = \sqrt{\pi D_{sol}^{bulk} t}$ is the diffusion length, resulting in:

$$R_{bulk} = \frac{L}{A_{bulk} D_{sol}^{bulk}} \approx \frac{l}{8\lambda^2 D_{sol}^{bulk}}. \tag{6.5.20}$$

The time-dependent diffusion length can be approximated by its maximum value at complete filling of $l_{max} \approx \pi a^3 / 3\lambda^2 \Delta c_{sol}$. The flow resistance for the grain-boundary diffusion can be approximated by assuming that $A_{gb} \approx 2\pi a\delta$ and $L_{gb} \approx \lambda$, resulting in:

$$R_{gb} = \frac{L}{A_{gb} D_{sol}^{gb}} \approx \frac{\lambda}{2\pi a\delta D_{sol}^{gb}}. \tag{6.5.21}$$

The total flow resistance between the nominal solute concentration in the bulk and the solute at the creep cavity surface then corresponds to:

$$R_{tot} = R_{bulk} + R_{gb} \approx \frac{l}{8\lambda^2 D_{sol}^{bulk}} + \frac{\lambda}{2\pi a\delta D_{sol}^{gb}}. \tag{6.5.22}$$

The total supersaturation of solute is now divided over the bulk and the grain boundary as: $\Delta c_{sol}^{bulk} = \Delta c_{sol} R_{bulk} / (R_{bulk} + R_{gb})$ and $\Delta c_{sol}^{gb} = \Delta c_{sol} R_{gb} / (R_{bulk} + R_{gb})$, respectively.

For $l \approx l_{max}$ the ratio of bulk and grain-boundary flow resistances is:

$$\frac{R_{gb}}{R_{bulk}} \approx \frac{a D_{sol}^{bulk}}{\delta D_{sol}^{gb}} \frac{12\lambda^5}{\pi^2 a^5} \Delta c_{sol} \ll 1. \tag{6.5.23}$$

For the Fe-Au alloy with $\Delta c_{sol} = 0.01$, $a = 0.5$ μm, $\lambda = 10$ μm, $\delta = 0.5$ nm, $D_{sol}^{bulk} = 7.47 \times 10^{-21}$ m^{2}s^{-1}, and $D_{sol}^{gb} = 7.43 \times 10^{-12}$ m^{2}s^{-1} at $T = 823$ K, (Table 1) we find $R_{gb}/R_{bulk} = 0.03 \ll 1$. As a result we can assume $R_{tot} \approx R_{bulk}$ and $\Delta c_{sol}^{bulk} \approx \Delta c_{sol}$.

REFERENCES

[1] C. Herring, *Diffusional viscosity of a polycrystalline solid,* J. Appl. Phys. **21**, 437 (1950).

[2] J. Weertman, *Theory of steady-state creep based on dislocation climb,* J. Appl. Phys. **26**, 1213 (1955).

[3] F. Nabarro, *Steady-state diffusional creep,* Philos. Mag. **16**, 231 (1967).

[4] H. Riedel, *Fracture at high temperatures* (Springer-Verlag, 1986) p. 117.

[5] C. Gandhi and M. F. Ashby, *Fracture mechanism maps for materials which cleave: fcc, bcc and hcp metals and ceramics,* Acta Met. **27**, 1565 (1979).

[6] D. Hull and D. E. Rimmer, *The growth of grain-boundary voids under stress,* Philos. Mag. **4**, 673 (1959).

[7] Y. Ishida and D. McLean, *The formation and growth of cavities in creep,* Met. Sci. **38**, 171 (1967).

[8] B. F. Dyson, *Constraints on diffusional cavity growth rates,* Met. Sci. **10**, 349 (1976).

[9] N. G. Needham, *Cavitation and fracture in creep resisting steels*, Tech. Rep. (1983).

[10] J. E. Harris, *Diffusional growth of creep voids,* Met. Sci. **12**, 321 (1978).

[11] W. Beere and M. Speight, *Creep cavitation by vacancy diffusion in plastically deforming solid,* Met. Sci. **12**, 172 (1978).

[12] N. G. Needham and T. Gladman, *Nucleation and growth of creep cavities in a type 347 steel,* Met. Sci. **14**, 64 (1980).

[13] A. Cocks and M. Ashby, *Intergranular fracture during power law creep under multiaxial stresses,* Met. Sci. **14**, 395 (1980).

[14] J. R. Rice, *Constraints on the Diffusive Cavitation of Isolated Grain Boundary Facets in Creeping Polycrystals,* Acta Metall. **29**, 675 (1981).

[15] A. Needleman and J. R. Rice, *Plastic Creep Flow Effects in the Diffusive Cavitation of Grain Boundaries,* Acta Metall. **28**, 1315 (1980).

[16] E. van der Giessen, M. W. D. van der Burg, A. Needleman, and V. Tvergaard, *Void growth due to creep and grain boundary diffusion at high triaxialities,* J. Mech. Phys. Solids **43**, 123 (1995).

[17] M. D. Hager, P. Greil, C. Leyens, S. Van Der Zwaag, and U. S. Schubert, *Self-healing materials,* Adv. Mater. **22**, 5424 (2010).

[18] K. Laha, J. Kyono, S. Kishimoto, and N. Shinya, *Beneficial effect of B segregation on creep cavitation in a type 347 austenitic stainless steel,* Scr. Mater. **52**, 675 (2005).

[19] K. Laha, J. Kyono, and N. Shinya, *An advanced creep cavitation resistance Cu-containing 18Cr-12Ni-Nb austenitic stainless steel,* Scr. Mater. **56**, 915 (2007).

[20] S. Zhang, C. Kwakernaak, F. D. Tichelaar, W. G. Sloof, M. Kuzmina, M. Herbig, D. Raabe, E. Brück, S. van der Zwaag, and N. H. van Dijk, *Autonomous repair mechanism of creep damage in Fe-Au and Fe-Au-B-N alloys,* Metall. Mater. Trans. A **46**, 5656 (2015).

[21] S. Zhang, C. Kwakernaak, W. G. Sloof, E. Brück, S. van der Zwaag, and N. H. Van Dijk, *Self healing of creep damage by gold precipitation in iron alloys,* Adv. Eng. Mater. **17**, 598 (2015).

[22] H. Fang, C. D. Versteylen, S. Zhang, Y. Yang, P. Cloetens, D. Ngan-Tillard, E. Brück, S. van der Zwaag, and N. H. van Dijk, *Autonomous filling of creep cavities in Fe-Au alloys studied by synchrotron X-ray nano-tomography,* Acta Mater. **121**, 352 (2016).

[23] W. W. Sun, H. Fang, N. H. van Dijk, S. van der Zwaag, and C. R. Hutchinson, *Linking surface precipitation in Fe-Au alloys to its self-healing potential during creep loading,* Metall. Mater. Trans. A **48**, 2109 (2017).

[24] S. Zhang, H. Fang, M. E. Gramsma, C. Kwakernaak, W. G. Sloof, F. Tichelaar, M. Kuzmina, M. Herbig, D. Raabe, E. Brück, S. van der Zwaag, and N. H. van Dijk, *Autonomous filling of grain-boundary cavities during creep loading in Fe-Mo alloys,* Metall. Mater. Trans. A **47**, 4831 (2016).

[25] D. Dunand, B. Han, and A. Jansen, *Monkman-Grant analysis of creep fracture in dispersion-strengthened and particulate-reinforced aluminium,* Metall. Mater. Trans. A **30**, 829 (1999).

[26] R. Raj and M. F. Ashby, *Intergranular fracture at elevated temperature,* Acta Metall. **23**, 653 (1975).

[27] B. Budiansky, J. W. Hutchinson, and S. Slutsky, *On void collapse in viscous solids,* in *Mech. Mater.*, edited by H. Hopkins and M. J. Sewell (Pergamon Press, 1982) pp. 13–45.

[28] A. C. F. Cocks and M. F. Ashby, *On creep fracture by void growth,* Prog. Mater. Sci. **27**, 189 (1982).

[29] Y. Ishida and M. H. Brown, *Dislocations in grain boundaries and grain boundary,* Acta Metall. **15**, 857 (1967).

[30] B. Dyson, *Continuous cavity nucleation and creep ductility,* Scr. Metall. **17**, 31 (1983).

[31] E. Clouet, L. Ventelon, and F. Willaime, *Dislocation core energies and core fields from first principles,* Phys. Rev. Lett. **102**, 055502 (2009), arXiv:0902.1451 .

[32] E. Orowan, *Problems of plastic gliding,* Proc. Phys. Soc. **52**, 8 (1940).

6

[33] M. Kabir, T. T. Lau, D. Rodney, S. Yip, and K. J. Van Vliet, *Predicting dislocation climb and creep from explicit atomistic details,* Phys. Rev. Lett. **105**, 1 (2010).

[34] D. Caillard, *Kinetics of dislocations in pure Fe. Part II. In situ straining experiments at low temperature,* Acta Mater. **58**, 3504 (2010).

[35] U. Messerschmidt, *Dislocation dynamics during plastic deformation*, Springer Series in Materials Science (Springer Berlin Heidelberg, 2010).

[36] M. C. Miguel, A. Vespignani, S. Zapperi, J. Weiss, and J.-R. Grasso, *Intermittent dislocation flow in viscoplastic deformation,* Lett. to Nat. **410**, 667 (2001), arXiv:0007487 [cond-mat] .

[37] A. Fuchs and B. Ilschner, *An analysis of the creep behaviour of iron-molybdenum solid solutions,* Acta Metall. **17**, 701 (1969).

[38] M. Upmanyu, D. Srolovitz, L. Shvindlerman, and G. Gottstein, *Vacancy generation during grain boundary migration,* Interface Sci. **6**, 287 (1998).

[39] R. J. Dikken, B. J. Thijsse, and L. Nicola, *Impingement of edge dislocations on atomically rough contacts,* Comput. Mater. Sci. **128**, 310 (2017).

[40] A. Elzas and B. Thijsse, *Dislocation impacts on iron/precipitate interfaces under shear loading,* Model. Simul. Mater. Sci. Eng. **24**, 085006 (2016).

[41] L. Trimble, D. Finn, and A. Gosgarea, *A Mathematical analysis of diffusion coefficients in binary systems,* Acta Met. **13**, 501 (1984).

[42] M. Danielewski, W. Krzyzanski, and R. Bachorczyk, *Generalized Darken's method from diffusional structures to nonparabolic diffusion,* .

[43] Q. Chen and Z. Jin, *The Fe-Cu system: A thermodynamic evaluation,* Metall. Mater. Trans. A **26**, 417 (1995).

[44] H. Okamoto and T. Massalski, *The Au-Fe (Gold-Iron) system,* Bull. Alloy Phase Diagrams **5**, 430 (1984).

[45] A. F. Guillermet, *The Fe-Mo (Iron-Molybdenum) system,* Bull. Alloy Phase Diagrams **3**, 359 (1982).

[46] B. Predel, *Fe-W (Iron-Tungsten),* in *Landolt-Börnstein - Gr. IV Phys. Chem. 5E, (Dy-Er –Fr-Mo)* (1995) pp. 1–4.

[47] A. Inoue, H. Nitta, and Y. Iijima, *Grain boundary self-diffusion in high purity iron,* Acta Mater. **55**, 5910 (2007).

[48] C. D. Versteylen, N. H. van Dijk, and M. H. F. Sluiter, *First-principles analysis of solute diffusion in dilute bcc Fe-X alloys,* Phys. Rev. B **96**, 094105 (2017).

[49] T. Kop, *A dilatometric study of the austenite/ferrite interface mobility*, Ph.D. thesis, Delft University of Technology (2000).

[50] S. Zhang, *Self healing of damage in Fe-based alloys*, Ph.D. thesis, Technische Universiteit Delft (2015).

[51] H. I. Aaronson, M. Enomoto, and J. K. Lee, *Mechanism of diffusional phase transformations in metals and alloys* (CRC Press, Boca Raton, 2010).

[52] Y. Kadoya, B. F. Dyson, and M. McLean, *Microstructural stability during creep of Mo- or W-bearing 12Cr steels,* Metall. Mater. Trans. A Phys. Metall. Mater. Sci. **33**, 2549 (2002).

[53] M. Song, K. Du, C. Wang, S. Wen, H. Huang, Z. Nie, and H. Ye, *Geometric and chemical composition effects on healing kinetics of voids in Mg-bearing Al alloys,* Metall. Mater. Trans. A **47**, 2410 (2016).

[54] A. Yousefiani, F. A. Mohamed, and J. C. Earthman, *Creep rupture mechanisms in annealed and overheated 7075 Al under multiaxial stress states,* Metall. Mater. Trans. A **31**, 2807 (2000).

6

ACKNOWLEDGEMENTS

The end of this thesis and also of my PhD project leads to a moment of reflection. No PhD is done alone, which is especially so in my case. With 3 promotors, 2 departments, 3 industrial partners, there was always help available. I owe gratitude to everyone involved for their help, or for simply being around to keep me sane(ish).

I would like to thank Marcel for his enthusiasm and relentless perfectionism. The enthusiasm was a reason for me to do the PhD and the perfectionism is something I have benefited from. His strong opinions make discussions very interesting. But mostly I would like to thank him for the things he taught me.

Thanks to Niels for being patient and practical. With a firm vision on self-healing, he always managed to make me keep a steady course. I am grateful that he was always glad to explain physics to an engineer, for the interesting experiments in Grenoble, and his overall drive to get me to the end.

Thanks to Ekkes for being my promotor, even though he has enough on his plate. Whenever we had meetings he always had time and insight to discuss and suggest new directions, or to go through his big books of binary phase diagrams. I would like to thank you for pushing me a bit when I needed it.

Without Sybrand or Hao Chen I would not have started a PhD. You two inspired me to stay at the university and Sybrand even send me to the interview for this position. I would like to thank Sybrand for the special interest he has always showed for my work and his openness and for creating NovAM, which vibrant atmosphere is his merit. In short, thanks for being a mentor.

Thanks to Shasha Zhang for being so good and welcoming, it made the start of my PhD much easier and Haixing Fang making the end of it much more interesting. Any project owes gratitude to the funding, but in this case I would like to single out Annette Steggerda and Daniëlle van Loon for organizing our workshops and summer schools. I would like to thank, from FNsteel: Annemarie van Geest and Tjitze Postma, from TATAsteel: Kees Bos and Pieter van der Wolk, and from SKF: Erik Vegter and Sebastián Echeverri Restrepo. I would like to thank Fred Vermolen for help with setting up the FE model and discussions on diffusional flux equations. Thanks to Professor Hiroshi Numakura for helpful discussions regarding diffusion in bcc iron.

I would like to acknowledge the nice people of the Max Planck institute für Eisenforschung, that were really helpful and accommodating whenever we could meet. Thank you to Jan Janßen, Martin Staadt, Poulumi & Bishwanath and all the others. Special thanks to Fritz Körmann, who needs half a word to understand the problem and give the appropriate solution.

I would like to thank those who gave me the opportunity to follow or supervise courses. Thanks to Guido Janssen, Cristina, Alkisti and Jaap, I now understand much more thermodynamics than before. Thanks to Wim Bouwman I got to experience supervising bachelor students. A special thanks to Nikodem and Maarten for working very hard and

CURRICULUM VITÆ

Casper VERSTEYLEN

23-09-1986	Born in Tilburg, the Netherlands.

EDUCATION

1999–2005	Grammar School OLV lyceum, Breda (1999–2005) Breda, the Netherlands (1999–2005)
2005–2013	Undergraduate in Aerospace Engineering Delft University of Technology
2018	PhD. Computational Materials Science Delft University of Technology *Thesis:* Modelling self-healing steel

LIST OF PUBLICATIONS

6. **C.D. Versteylen**, M.H.F. Sluiter, *Magnetic activation energy for diffusion in bcc iron*, in preparation.

5. **C.D. Versteylen**, M.H.F. Sluiter, N.H. van Dijk, *Modelling formation and self healing of creep damage in iron-based alloys.*, submitted.

4. **C.D. Versteylen**, N.H. van Dijk, M.H.F. Sluiter, *A new design principle for creep resistant materials*, submitted.

3. **C.D. Versteylen**, N.K. Szymanski, M.H.F. Sluiter, N.H. van Dijk, *Finite element modelling of creep cavity filling by solute diffusion*, Philos. Mag. **98**, 864, (2018).

2. **C.D. Versteylen**, N.H. van Dijk, M.H.F. Sluiter, *First-principles analysis of solute diffusion in dilute bcc Fe- X alloys*, Phys. Rev. B **96**, 094105 (2017).

1. H. Fang, **C.D. Versteylen**, S. Zhang, Y. Yang, P. Cloetens, D. Ngan-Tillard, E. Brück, S. van der Zwaag, and N.H. van Dijk, *Autonomous filling of creep cavities in Fe-Au alloys studied by synchrotron X-ray nano-tomography*, Acta Mater. **121**, 352 (2016).